DPhil Thesis



Domenico Campanaro

Supervisor: Prof. Li He

Analysis of the Aerothermal Characteristics of Additively Manufacturable Surface Microstructures

---

Oxford Thermofluids Institute, Department of Engineering Science

Christ Church College. May 31, 2024

Contents

Acknowledgments **2**

Abstract **5**

Nomenclature **8**

List of Figures **16**

List of Tables **17**

1 Introduction **18**

1.1 Background and Motivation 18

1.1.1 Development of Additive Manufacturing 18

1.1.2 Surface Finish as a Potential Design Space 21

1.1.3 Aerothermal Impact of Surface Structures 24

1.1.4 Interactions Between Aerodynamics and Heat Transfer 27

1.2 Thesis Outline 30

2 Literature Review **31**

2.1 Behavior of Regular and Random Roughness 33
2.1.1 Impact on the Aerothermal Characteristics of a Surface 33
2.1.2 Limits of Conventional Parameters for Roughness Characterization 39
2.2 Limits to the Application of Newton's Law of Cooling 43
2.3 Aerodynamics and Heat Transfer Interactions 47
2.3.1 Impact of Heat Transfer on Turbulent Transition 50
2.4 CFD Analysis of Surface Microstructure arrays 52
2.4.1 Conjugate Heat Transfer Approaches 52
2.4.2 Multiscale Methods 55
2.5 Remarks 58

3 Heat Transfer Effects on a Flat-Plate Laminar Boundary Layer 63

3.1 Computational method and set-up 64
3.2 Flat plate boundary layer under different TRs 66
3.2.1 Basic validation and mesh sensitivity 66
3.2.2 Impact of wall temperature 66
3.3 Remarks 73

4 Heat Transfer Effects for a Surface Microstructure Array 75

4.1 Computational method and set-up 76
4.2 Numerical sensitivity study 81
4.3 Laminar flow results 82
4.3.1 Local Reynolds number effect 83

4.3.2 Impact of TR on aerothermal parameters 88
4.4 Transition to turbulent flow 91
4.4.1 Transitional flow behavior at a given Re_r 91
4.4.2 Transitional regime at different Re_r 93
4.4.3 Non-dimensional characterization 97
4.5 Remarks 101

5 Surface Microstructure Array Under Pressure Gradient 103

5.1 Solver description and validation 105
5.1.1 Preliminary validation 106
5.2 Computational method and set-up 112
5.3 Smooth Wall Validation 119
5.4 Adiabatic Surface Microstructure Array 126
5.5 Remarks 132

6 Heat Transfer Effects for Surfaces Under Pressure Gradient 134

6.1 Smooth Wall 135
6.2 Surface Microstructure Array 145
6.3 Remarks 148

7 Conclusions and Future Work 150

7.1 Conclusions 150
7.2 Future work 155

References **157**

Acknowledgments

I would like to express my sincere gratitude to those who have supported me throughout my DPhil program.

First and foremost, my heartfelt thanks go to my supervisor, Prof. Li He, whose expertise and insightful guidance have been invaluable throughout this research. His wisdom, patience, and academic rigor have profoundly shaped my work and thinking.

I am also very grateful to my industrial sponsor, Siemens Energy. I extend my special appreciation to Roger Wells, Yansheng Li, and Omar Valero for their valuable technical discussions and contributions that greatly enriched my research experience.

My sincere thanks also go to the University of Oxford Advanced Research Computing (ARC) facility for providing the essential resources and support that played a crucial role in my research.

I would also like to thank my family, my girlfriend and my friends for their encouragement and support during this journey.

Abstract

This thesis investigates the aerothermal behavior of surfaces, with a particular focus on the interplay between aerodynamics and heat transfer, which raises many questions in current state-of-the-art research and industrial practice, where flow and thermal fields are often considered uncoupled due to the underlying complexity of the problem. In fact, studying aerothermal coupling in high-temperature scenarios could potentially require performing experiments in prohibitive conditions or necessitate fluid-solid conjugate heat transfer simulations, both of which approaches are often impractical.

The research encompasses several scenarios, ranging from a simple flat-plate laminar boundary layer to a rough wall characterized by an array of surface microstructures under a pressure gradient, and highlights the substantial changes in fluid properties and flow fields attributable to wall heat transfer.

With the goal of studying the aerothermal behavior of surface microstructures, a comprehensive literature review lays the foundational context by illustrating challenges in characterizing surface roughness, especially in distinguishing between regular roughness composed of surface microstructures and random roughness. It also identifies the limitations of Newton's law of cooling in scenarios with significant fluid-solid tempera-

ture differences and emphasizes the importance of interactions between aerodynamics and heat transfer, underscoring the relevance of conjugate heat transfer analysis.

The study begins with an examination of a laminar flat-plate boundary layer under various thermal conditions, with a focus on the use of conventional parameters such as the friction coefficient and Nusselt number in capturing the interplay between aerodynamics and heat transfer. The analysis reveals that these parameters may show small variations under different thermal boundary conditions, thus concealing the true impact of heat transfer on flow. As a result, the local Reynolds number has been identified as a more telling indicator of the interplay between flow and thermal fields.

In light of these findings, surface microstructures under zero pressure gradient are analysed, showing significant variations in the local Reynolds number distribution due to heat transfer and their impact on the flow field. These variations considerably influence the critical Reynolds number, leading to earlier transitions to turbulent flow in cooled wall cases and delayed transitions for heated walls. Additionally, the study presents a practical method for scaling wall heat transfer effects, offering promising potential for aerothermal engineering applications.

The thesis progresses to analyze more realistic scenarios, such as larger arrays of surface microstructures subjected to the pressure gradient of a high-lift, low-pressure turbine airfoil using a novel multiscale block spectral approach for resolving the flow around these microstructures. Initially, a smooth wall under such a pressure gradient is used for validation against experimental data from published literature, showing good agreement with the simulations in this project. Finally, an array of surface mi-

crostructures under the same pressure gradient is examined for different wall thermal conditions. This investigation confirms a significant interplay between aerodynamics and heat transfer, extending previous insights to include larger arrays of microstructures in the presence of a pressure gradient.

Nomenclature

Δt_{nd}	non-dimensional time step; $(time\ step/throughflow\ time)$
δ	boundary layer thickness
$\delta*$	displacement thickness
η	Blasius non-dimensional y-coord.; $(y\sqrt{u_\infty \rho_\infty / \mu_\infty\, x})$
μ	dynamic viscosity
ρ	density
τ	stress tensor
τ_w	wall shear stress
θ	momentum thickness
C	chord length
C_D	drag coefficient; $(C_{D_f} + C_{D_p})$
C_f	local friction drag coefficient

C_{D_f} friction drag coefficient

C_{D_p} pressure drag coefficient

D_{tot} local Reynolds number difference

e local total energy

h or HTC heat transfer coefficient; $(q/(T_w - T_{01}))$

I turbulence intensity

k free-stream thermal conductivity

L flat plate length

Nu_L flat plate Nusselt number based on L

Nu_r surface microstructure Nusselt number based on r

Nu_{ref} reference Nusselt number

Pr Prandtl number

q heat flux

r pin radius

Re_L Reynolds number based on L; $(\rho_\infty u_\infty L/\mu_\infty)$

Re_r Reynolds number based on r; $(\rho_\infty u_\infty r/\mu_\infty)$

Re_c Reynolds number based on C; $(\rho_\infty u_\infty C/\mu_\infty)$

Re_{local} local Reynolds number

T_w wall temperature

T_{01} inlet total temperature

T_{ad} adiabatic wall temperature

$TR = T_w/T_{01}$ temperature ratio

u_{max} boundary layer edge velocity at the suction peak location

Abbreviations

AM	Additive manufacturing
BC	Boundary condition
CFD	Computational fluid dynamics
CHT	Conjugate heat transfer
DMLS	Direct metal laser sintering
HPT	High pressure turbine
HT	Heat transfer
HTC	Heat transfer coefficient
LES	Large eddy simulation
LP	Low-pressure
MSUP	Multiscale upwind based fluid-solid coupled solver
RANS	Reynolds-averaged Navier-Stokes
SHTC	Spectral heat transfer coefficient
SLM	Selective laser melting
TMEP	Theorem of Minimum Entropy Production
TR	Temperature ratio

List of Figures

1.1 Surface microstructure arrays produced with Quantum X, a lithography system manufactured by NanoScribe. a) Sharp micro-needles created to control small quantities of liquids, e.g. for the precise formation of jets. b) Micro-optical array with high fill factors. Reprinted from [1]. 23

1.2 a) Cooling effectiveness distribution comparison between smooth and ribbed end walls, with the ribbed end wall demonstrating notably superior cooling effectiveness. b) Visualization of iso-temperature surfaces for both cases, illustrating the secondary flow attenuation and enhanced cooling effectiveness achieved with the ribbed end wall. Reproduced from [2] 25

1.3 Friction factor augmentation versus Nusselt number augmentation are plotted for all DMLS microchannels manufactured by Ferster et al. [3], straight DMLS microchannels, and conventionally manufactured (relatively smooth-walled) containing pin fins and ribs. Reprinted from [3]. . 27

2.1 Thermal boundary condition independency of $h_{adiabatic}$. Reprinted from Moffat [4]. 44

2.2 The two-temperature method accurately predicts HTC distribution only when HTC and wall temperature (T_w) are aerodynamically determined. Otherwise, when HTC relies on temperature difference (ΔT) and T_w, the heat flux-ΔT relationship becomes nonlinear. Reprinted from [5] 48

2.3 The HTC distributions on the suction surface of a nozzle guide vane passage for two temperature ratios (TR) are compared. Using the conventional two-point heat transfer method results in local discrepancies of up to 30-40%. Reprinted from [6] 49

3.1 Flat plate boundary layer domain (height and length are to the scale H/L=2.5). 66

3.2 Mesh dependency study for flat plate boundary layer 67

3.3 Impact of Temperature Ratio (TR) on the velocity profile 68

3.4 Profiles of dynamic viscosity and velocity gradient at different wall temperature conditions non-dimensionalized using adiabatic values at the wall 69

3.5 Local Reynolds number profile 71

3.6 The contribution of velocity, dynamic viscosity, and density to increasing Re_{local} in the near-wall region for TR=0.5 72

4.1 Surface microstructure array domain: a row of eight hemispherical surface microstructures of $500\mu m$ radius 79
4.2 Inlet velocity profile, obtained by specifying a total pressure profile to match the laminar Blasius solution as shown 79
4.3 Velocity contours, a) Laminar flow field Re_r=700, b) Turbulent flow field Re_r=6200 80
4.4 Vorticity iso-surfaces colored with u values: a) laminar, b) turbulent . . 80
4.5 O-grid mesh around one of the microstructures 81
4.6 Sampling time length study. The reference value Nu_{ref} is $\overline{Nu_r}$ after sampling for 10 through-flow times 83
4.7 Impact of TR=0.5 on Re_{local} for an array of surface microstructures . . 84
4.8 The contribution of velocity, dynamic viscosity and density to increasing Re_{local} in the near wall region for TR=0.5 85
4.9 Impact of TR on the velocity field near surface microstructures. The contour is clipped at u/u_∞=0, thus reversed flow only is depicted . . . 86
4.10 Impact of TR=1.5 on Re_{local} for an array of surface microstructures . . 87
4.11 The contribution of velocity, dynamic viscosity and density to reducing Re_{local} in the near wall region for TR=1.5 87
4.12 Impact of TR on aerothermal parameters at Re_r=720 88
4.13 Impact of TR on the local C_{D_f} distribution. The C_{D_f} contour is 3D, and 2D streamlines are plotted on the mid-pitch cut-plane (z=0) 90
4.14 Velocity field at Re_r=4000. a) TR=0.98, b) TR=0.5 92

4.15 Power spectral density of axial velocity downstream of the last microstructure at $Re_r = 4000$ for TR=0.5 92

4.16 C_D-Re_r chart for three wall temperatures: cooled wall (TR=0.5), quasi-adiabatic (TR=0.98), and TR=1.5 (heated wall) 93

4.17 Nu_r-Re_r chart for three wall temperatures: cooled wall (TR=0.5), quasi-adiabatic (TR=0.98), and TR=1.5 (heated wall) 94

4.18 Power spectral density of axial velocity downstream of the last microstructure at $Re_r = 6200$ for TR=0.5, and TR=0.98 94

4.19 Time-averaged velocity, Re_r=6200. The velocity contour is clipped at $\bar{u}/u_\infty$=0 96

4.20 Velocity contours at Re_r=3450. a) Compressible flow at TR=0.5; b) Incompressible flow at TR=0.5; c) Compressible flow at TR=0.98 . . . 96

4.21 Applicability of the incompressible flow solution to transition under the influence of heat transfer 97

4.22 Non-dimensional analysis method to determine z_{Nu} 99

4.23 Regrouped non-dimensional characteristics 100

5.1 Impact of TR on the velocity profile for flat-plate boundary layer. Comparison of Msflows present results with ANSYS FLUENT show matching within a 1% difference 108

5.2 2D surface microstructure in a flat-plate laminar boundary layer flow field 109

5.3 Msflows resuslts validation against ANSYS FLUENT for a 2D surface microstructure located in a flat-plate laminar boundary layer 109
5.4 3D surface microstructure flow domain used for the validation of Msflows 110
5.5 Velocity profiles upstream and downstream of a 3D surface microstructure to validate Msflows present results against ANSYS FLUENT 111
5.6 a) Experimental domain by Jeong et al. [7]; b) Msflows present simulation domain 114
5.7 Rough wall Msflows simulation domain 116
5.8 Surface microstructure pattern parametrization 117
5.9 Embedded mesh around the surface microstructures 119
5.10 Time-averaged flow field on a mid-span cut plane at Re_C=120000 in the smooth bottom surface case from the present Msflows simulations. Locations of separation onset 'S' and reattachment 'R' are also indicated on the contour plot for comparison with Jeong et al. [7] 120
5.11 Comparison with experimental data by Jeong et al. [7]: static pressure coefficient plotted versus normalized streamwise location for the smooth surface at Re_c=120000 121
5.12 Comparison with experimental data by Jeong et al. [7]: time-averaged velocity profiles at Re_c=120000 for the smooth surface case 122
5.13 Comparison with experimental data by Jeong et al. [7]: Reynolds shear stress profiles at Re_c=120000 for the smooth surface case 123

5.14 Time-averaged flow field on a mid-span cut plane at Re=520000 for the smooth surface case from the present Msflows simulations 124

5.15 Comparison with experimental data by Jeong et al. [7]: time-averaged velocity profiles at Re_c=520000 for the smooth surface case 124

5.16 Comparison with experimental data by Jeong et al. [7]: Reynolds shear stress profiles at Re_c=520000 for the smooth wall case 125

5.17 Comparison with experimental data by Jeong et al. [7]: transition onset at Re_c=520000 126

5.18 Comparison with experimental data by Jeong et al. [7]: time-averaged flow field on a mid-span cut plane at Re=120000 for both a) smooth wall and b) rough wall. Separation onset and reattachment location are indicated respectively with S and R 128

5.19 Time-averaged velocity profiles at Re_c = 120000 for smooth and rough surface cases 130

5.20 Flow field near surface microstructures under an adverse pressure gradient at Re_c = 120000 130

6.1 Time-averaged flow field on a mid-span cut plane at Re=120000 for the smooth wall case with three different TRs: cooled wall (TR=0.5), heated wall (TR=1.5), and adiabatic (TR=1). Separation onset and reattachment location are indicated respectively with S and R 136

6.2 Impact of TR on the a) time-averaged velocity profile, and b) local Reynolds number profile at Re_c=120000, upstream of the separation bubble for the smooth wall case 138

6.3 Impact of TR on the separation bubble maximum height location (MH) at Re_c=120000for the smooth wall case 141

6.4 Time-averaged flow field on a mid-span cut plane at Re=520000 for the smooth wall case with three different TRs: cooled wall (TR=0.5), heated wall (TR=1.5), and adiabatic (TR=1). Transition onset locations are indicated with dash lines 142

6.5 Impact of TR on the a) time-averaged velocity profile, and b) local Reynolds number profile at Re_c=520000for the smooth wall case 143

6.6 Time-averaged flow field on a mid-span cut plane at Re=120000 for the rough wall case with three different TRs: cooled wall (TR=0.5), heated wall (TR=1.5), and adiabatic (TR=1). Separation onset and reattachment location are indicated respectively with S and R 146

6.7 Impact of TR on the velocity field near surface microstructures under a pressure gradient at Re=120000. The contour is clipped at u/u_∞=0, thus reversed flow only is depicted 147

List of Tables

3.1 Impact of TR on performance parameters for a flat-plate laminar boundary layer 68

4.1 Mesh size sensitivity for an array of surface microstructure 82

4.2 Time step size sensitivity for an array of surface microstructure 82

4.3 Turbulence intensity value at a point downstream of the microstructures 95

Chapter 1

Introduction

1.1 Background and Motivation

1.1.1 Development of Additive Manufacturing

Additive Manufacturing (AM), also known as 3D printing, is an innovative method of producing three-dimensional objects by adding material layer by layer, and is set to revolutionize how products are created, made and delivered to customers [8,9]. In recent years, the development of additive manufacturing (AM)/"3D printing" technology has generated significant academic and industrial interest due to its capability to produce complex geometries at an affordable cost for many devices and machines that require complex and lightweight components (e.g. turbomachinery or micro-electro-mechanical systems [10, 11]).

In the 1990s, AM was considered suitable mainly for prototyping and not for the production of ready technologies [12]. In the past 30 years, 3D printing has made

significant progress in terms of precision, repeatability, and material range. Thus, it is no longer seen just as a rapid prototyping technique, and many engineering firms are adopting it on production lines. Especially for products with a relatively low production rate, such as gas turbines, AM is becoming an increasingly more appealing option in the design and maintenance process [13–15].

An example of a company that is using AM to produce gas turbine components is General Electric (GE), which is implementing AM to manufacture the low-pressure compressor blades of the GE9X jet engine [16], and started a joint venture with Safran Aircraft Engines called CFM Leap to produce 3D-printed fuel injectors [17]. The main advantages of AM fuel injectors are that they are lighter and more durable than conventional ones. Their internal design is sophisticated and could not be realized with standard casting techniques. Moreover, the conventional manufacturing procedure implies the need for welding and brazing various casted components, causing additional production difficulties [18].

Furthermore, Siemens, another major company in the energy field, has adopted AM technology for various applications in the gas turbine industry. As reported in the public domain in 2017 [19], Siemens has carried out the first full load test of 3D printed HP turbine blades. Siemens believes that utilizing additive manufacturing (AM) processes can significantly reduce the time required for design and testing, shifting from the conventional timeline of years to a few months. The entire process for these turbine blades, produced by Siemens, from initial component design to rigorous testing, took only 18 months, including the development of new materials, extensive simulation, and

rigorous quality control. The ink used for 3D printing the turbine blades consisted of a high-temperature-resistant powdered polycrystalline nickel-based superalloy. Consequently, the AM-bladed turbines proved capable of handling high pressures, extreme temperatures exceeding 1500K, and centrifugal forces exceeding 13,000 RPM during the demanding full load test.

Over the years, researchers have tried to improve the effectiveness of transpiration and film cooling configurations for gas turbines. Many promising cooling concepts with complex shapes and configurations have been designed. However, until recently, many of these designs were challenging to manufacture due to limitations with conventional manufacturing methods. Now, with the advances in additive manufacturing, it is possible to create turbine parts using high-temperature nickel alloys that feature detailed geometry features. Snyder et al. [20] designed and manufactured various film cooling holes using a laser powder bed fusion process, and Xu et al. [21] offered insights into AM's role in transpiration cooling. Their findings emphasize the potential of additive manufacturing in the development and production of cooling systems for gas turbines.

Additive manufacturing is currently under research for other applications, including microelectromechanical systems (MEMS). Chu et al. [22] undertook a study with the objective of augmenting the critical heat flux within microelectromechanical systems (MEMS). This was pursued through the implementation of precisely engineered micropillars, each featuring dimensions below 100 µm. Their experimental investigation yielded a significant enhancement in critical heat flux, increasing it by approximately 160%. This augmentation was primarily attributed to the amplified capillary forces due

to the implementation of machined microstructures.

AM is advancing rapidly, yet it faces challenges in ensuring the quality of fabricated parts, as well as their long-term durability [23]. Even if the additively manufactured parts are becoming more comparable to those produced with conventional manufacturing [24], they are often characterised by inferior mechanical properties, resulting in early cracking due to the residual stresses caused by the rapid cooling nature of the process [25]. Additionally, for different AM techniques, the capability of producing single crystal, and/or directionally solidified parts and intermetallic alloys needs to be developed [26]. The challenges related to printability, such as porosity, distortion, and surface roughness, have been documented in the literature and appear to pose significant hurdles to overcome, as they are influenced by a number of factors including the build direction [27, 28].

1.1.2 Surface Finish as a Potential Design Space

3D printing is expanding manufacturing flexibility and enabling novel design strategies that were previously impractical due to manufacturing challenges. These emerging capabilities not only facilitate the production of intricate shapes, but also provide control over fine details that were historically difficult to manage, including surface finish patterns.

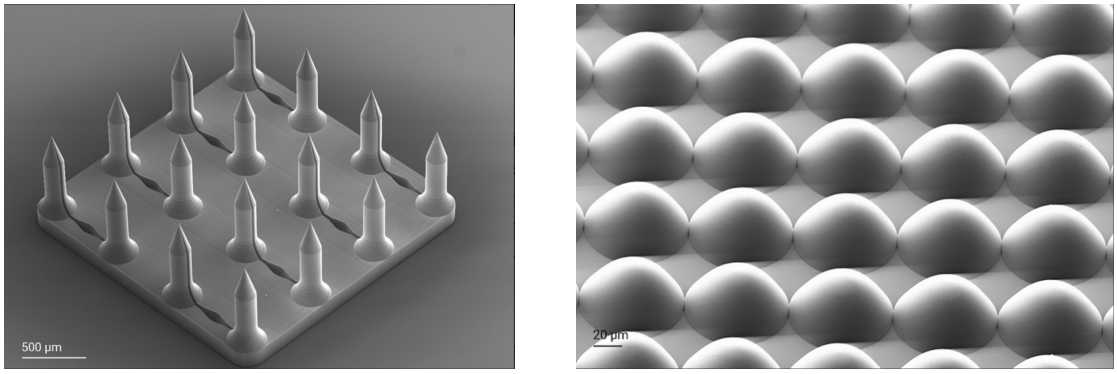
In the gas turbine industry, surface roughness has traditionally been considered an inherent outcome of the manufacturing process and, as such, has been addressed in a stochastic manner through the use of empirical models. The operating cycles of gas

turbines subject components to various degradation mechanisms, including erosion, corrosion, and other factors that can compromise structural integrity and increase surface roughness [29]. In many cases, this increased roughness negatively impacts gas turbine performance. However, it is important to note that there are cases where surface roughness has been observed to enhance the aerothermal properties of a surface, often by mitigating laminar separation bubbles [30].

Additive manufacturing (AM) can enable the creation of specific surface finish patterns, as confirmed by numerous startups engaged in the 3D printing industry and academic researchers [1, 31]. 3D printing could potentially transform roughness from an unpredictable stochastic characteristic into an intentional and additional design parameter. For example, NanoScribe is a company that specializes in lithography systems for the precise manufacturing of optical components. In Figure Figure 1.1, two surface arrays produced using one of their tools, Quantum X, are illustrated. This technology opens up possibilities for the fabrication of various microfluidic elements such as filters, mixers, and capillary pumps using 3D microfabrication.

It is important to note that different materials present distinct challenges in the 3D printing process and vary in production costs. For example, in aerospace applications, components often require superalloys capable of withstand extreme thermal environments. Research has shown that cobalt-based alloys consistently achieve smoother surface quality and lower surface roughness compared to nickel-based alloys, which are characterized by high pressure losses and a significantly increased friction factor that is not always matched by increases in heat transfer [32].

Although additive manufacturing has the potential to create complex surface finish patterns, accurately producing high-quality surface microstructures with materials that must endure harsh conditions remains a significant challenge. Several strategies can be implemented to postprocess 3D-printed components and improve surface quality, but they can be expensive and difficult to perform around small features like surface microstructures. The future will likely see an increase in innovative automated post-processing solutions to keep up with the expanding AM sector. Although automated solutions can boost productivity, most current systems are designed for polymer AM parts, with standard post-processing still used for metal AM [33].



(a) Microoptical elements (b) Micro-needles

Figure 1.1: *Surface microstructure arrays produced with Quantum X, a lithography system manufactured by NanoScribe. a) Sharp micro-needles created to control small quantities of liquids, e.g. for the precise formation of jets. b) Micro-optical array with high fill factors. Reprinted from [1].*

The influence of stochastic roughness on aerothermal technologies is extensively documented in the literature. However, the specific contribution of deterministic manufacturable roughness remains less understood. Recent research has demonstrated that the shape and arrangement of machined roughness elements significantly affect aerody-

namics and heat transfer [34]. These findings suggest that a carefully designed surface finish pattern could potentially enhance the performance of aerothermal technologies such as gas turbines or MEMS. Consequently, there is a growing interest in both industry and academia in establishing a design process for deterministic AM roughness.

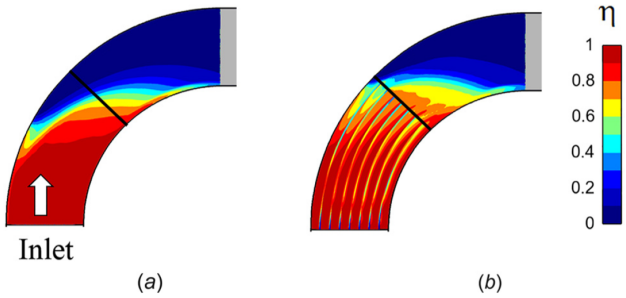
Currently, there is a lack of commercially available computational fluid dynamics (CFD) solvers tailored to this specific purpose, and established correlations for conventional stochastic roughness are not directly applicable to machined roughness, as further elaborated in the literature review. As a result, the predominant approach to the design of surface microstructures is heavily based on experimental testing [35]. However, experimental methods offer limited insight into flow characteristics, reducing the design process to a trial-and-error methodology. The inherent drawback of adopting such an inefficient approach is that it restricts the number of patterns that can be tested, and the reasons behind the varying performance of different patterns remain unclear.

1.1.3 Aerothermal Impact of Surface Structures

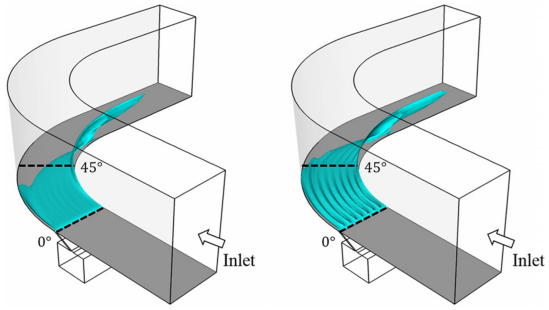
In recent years, deterministic surface structures have gained significant attention in the field of engineering due to their potential to enhance aerodynamics and heat transfer performance. These manufacturable structures offer opportunities for optimizing aerodynamics and thermal performance. Therefore, surface finish manipulation holds the promise of controlling boundary layer behavior, reducing drag, and improving heat transfer efficiency.

For example, in a study conducted by Miao et al. [2], engineered surface structures

were shown to effectively modulate secondary flow within a turbine blade passage, resulting in a notable reduction in its intensity. As depicted in fig. 1.2, the use of a ribbed end-wall was found to guide the purge air flow more efficiently, covering a larger portion of the end-wall surface and consequently enhancing cooling effectiveness. This enhancement can be attributed to the reduction in secondary flow vortex intensity facilitated by rib blockage, while the vortices generated within the rib grooves serve to maintain the cooling air in close contact with the end wall.



(a) Cooling effectiveness



(b) Iso-temperature surface

Figure 1.2: *a) Cooling effectiveness distribution comparison between smooth and ribbed end walls, with the ribbed end wall demonstrating notably superior cooling effectiveness. b) Visualization of iso-temperature surfaces for both cases, illustrating the secondary flow attenuation and enhanced cooling effectiveness achieved with the ribbed end wall. Reproduced from [2]*

The ribs used in this study may not qualify as micro-elements, as they are relatively

large compared to the thickness of the boundary layer (δ/h=4). However, as recommended by the authors, optimizing rib shapes based on factors such as the purge air blowing ratio, blade loading, and incoming flow boundary layer characteristics could lead to an even more efficient configuration different from the one tested. This suggests that the design flexibility offered by additive manufacturing (AM) could enable the implementation of finer surface elements, potentially advancing the utilization of smaller microstructures through AM technology.

Different research groups have investigated surface microstructures, revealing that variations in size, shape, and spacing have a substantial impact on both aerodynamics and heat transfer performance [3, 36]. However, there has been relatively limited exploration of the local flow behavior and the underlying mechanisms that explain why certain surface microstructure arrays outperform others. Although the influence of microstructure geometrical parameters on overall performance has been analysed for some specific applications (e.g. gas turbine pin fin arrays fig. 1.3), a comprehensive examination of local flow phenomena and the interactions between microstructures and the surrounding flow field remains relatively understudied.

The sensitivity of aerothermal performance to the detailed shapes and patterns of regular roughness provides motivation to develop computational methods capable of resolving, rather than empirically modeling, the flow around these microstructures. A significant challenge in this pursuit is the effective simulation of the flow field around a large number of microstructures. The complex flow patterns around each individual element necessitate a fine local mesh, presenting a typical two-scale problem where a

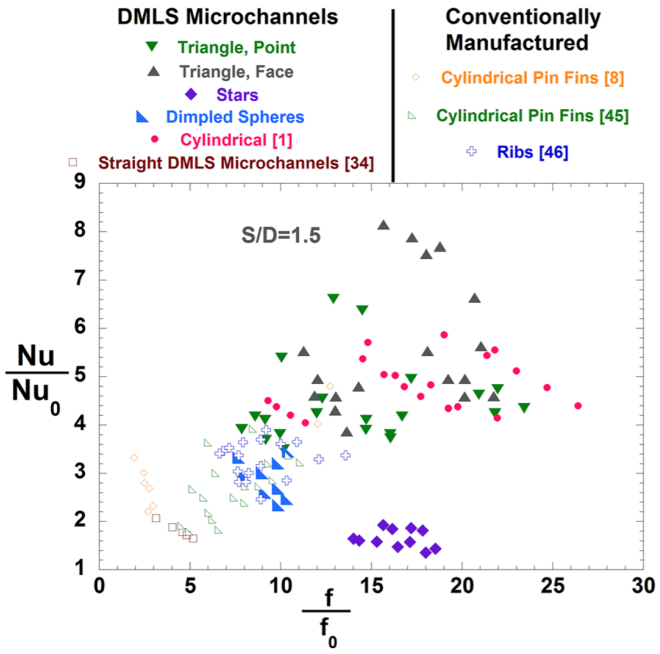


Figure 1.3: *Friction factor augmentation versus Nusselt number augmentation are plotted for all DMLS microchannels manufactured by Ferster et al. [3], straight DMLS microchannels, and conventionally manufactured (relatively smooth-walled) containing pin fins and ribs. Reprinted from [3].*

direct single-scale solution approach is not feasible. Over the years, various multiscale techniques have been developed to address disparities in spatial and temporal scales. Recent progress in these methods suggests their potential applicability to scenarios involving manufacturable surface microstructures [37]

1.1.4 Interactions Between Aerodynamics and Heat Transfer

The introduction of surface microstructures modifies near-wall flow dynamics due to element-to-element interactions, and very little has been done in the literature to effectively study this kind of problem. Furthermore, the manner in which the interaction and potential interplay between aerodynamics and heat transfer influence the local

near-wall flow around these microstructures remains an open research question.

Conventional wisdom often regards convective heat transfer as being completely determined by aerodynamics. According to Newton's law of cooling, the heat transfer coefficient is assumed to be independent of the wall temperature, implying that the flow field is unaffected by wall heat transfer. This view has been frequently questioned, and some empirical correlations have been developed for turbulent flat plate boundary layer flows to account for the fluid-solid temperature ratio (TR) effects [38]. Recently, the interdependence between aerodynamics and heat transfer has been explored for more realistic high-pressure turbine blade geometries [6], revealing that TR has a non-negligible impact on the heat transfer coefficient (HTC) distribution. However, a comprehensive understanding of these interactions is currently limited due to the scarcity of studies in the existing literature and the fact that such studies often rely on Reynolds-Averaged Navier-Stokes (RANS) analysis and smooth surface assumptions.

Additionally, overall observations regarding the impact of wall heat transfer on the laminar-turbulent flow transition for smooth and rough surfaces appear to be inconclusive. Very little has been done in analyzing the transition under the influence of wall heat transfer for surface microstructures, and the interactions between aerodynamics and heat transfer for manufacturable surface structures in general have not been extensively explored.

A potential coupling between heat transfer and aerodynamics would emphasize the need for conjugate heat transfer (CHT) methods to study this potentially nonlinear problem and analyze flows around surface microstructures in the presence of non-

negligible fluid-solid temperature differences [39]. However, the current state of the art has not yet presented a clear case for CHT analysis that justifies the necessity for more sophisticated and expensive approaches to evaluate such heat transfer phenomena. Therefore, the question of whether CHT methods are indispensable remains an open research inquiry. A deeper understanding of the interactions between aerodynamics and heat transfer may provide insight into the applicability and significance of CHT analysis.

In the context of the use of surface microstructures for aerothermal technologies such as gas turbines, it is crucial to consider that these components operate under challenging conditions, particularly in terms of temperature. Elevated temperatures, such as localized temperature spikes on blade surfaces, can potentially affect the durability of machined roughness. Therefore, it is essential to conduct a rigorous evaluation of the temperature distribution and assess the interplay between aerodynamics and heat transfer. This raises a relevant question that this thesis aims to address: in cases of large fluid-solid temperature differences, are there significant interactions between aerodynamics and heat transfer, particularly for surfaces characterised by surface microstructures, and how relevant are these interactions in terms of the aerothermal behavior of a surface?

1.2 Thesis Outline

In light of the preceding considerations, this thesis is structured as follows, with each chapter designed to delve into specific aspects of the research:

- Chapter 2 provides a literature review of previous research on the behavior or regular and random roughness, interactions between aerodynamics and heat transfer, and CFD methods for surface microstructures

- Chapter 3 illustrates heat transfer effects on a flat plate laminar boundary layer focusing on the impact of fluid-solid temperature ratio on the local Reynolds number

- Chapter 4 studies heat transfer effects on flows over a row of surface microstructures under zero pressure gradient, and assesses how the local Reynolds number variation due to heat transfer influences the laminar-turbulent transition

- Chapter 5 analyses flows over an array of surface microstructures under a pressure gradient in adiabatic conditions, comparing the computational results with experimental data found in the literature

- Chapter 6 discusses heat transfer effects on the development of the boundary layer for smooth surfaces and walls characterized by regular roughness subject to a pressure gradient

- Chapter 7 summarises the main findings and highlights the pontential for future development

Chapter 2

Literature Review

The forthcoming literature review provides a comprehensive framework for this DPhil project within the broader context of international academic and industrial research. It serves to underscore the project's alignment with areas where the prior art has exhibited shortcomings. This review is organized into three distinct sections, each dedicated to the exploration of the following aspects:

- The behavior of regular roughness and random roughness: an overview of stochastic roughness characterization, and an assessment of whether conventional parameters used to describe random roughness are adequate for characterizing regular roughness composed of manufacturable surface structures
- Aerodynamics and heat transfer interactions: a review of conventional wisdom treating heat transfer phenomena in fluid flow as a linear problem, criticisms related to the application of Newton's law of cooling for a potentially non-linear problem, and investigation of heat transfer and aerodynamics interactions

- Computational analysis of surface microstructure patterns under significant temperature gradient: a summary of the current state of the art in terms of computational methods that could be used to support the development of manufacturable microstructure arrays such as multiscale techniques and conjugate heat transfer approaches

2.1 Behavior of Regular and Random Roughness

2.1.1 Impact on the Aerothermal Characteristics of a Surface

In the domain of aerothermal research, it is widely acknowledged that surface finish, as a general factor, can have a significant impact on the aerothermal characteristics of flow bounded by a surface, and numerous studies have been conducted to document and emphasize this crucial aspect since the 1930s [40, 41].

Hummel et al. [42], for instance, studied the performance of turbine blades with linear cascade measurements and established a clear relationship between rising Reynolds numbers and the increase in total pressure loss caused by surface roughness, resulting in an increase of up to 40% compared to a hydraulically smooth surface.

Surface roughness intensifies turbulence kinetic energy, turbulence production, and diffusion throughout the boundary layer. The way in which it modifies the turbulence structure is contingent on the specific geometry of the roughness elements, as demonstrated in the study conducted by Tachie et al. [43], which illustrates the effects of surface roughness on the transport and mixing properties within turbulent boundary layers formed in an open channel.

One of the primary challenges in studying surface finish is accurately resolving the near-wall region. Sublayer-resolved Reynolds-averaged Navier–Stokes (RANS) models struggle to predict the behavior of arrays of roughness elements, as pointed out by Altland et al. [44]. Consequently, several DNS studies have been performed to assess the impact of surface microstructures on the boundary layer.

Chatzikyriakou et al. [45], for instance, performed a DNS and LES study of a fully developed turbulent channel flow. Hemispherical roughness elements were strategically placed on the walls in various spacing configurations to investigate their influence on the friction coefficient. The DNS results distinctly reveal different behaviors between the inner wall-layer, which experiences the impact of the roughness elements, and the outer layer, which remains comparatively unaffected. The height of the roughness elements exerts a pronounced influence on the friction factor, the mean velocity profile, and the turbulent stresses. Furthermore, according to their study, for a given element height, the spacing has a less relevant effect on the friction factor and mean velocity profile.

Rizzetta et al. [46] demonstrated that a bypass transition was initiated downstream of the cylindrical roughness elements used in their simulations, caused by the breakdown of an unstable shear layer that formed around the surface of the elements.

Several high-fidelity studies have been undertaken to model and parameterize regular roughness. Orlandi et al. [47], for example, attempted to demonstrate that parameterizing the roughness function using the RMS of the wall normal velocity in the plane of the microstructure crests could be effective in cases where resolving the roughness elements with a fine mesh is not feasible.

Although DNS analysis provides detailed insights, most high fidelity studies are restricted to examining only a few surface microstructures, often just a single element, due to the significant mesh size requirements [48, 49]. This limitation has led to roughness being largely treated as a stochastic attribute and thus empirically modeled, as discussed in the next chapter.

Besides aerodynamic losses, surface finish plays an important role in affecting heat transfer on the gas side of turbine airfoils, as outlined by Abuaf et al. [50]. To achieve high aerodynamic efficiencies and minimize the need for cooling, airfoil designs require precise surface finishing procedures to create smoother surfaces, thus enhancing engine performance. It is important to note that adhering to these stringent standards results in additional manufacturing costs for surface finishing compared to less demanding requirements. The results of Abuaf et al. [50] demonstrate that processes such as tumbling and polishing lead to a reduction in average roughness and subsequent performance improvements.

Engine working cycles cause erosion, corrosion, and other mechanisms that compromise component structural integrity and roughness usually worsening gas turbine performance. Nevertheless, in some cases, roughness is shown to improve the aerothermal properties of a surface, for instance, by eliminating laminar separation bubbles, as illustrated by Goodhand et al. [30]. Similarly, Montomoli et al. [51] observed that a higher level of roughness promotes an earlier transition of the suction side boundary layer of a low-pressure turbine blade, resulting in a reduction in the size of the separation bubble.

Additional evidence on the influence of surface roughness on separation bubbles was provided by Jeong et al. [7]. Their research shows that increased roughness leads to a reduction in the maximum height and length of the separation bubble, without affecting the separation bubble onset location. Increased surface roughness has positive effects on profile loss, specifically in the separated shear layer and reattachment stages.

It enhances turbulent mixing in the separated shear layer, reducing its thickness and momentum deficit. Additionally, it decreases the length scale and turbulence intensity of the shed vortices. Consequently, turbulent mixing and momentum deficit during the reattachment of boundary layers are reduced, resulting in a lower profile loss.

Stripf et al. [29] conducted an experimental study to inspect turbulent transition on a highly loaded turbine vane with nine different roughness configurations which consisted of truncated conical surface elements uniformly distributed on the vane surface. Several different microelement configurations were tested, and transition on the suction surface was seen to move upstream as a result of different sizes and spacing. Height was shown to have a more significant influence on the turbulent transition than spacing. The authors also concluded that the location of the turbulent transition is sensitive even to the finest roughness and significantly affects heat transfer.

Shin et al. [52, 53] experimentally investigated the effects of pressure gradient and surface roughness on turbulent boundary layers. An adverse pressure gradient reduces the roughness effects of increasing the mean velocity defect and normal Reynolds stress, and significantly decreases the integrated streamwise turbulent kinetic energy, friction coefficient, roughness Reynolds number, as well as the roughness effects on integral boundary layer parameters. On the other hand, a favourable pressure gradient enhances the roughness effects.

Rostamy et al. [54] conducted an analysis of how surface roughness influences a turbulent wall jet. Their study examining the impact of surface roughness on the mean flow characteristics of a planar turbulent wall jet concluded that surface roughness has

no effect on the spread rate of the jet. However, it does result in an increase in the streamwise decay rate of the maximum velocity and the thickness of the inner layer.

Yan et al. [55] conducted an investigation into gas flow characteristics within converging-diverging micronozzles with a rectangular cross-section, taking into account the impact of 3D rough surface topography. Their findings reveal that random surface roughness disrupts the velocity field near the wall, and this perturbation can extend throughout the entire flow field. In the case of subsonic flow, this perturbation is predominantly confined to the vicinity of the wall and has negligible effects in the central region of the nozzle. However, when dealing with supersonic flow in the divergent portion, the perturbation can induce the formation of supersonic multiwaves, leading to significant fluctuations in flow parameters. The intensity of these waves increases with greater surface roughness heights.

Film cooling may be affected in different ways by surface roughness depending on the blowing ratio, as shown by Cardwell et al. [56]. At the higher blowing ratio, a noticeable decline in adiabatic effectiveness attributed to roughness was observed, whereas at the lower blowing ratio, cooling remained essentially unaffected.

Erickson et al. [57] studied the impact of surface roughness on heat transfer using a linear cascade rig. In their study, realistic roughness appeared to have no influence on heat transfer rates as long as boundary layers remained laminar. Realistic roughness led to an early transition in all cases, and the transition onset appeared to be independent of the inlet turbulence condition. Furthermore, variations in Reynolds numbers had a limited effect on the transition location, highlighting that the initiation of transition

is markedly influenced by the specific roughness characteristics present on realistically rough surfaces.

The impact of surface roughness on the laminar-turbulent transition was also studied by Lorenz et al. [58], who detected an upstream transition shift on the suction side of a low-pressure turbine blade with increasing roughness height. They also carried out experiments on rough surfaces composed of truncated cones of comparable height. Each of these sets of roughness elements exhibited distinct geometric anisotropy characteristics: some had a circular base shape, while others featured an elliptical base shape stretched in the spanwise direction, and another group of roughness elements was stretched in the streamwise direction. Their study revealed that roughness anisotropy had a similar impact as roughness height. When dealing with streamwise stretched roughness, as seen in scenarios like particle deposits, the transition from laminar to turbulent flow occurred significantly further downstream compared to isotropic roughness. Conversely, spanwise stretched roughness elements induced an earlier transition point, moving it considerably upstream.

The research by Lorenz et al. [58] additionally showed that the total heat load on both the pressure and suction sides with roughness increased by approximately 100%. A notable increase in pressure-side heat transfer was observed primarily in the presence of heightened roughness or spanwise stretched roughness elements. In fully rough turbulent boundary layers, this heat transfer enhancement was found to be unrelated to the Reynolds number and instead dictated by the geometry of the roughness elements. Furthermore, the heat transfer within the turbulent boundary layer displayed a sig-

nificant dependence on anisotropy. Specifically, heightened turbulent heat transfer was associated with spanwise stretched roughness, while diminished heat transfer was linked to streamwise stretched roughness when compared to isotropic roughness elements.

In general, the surface finish interacts with a range of flow mechanisms, including suction side separation, freestream turbulence, pressure gradients, secondary flows, film cooling, and overall unsteadiness. This implies that the influence of the surface finish is intertwined with these flow mechanisms that affect its impact on the flow field. Consequently, numerical predictions become case-specific, making it necessary to assess surface roughness within the relevant flow conditions to ensure accurate predictions.

2.1.2 Limits of Conventional Parameters for Roughness Characterization

During the past century, numerous studies have aimed to define the behavior of surface roughness, e.g. Whitehouse et al. [59]. Yet, questions persist regarding the sufficiency of conventional parameters for this purpose, such as the equivalent sandgrain height k_s, the centerline height R_a, the mean height μ, the roughness skewness or the peak-to-valley distance. The introduction of new roughness parameters has sparked both criticism and support within the scientific community. For instance, Thomas [60] raised concerns about the redundancy of some of these parameters, while others, such as Gadelmawla [61], argue that the complex nature of real surface geometry necessitates a greater number of parameters for a comprehensive description. Thus, the drive to

introduce new parameters for surface evaluation is in part a response to this need for increased descriptive accuracy.

Bogard [62] conducted an analysis on two turbine vanes from military aircraft engines, which had accumulated 500 hours of service, revealing a substantial increase in surface roughness, more pronounced on the pressure side. The analysis involved detailed profilometer measurements that provided comprehensive roughness profiles on vane surfaces. It was found that the commonly used parameters for characterizing surface roughness, such as the centerline average R_a and the average peak value, were insufficient in predicting the impact of surface roughness on flow and heat transfer. Instead, the study identified a correlation between surface friction and heat transfer with the equivalent sandgrain roughness k_s, first introduced by Schlichting [41] to correlate different shapes of roughness with the well-documented surface roughened with emery paper.

Sigal et al. [63] introduced a novel roughness density parameter, which is determined by multiplying the ratio of total surface area to total frontal area by a shape factor that considers the average inclination of the windward surface of the roughness elements. This newly introduced parameter is used to create associations that describe the shifting characteristics of the logarithmic wall profile when dealing with two and three-dimensional roughness elements. In instances where the roughness density parameter is small in magnitude, the equivalent sand grain roughness calculated from this novel correlation closely corresponds with earlier observations. Nevertheless, when this parameter assumes higher values, notable disparities become apparent.

The two most commonly used methods for conducting viscous simulations involve the utilization of wall functions, such as the law of the wall with adjustments for representing roughness effects in near-wall flows, or the integration of equations of motion from the wall using a turbulence model that incorporates a correlation for roughness effects. In both the wall function and the turbulence model approaches, it is essential to characterize the actual roughness, typically in terms of its equivalent sandgrain roughness, k_s, or similarly, in terms of the shift C it induces in the law-of-the-wall intercept. To enhance the characterization of standard roughness, improvements have been suggested by Waigh [64] that consider the shape of the roughness elements. These improvements account for their bluntness and spanwise aspect ratio to reduce uncertainties.

Although there is a degree of agreement regarding the overall trends, our current ability to develop precise models to forecast the impact of roughness on profile losses and surface heat transfer remains limited. As noted by Bons [65], this limitation arises primarily from the extensive parameter space needed to comprehensively characterize roughness, encompassing factors like size, shape, or spacing. Furthermore, he points out that the use of equivalent sand-grain roughness characterization, k_s, does not take into account the different effects of roughness on skin friction, heat transfer, and boundary layer transition.

While several studies indicate that the effects of roughness spacing and skewness are relatively small compared to roughness height [51, 66], it should be noted that topological characteristics significantly impact the aerothermal performance of surface

roughness, particularly for surfaces with comparable roughness heights. For example, in the case of Goodhand et al. [67], it is argued that well-established parameters, such as the centerline-averaged roughness (R_a) and the equivalent sandgrain roughness (k_s), prove to be insufficient. Instead, they suggest taking into account the detailed roughness topology and using the roughness slope as the key topographical parameter, characterized by normalizing the roughness amplitude with wavelength.

While Goodhand et al. [67] proposed a solution involving a single parameter to characterize roughness, Kapsis et al. [34], in agreement with the findings of Lorenz et al. [58], demonstrated that regular roughness exhibits a significant directionality effect arising from the element-to-element length scale. This observation highlights the limitation of relying solely on a single roughness spacing parameter such as the roughness slope. Their corresponding findings for regular microstructures emphasize that the detailed shapes and patterns of regular roughness have substantial effects on practical aerodynamic and heat-transfer performance.

On the one hand, the importance of roughness shape and spacing suggests a fundamental difference between regular roughness and random roughness, on the other hand regular roughness is often used in the literature to study the beavior of random roughness. Gramespacher et al. [68] and Stripf et al. [29], for instance, used deterministic roughness to study the influence of surface finish on transitional boundary layers with an unambiguous description of surface topography. Although there appears to be a qualitative similarity in the behavior of regular and random roughness, the relevance of detailed microstructure shapes and spacings of regular roughness may introduce a

distinction between the two types of roughness, as suggested by Kapsis et al. [34]. Consequently, it is uncertain to what extent we can compare the behavior of random and deterministic roughness and whether distinct parameters should be utilized in their characterization.

2.2 Limits to the Application of Newton's Law of Cooling

The concept of heat transfer coefficient, even if not necessarily called so, was first introduced by Sir Isaac Newton, who observed that the hot objects cooled at a rate proportional to the difference between their temperature and that of the surroundings. As mentioned by Moffat et al. [4], in the 1920's, the increasing interest towards internal flows challenged the definition of heat transfer coefficient, given that there was no free-stream temperature to use as the reference, and suggested the use of the bulk mean fluid temperature instead. Around 20 years later, in the context of high speed flows, heat transfer rates were found to be proportional to the difference between the wall temperature and its adiabatic temperature instead of the free-stream temperature, however, this finding had a limited impact in terms of industrial practise at the time.

In the 1970s and 1980s, increasing attention was directed toward problems involving abrupt changes in heat fluxes and wall temperatures. This highlighted the challenge of dealing with unknown wall temperatures and the need for parameters that remain unaffected by wall temperature variations. Thus, Moffat et al. [4] introduced a novel

approach aimed at analyzing situations where wall temperature is not constant and is often unknown: the adiabatic heat transfer coefficient, which employs the wall adiabatic temperature as the reference temperature. Unlike the earlier definition of the heat transfer coefficient (HTC), this was shown to be invariant of the thermal boundary condition, as illustrated in fig. 2.1. Therefore, this new heat transfer coefficient is commonly calculated for a known wall temperature field (e.g. a low-temperature lab testing or an empirical correlation), and then used for thermal design to evaluate the temperature field in other conditions (e.g. a high-temperature operational condition) using nondimensional parameters like Nusselt number and Biot number.

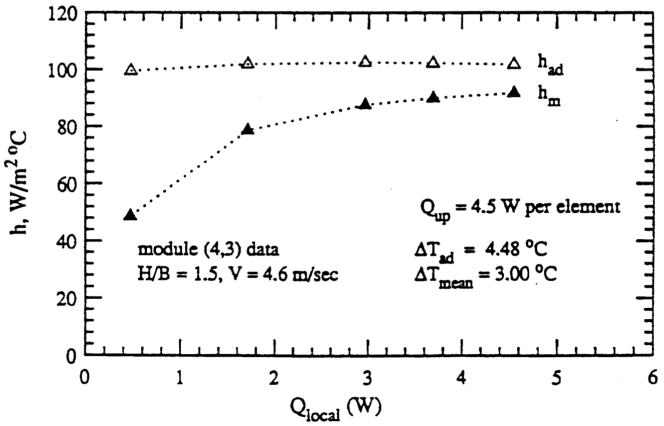


Figure 2.1: *Thermal boundary condition independency of $h_{adiabatic}$. Reprinted from Moffat [4].*

The foundations of Newton's law of cooling and the associated concept of heat transfer coefficient are fundamentally established on the premise of isothermal walls [69]. This leads to two pivotal questions: Can we straightforwardly calculate the heat transfer coefficient and then adapt it for different operational conditions, even when non-isothermal walls are in play? Does Newton's law of cooling hold true for scenarios

involving nonisothermal walls? He [70] explored these inquiries and deduced that the heat transfer coefficient derived under isothermal conditions does not hold applicability for nonisothermal scenarios, with the associated errors being generally deemed unacceptably large. This underscores the pressing need for alternative frameworks and methodologies to address convective heat transfer over nonisothermal surfaces.

A way of dealing with problems characterised by non-constant thermal boundary conditions is the discrete Green's function approach developed by Hacker and Eaton [71] which consists in discretizing the surface of interest into a finite number of elements and relating the heat flux out of any element (q_j) to the wall temperature disturbances caused by all other elements (ΔT_{w_i}) weighted by their respective local influence coefficients ($G_{i,j}(U)$) as illustrated in eq. (2.1). This method eliminates the necessity for the concept of a heat transfer coefficient, as illustrated by Eaton et al. [72, 73], but with a comprehensive Green's function description of a scenario, it becomes possible to determine both the adiabatic heat transfer coefficient and the wall adiabatic temperature. Additionally, discrete Green's function analysis could be used to deal with conjugate heat transfer problems as illustrated by Eaton [74].

$$q_j = \sum_i G_{i,j}(U)\Delta T_{w_i} \tag{2.1}$$

However, Green's function methods encounter practical challenges due to the substantial computational burden, given that each mesh point on a wall surface can potentially be affected by all other mesh points on the same surface. Furthermore, the use

of coarser wall partitions may introduce uncertainty, as it leads to lower resolution in both the representation of thermal disturbances and the computation of local responses for the specific mesh point under consideration. Thus, given that the main problem of the Green's function analysis is the locality of the functions, He [70] proposed a Spectral Heat Transfer Coefficient (SHTC) approach where the temperature disturbance is globally defined as the sum of the contributions of different modes rather than the sum of the contributions of different local elements. As a result, when the number of modes under consideration is significantly fewer than the number of mesh points, this approach leads to considerably more cost-effective computations. Furthermore, this framework can be used for nonisothermal surfaces, and closely resembles the conventional definition of Heat Transfer Coefficient (HTC), as demonstrated in eq. (2.2), where C_m is the magnitude of temperature disturbance for mode m, and H_m is an HTC-like parameter:

$$q(x, y) = \sum_m C_m H_m \tag{2.2}$$

Nevertheless, it must be remarked that Green's function and SHTC approaches, similarly to the definition of adiabatic HTC, rely on the assumption of linear energy equations which translates into the decoupling of aerodynamics and heat transfer. Therefore, the effects of heat transfer on fluid properties and their consequential impact on aerodynamics is entirely neglected when using discrete Green's function analysis.

2.3 Aerodynamics and Heat Transfer Interactions

When substantial temperature differences exist between the freestream and the wall, a coupling between the aerodynamic and thermal fields takes place, as emphasized by Ekret et al. [75] and Kays et al. [76]. Under those conditions the Nusselt number can be affected by the fluid-solid temperature ratio (TR) due to compressibility effects and variations in gas properties with temperature through the boundary layer. Fitt et al. [38] conducted both experimental and numerical investigations on this matter, specifically focusing on the effect of the temperature ratio on laminar and turbulent boundary layers over a flat plate. Their findings indicated that the variation in fluid properties has a non-negligible impact on the Nusselt number.

Nevertheless, very often in practical applications related to the thermal fatigue design of hot components, an HTC distribution is derived assuming that heat transfer and aerodynamics are uncoupled as illustrated by Moffat [4]. Then, the Nusselt number (Nu) is used to scale HTC to the working conditions of interest. Subsequently, a straightforward conduction equation is employed to determine the temperature field within the solid. In this conventional approach to heat transfer analysis, aerodynamics is deemed the sole determinant of the heat transfer coefficient. By assuming that HTC is unaffected by wall temperature, a linear relationship between heat flux and temperature difference (ΔT_{f-s}) is established. According to such an approach, HTC could be calculated through a linear system by working out the heat flux for two arbitrary wall temperatures. The two-temperature method offers a suitable approximation for

scenarios with sufficiently small temperature gradients, where the HTC can be considered primarily determined by aerodynamics. On the other hand, if HTC depends on ΔT and T_w, the dependence between the heat flux and ΔT is non-linear, as Maffulli et al. [5] and illustrated in fig. 2.2.

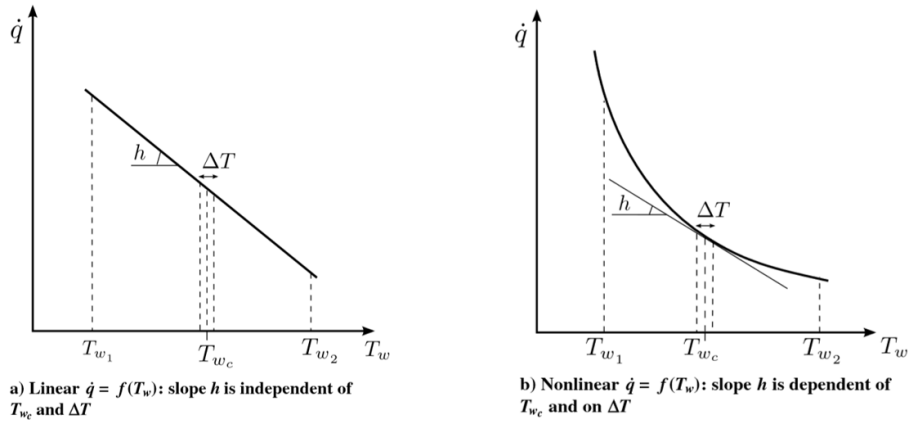


Figure 2.2: *The two-temperature method accurately predicts HTC distribution only when HTC and wall temperature (T_w) are aerodynamically determined. Otherwise, when HTC relies on temperature difference (ΔT) and T_w, the heat flux-ΔT relationship becomes nonlinear. Reprinted from [5]*

The study conducted by Maffulli et al. [6] sheds light on the interdependence between aerodynamics and heat transfer in high-pressure turbines. It demonstrates that neglecting the influence of wall temperature on HTC leads to inaccurate heat transfer predictions for transonic blades. The study reveals that, when using the conventional two-point method, the local discrepancy in HTC for a 3D nozzle guide vane passage can be as high as 30-40% (as shown in Figure 2.3). In high-pressure turbine walls, heat flux is associated with a significant temperature difference. Hence, the near-wall flow experiences notable density variations and consequential rebalancing of density and velocity. The authors introduced a three-point nonlinear method for localized HTC correction.

By solving three linear equations, this method effectively predicts HTC distributions within the NGV passage, resulting in a substantial reduction in errors and an enhancement in stability. Nevertheless, it must be remarked that this is a RANS study and a high-fidelity analysis of the interactions between aerodynamics and heat transfer would be necessary to confirm those findings.

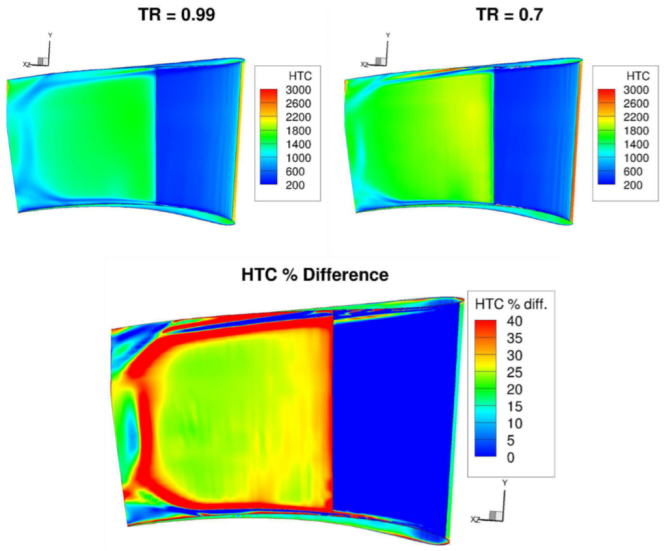


Figure 2.3: *The HTC distributions on the suction surface of a nozzle guide vane passage for two temperature ratios (TR) are compared. Using the conventional two-point heat transfer method results in local discrepancies of up to 30-40%. Reprinted from [6]*

Another engineering application where the impact of the wall thermal boundary conditions is often neglected is over-tip-leakage (OTL) in turbomachinery. The numerical analysis conducted by Zhang et al. [77] shows a significant impact of the wall-gas temperature ratio on the transonic OTL flow field. This analysis also highlights a strong two-way coupling between aerodynamics and heat transfer. This observation underscores the need for localized correction of temperature dependence when using

HTC for blade metal temperature predictions without resorting to a fully conjugate solution.

In general, it appears that while the definition of heat transfer coefficient has evolved over the years with the introduction of $h_{adiabatic}$, and the use of other invariant descriptors, such as the Green's function and SHTC, based on the assumption of linear energy equations, has been explored, the interactions between aerodynamics and heat transfer have received limited attention in the existing literature. Neglecting this critical coupling could potentially lead to inaccurate predictions of both heat transfer and aerodynamics, especially in scenarios involving significant temperature gradients.

2.3.1 Impact of Heat Transfer on Turbulent Transition

Several studies have been conducted on the laminar-to-turbulent transition, with a specific emphasis on the impact of wall cooling and heating. Previous investigations have delved into these aerothermal processes, providing insight into the complex interactions between fluid dynamics and heat transfer during this transition phase.

Shadloo et al. [78], for instance, conducted a study on the impact of heat transfer on the transition within flat plate supersonic boundary layers. Through the application of Direct Numerical Simulations (DNS), they detected an earlier transition when wall cooling is introduced.

Following the initial work by Braslow et al. [79], several researchers focused on supersonic flows over cone nose-tip geometries. Buntin et al. [80], for instance, show that for sharp nose-tips cooling and heating would correspondingly have a stabilizing

and destabilizing effect. On the other hand, they also reported the opposite behavior for blunt nose-tips: cooling and heating would promote and delay the transition, respectively.

Fedorov et al. [81] studied with a DNS approach a sharp cone at zero angle of attack under a free-stream Mach number 6 condition, and concluded that cooling decreases the second-mode disturbance amplitude and delays the transition, and heating produces an opposite and less pronounced effect. Other researchers like Zhu et al. [82] experimentally studied the laminar-to-turbuent transition over a cone under a Mach number 6 free stream. Specifically, they employed an instability-enhanced flared cone in their study. Their findings demonstrated that increasing the ratio T_w/T_0 initially postpones the transition to turbulence, but subsequently promotes it, with the reversal point occurring around $T_w/T_0 = 1$. It should be noted that the primary distinction between the work of Zhu et al. [82] and that of Fedorov et al. [81] lies in the geometry of the cone used. This distinction underscores the substantial influence of geometric factors on the mechanisms that govern the transition in supersonic flows, which was also suggested by Buntin et al. [80].

In the subsonic flow regime, Schafer et al. [83, 84] studied the impact of wall heat transfer on transition using linear stability theory. In particular, they modified the incompressible stability equations to account for the variation of temperature dependent fluid properties across the boundary layer, and found that cooling destabilizes low-speed water flows but stabilizes air flows. Their results align with the experimental work by Liepmann and Fila [85] who highlighted the destabilizing effect of heating on air flows

caused by the variation of near-wall viscosity, which leads to a thicker boundary layer and a velocity profile that is more prone to transition.

In contrast with the aforementioned findings referred to as a natural transition, other studies [86–88] show that cooling promotes the bypass transition even if such behavior is opposite to what was expected from the small disturbance stability theory. These results seem to be qualitatively in agreement with those observed experimentally by Back et al. [89].

The current state of understanding regarding the influence of wall heat transfer on the transition from laminar to turbulent flow remains rather inconclusive given the strong dependence on geometrical factors and different behavior of natural and bypass transition. It is also important to emphasize that previous research efforts on transition mainly concentrate on smooth surfaces. However, a noticeable gap exists in the analysis of the transition under the influence of wall heat transfer, particularly when considering surface microstructures. This highlights an area in need of further investigation to enhance our understanding of these complex interactions.

2.4 CFD Analysis of Surface Microstructure arrays

2.4.1 Conjugate Heat Transfer Approaches

As discussed in section 2.3, in the presence of non-negligible fluid-solid temperature differences, the coupling between heat transfer and aerodynamics could have a significant effect for applications of practical interests. Additionally, the presence of surface mi-

crostructures can substantially influence the local near-wall flow because of the element-to-element interactions, emphasizing the need for conjugate heat transfer methods to study this potentially nonlinear aerothermal problem.

For the first time, in 1961, Perelman [39] suggested the use of conjugate heat transfer (CHT), and in the last 50 years, various research groups around the world have worked on the development of CHT solvers. Dorfman et al. [90] published a review of the analytical CHT solutions available and their applications. The interdependence of aerodynamics and heat transfer can be taken into account by iterating CFD solutions and FE solid conduction. Approaches based on this concept are defined as loosely coupled since they require two different solvers for solid and fluid and a continuous exchange of boundary conditions at the solid-fluid interface. Because of the different mesh sizes at the fluid solid-interface an interpolation, which does not guarantee energy conservation, is necessary. Moreover, in the case of large ΔT, the flow characteristics tend to be sensitive to the temperature of the wall and can cause convergence problems. Various strategies have been implemented to fix this problem, but none of the methods in the literature is unconditionally stable, as indicated by Verstraete et al. [91].

Another possibility is to adopt fully coupled unconditionally stable methods that exploit a single solver for both fluid and solid domains. One of the main issues related to conjugate heat transfer solvers is the time-scale disparity between fluid and solid. This problem is not relevant for steady solutions but affects in a prominent way transient simulations [92]. Fully coupled unsteady CHT simulations using the same discretization in space and time for both fluid and solid domains can be extremely expensive.

Loosely coupled CHT methods are more popular because of such fluid-solid time scale discrepancy, and the fluid side is conventionally assumed to behave in a quasi-steady way. However, this assumption may cause non-negligible errors in certain applications. Hence, He et al. [93] developed a new multiscale framework for the fluid domain formulated in a triple-timing form. As the authors explain, the slow-varying temporal gradient corresponding to the time scales in the solid domain has been included in the fluid equations as a source term. In the meantime, fast fluid unsteadiness is captured by a local-time integration at a given frozen large scale time instant. Such a time desynchronization is adopted to accelerate the unsteady CHT solution. Nevertheless, a large time desynchronization may lead to consistent aliasing errors. Moreover, when an eddy-resolving method is used, directly coupled CHT solutions are affected by an extra mesh dependency in the solid domain, as illustrated by Shahi et al. [94].

Subsequently, He [95] developed a closely coupled nonpartitioned CHT solver which applies a moving average to the time-mean flow and a discrete Fourier transform at each time step. By using a semi-analytical transfer function and harmonic balancing for the CHT interface, the solid domain is solved entirely on its own time step, which is 3-5 orders of magnitude larger than the time step of the fluid domain. Such a method is not affected by aliasing problems and extra solid domain mesh-dependence in case of application of eddy-resolving approaches.

A similar approach, in which fluid and solid are coupled in the frequency domain instead of the time domain to avoid the time scale disparity issue, was adopted by Hickling et al. [96] in the context of rotating cavities. This approach is effectively a

reformulation of the method developed by He [95] to deal with high-frequency temperature fluctuations. The authors linked monochromatic low-frequency temperature fluctuations from large coherent structures in the fluid domain to a time-spectral solid-domain solution using a harmonic balance interface condition. Simultaneously, broad-band higher-frequency temperature fluctuations from turbulence were captured locally on the wall with a wall transfer function approach.

The increased computational cost associated with CHT methods deter their widespread adoption in the design phase of aerothermal technologies. Nevertheless, for specific applications such as surface microstructures, where the temperature distribution can profoundly impact surface finish durability, it is advisable to evaluate the extent to which the interplay between aerodynamics and heat transfer contributes significantly. For highly nonlinear scenarios, where the two-way feedback between aerodynamics and heat transfer cannot be disregarded, the adoption of CHT approaches is recommended.

2.4.2 Multiscale Methods

The traditional approach to addressing two-scale problems relies predominantly on empirical methods. Microscale effects are typically modeled, such as through modified wall boundary conditions, while larger-scale disturbances are resolved. However, the sensitivities of aerothermal performance to the detailed shapes and patterns of regular roughness illustrated in section 2.1.2 provide a motivation to develop computational methods to be able to resolve, rather than empirically model, the flow around these microstructures. The major challenge faced then is to solve the flow field around a

huge number of microstructures to predict the effect on a microstructured surface of interest. This presents a typical two-scale problem, as the high-gradient flow around each element requires a fine local mesh. Solving this directly with a single-scale solution strategy is prohibitive, suggesting that the use of a multiscale solver could be a potential solution to address this challenge.

Several multi-scale approaches based on a finite element formulation have been developed for problems characterized by distinctive spatial scales [97–101], showing the potential of multi-scale solvers to address problems that would be difficult to treat otherwise, mainly for incompressible flows. Moreover, other methods have been established to deal with the different temporal scales of solid and fluid under transient thermal coupling [92, 93, 102].

A novel block spectral model for compressible flows has been developed by He [103–105] to finely resolve small-scale flow features while avoiding a globally fine mesh for parts of the domain that can be solved with a coarser grid, and tested for film cooling and dimples. The primary objective of this finite-volume model is to ensure uniformity in the numerical discretization scheme and integration method for both coarse and fine scales so that the numerical resolution is solely dictated by the mesh size. Its primary constraint is the assumption of steady or quasi-steady flow, which makes it unsuitable for handling small-scale turbulence and self-excited unsteadiness, as the flow field would lose the required smoothness in terms of block-to-block variations necessary for spectral mapping. He [106] then updated his block spectral approach with the capability to deal with unsteady flows. This formulation consists in dividing the domain into several small

blocks, and only a small set of blocks needs to be solved with a fine mesh resolution. The solution is obtained by coupling the local fine mesh solution and the global coarse mesh solution through a block spectral mapping that propagates source terms to areas with coarse mesh only. In this way, the coarse solution is influenced by the fine mesh even where there is no local fine mesh embedded. The global coarse mesh solution provides boundary conditions to the local fine mesh blocks, while the local fine mesh solution provides the source terms to the global coarse mesh domain. A more recent version of the block spectral method previously discussed has been developed by Kapsis and He [107]. Their primary objective was to parallelize the block spectral solver, enhancing its efficiency in managing domains characterised by large surface microstructure arrays. The method's effectiveness in handling a substantial quantity of micro-elements was demonstrated through a test case involving 4000 surface microstructures.

In cases with significant differences in temperature between fluid and solid components, consideration of conjugate heat transfer approaches is warranted, as discussed in section 2.3. To serve this purpose, He's CHT approach [95], has been integrated with his multiscale solver [106] to create a two-scale CHT method [108]. Such a solver is capable of computing the flow around numerous surface microstructures while capturing the interactions between aerodynamics and heat transfer.

The advancements in the realm of multiscale solvers have demonstrated the potential to resolve, rather than relying on empirical modeling, the flow around surface microstructures, thus opening up possibilities for their design. These multiscale approaches are still in the development phase and have not yet experienced widespread

industrial implementation.

2.5 Remarks

The literature review initially provides an overview of various research endeavors investigating the influence of roughness on the aerothermal characteristics of surfaces. Based on the papers presented, it is evident that the surface finish substantially influences the surface behavior, intensifying turbulence kinetic energy, turbulence production, and diffusion throughout the boundary layer. Moreover, different and hard-to-generalize effects on the flow field and performance parameters manifest due to roughness, depending on the domain and the specific boundary conditions of interest.

The characterization of surface roughness remains a complex challenge. Despite extensive research spanning many years, it still raises several ongoing questions. The adequacy of parameters used for characterizing random roughness behavior is not definitively clear, and directly comparing characteristics between random and regular roughness continues to be a subject of inquiry. This uncertainty is due to the significant impact of the detailed shape, size, and spacing of the microstructures comprising regular roughness on aerothermal performance, which complicates direct comparisons with random roughness.

The engineering of regular roughness for aerothermal applications necessitates a focus on its durability under demanding temperature conditions and the development of techniques for accurately predicting temperature distribution. Thus, this literature

review explores the historical perspective on the conventional definition of the heat transfer coefficient (HTC) and the ongoing criticism regarding its accuracy and significance. In fact, in several cases discussed in this chapter, the conventional wisdom that views HTC as fully aerodynamically determined led to inaccurate heat transfer predictions. Hence, the present review emphasizes the importance of employing conjugate heat transfer analysis in cases with significant temperature differences where the flow field and temperature field are likely to be coupled.

Overall, it seems that both in industrial practice and academic research, the interactions between aerodynamics and heat transfer are not thoroughly discussed, and the few pubblications available tend to rely on low-fidelity RANS analysis. This is attributed to the complexity of the problem, which would potentially require either conjugate heat transfer analysis or high-temperature laboratory testing, both costly solutions. Although some researchers have addressed the limitations of conventional wisdom that views the heat transfer coefficient as solely determined by aerodynamics, the difficulty of implementing more accurate methods means that scaling the heat transfer coefficient for the conditions of interest using the Nusselt number remains the most common approach. Consequently, this method is very rarely questioned, as it is often seen as the only viable alternative, and the error caused by its application remains unclear. Furthermore, in the context of surface microstructure flows and transition mechanisms, published findings related to such interactions are generally inconclusive. This, combined with the need to resolve the flow field around engineered roughness arrays rather than relying on empirical modeling due to the significance of the specific

shapes and spacing of surface microstructures within such arrays, underscores the potential of multiscale solvers for this kind of applications. Therefore, the literature review discusses various multiscale solvers, their associated challenges in the context of surface microstructure arrays, and their integration with conjugate heat transfer approaches to capture potential interactions between aerodynamics and heat transfer.

Based on the insights gained from this literature review, the following research questions are proposed to address the gaps and challenges identified:

- How would variations in local fluid properties caused by heat transfer affect the flow field in the case of a flat plate boundary layer and in the presence of surface microstructures?

- What is the key parameter that could be used to assess the interactions between aerodynamics and heat transfer?

- What is the impact of such interactions on transition and can we use an incompressible flow model to predict transition under the influence of heat transfer, particularly given the incompressible model being often adopted for transition studies?

- How does the interplay between aerodynamics and heat transfer manifest itself in realistic gas turbine applications, such as in the presence of a pressure gradient and separation bubbles?

- How do interactions between flow and thermal fields feature in the case of a surface

microstructure array undergoing such a pressure gradient?

In particular, the following chapters are dedicated to exploring and addressing these research questions comprehensively. Each chapter is designed to build upon the insights gained from the previous sections, ensuring a coherent investigation into the interplay between aerodynamics and heat transfer. The specific focus of each chapter is outlined as follows:

- Chapter 3 delves into the heat transfer effects on a flat-plate laminar boundary layer, with an emphasis on how the fluid-solid temperature ratio impacts the local Reynolds number. This chapter lays the groundwork using a simple configuration
- Chapter 4 extends the investigation to flows over a row of surface microstructures under a zero pressure gradient. It examines the influence of heat transfer on the local Reynolds number and its subsequent effect on the laminar-turbulent transition. This analysis is crucial for comprehending the behavior of more complex surface geometries
- Chapter 5 analyzes flows over a larger array of surface microstructures subjected to a pressure gradient in adiabatic conditions. This chapter compares computational results with experimental data found in the literature, providing a critical validation of the simulation set-up used
- Chapter 6 discusses the heat transfer effects on the development of the boundary layer for both smooth surfaces and walls characterized by regular roughness under

a pressure gradient. This chapter integrates the insights from previous chapters with results obtained in a more realistic environment

- Chapter 7 summarizes the main findings of the research and highlights the potential for future developments in this field

Chapter 3

Heat Transfer Effects on a Flat-Plate Laminar Boundary Layer

As indicated in section 2.3, the interplay between aerodynamics and heat transfer has received limited attention in both academic research and practical industrial settings. This holds true even for fundamental scenarios like laminar boundary layers on flat plates, where the implications of deviating from linear energy equations on flow behavior remain unclear. Therefore, the principal aim of this chapter is to conduct a comprehensive analysis of the interactions between aerodynamics and heat transfer within the context of laminar flat plate boundary layers.

In the following sections, the computational method and the case setups are introduced. Subsequently, the laminar boundary layer on a flat plate is first presented for validation. The results at different wall temperatures are then compared to highlight how wall heat transfer can influence the flow field, fluid properties, and performance parameters in different yet consequential ways.

3.1 Computational method and set-up

Laminar simulations are performed to study the flow field using compressible Navier-Stokes equations as the governing equations (eqs. (3.1) to (3.3)), where u is the velocity vector field, q represents the heat flux due to thermal conduction, τ the viscous stress tensor, f represents body forces such as gravity, e is the total energy per unit mass, k is the thermal conductivity and S represents any sources or sinks of energy.

Continuity Equation:

$$\frac{\partial \rho}{\partial t} + \nabla \cdot (\rho u) = 0 \tag{3.1}$$

Momentum Equations:

$$\frac{\partial (\rho u)}{\partial t} + \nabla \cdot (\rho u u) = -\nabla p + \nabla \cdot \tau + f \tag{3.2}$$

Energy Equation:

$$\frac{\partial (\rho e)}{\partial t} + \nabla \cdot (u(\rho e + p)) = \nabla \cdot (\tau \cdot u) + \nabla \cdot q + S \tag{3.3}$$

Low-speed flows have been analysed (M<0.3), and the compressible flow model is used to capture the effects on the flow field of fluid properties variations due to heat transfer. The commercial codes ANSYS ICEM and FLUENT are used for mesh generation and flow simulation, respectively. A pressure-based finite-volume method with a pressure-velocity coupled scheme is adopted.

Historically, density-based solvers were favored for high-speed compressible flows due to their direct calculation of the density field. However, advancements in commercial solvers such as ANSYS FLUENT have expanded the functionality of pressure-based solvers to effectively handle a wide range of flow conditions, including low-speed flows that exhibit variations in fluid properties within the boundary layer due to thermal effects.

The inlet total temperature T_{01} is taken to be $280K$, and the wall temperature is set to a uniform value to match the prescribed temperature ratio (TR), defined as T_w/T_{01}. The boundary conditions are set to ensure a fully laminar flow field, therefore no inlet turbulence is present, and P_{01} as well as P_2 are set to a uniform value so that Re_L=130000. Air properties such as thermal conductivity and specific heat capacity vary with temperature according to air properties tables. Dynamic viscosity is based on Sutherland's law and density on the ideal gas law. The exit pressure is set to atmospheric pressure.

The flow domain is illustrated in fig. 3.1. The upstream part of the domain is inviscid, so the boundary layer starts at the leading edge location indicated in fig. 3.1, where the viscous wall begins. The top boundary is specified as an inviscid wall, and the height of the domain is large enough (H/L=2.5) to ensure that the continuity deficit caused by the growth of the boundary layer is negligible.

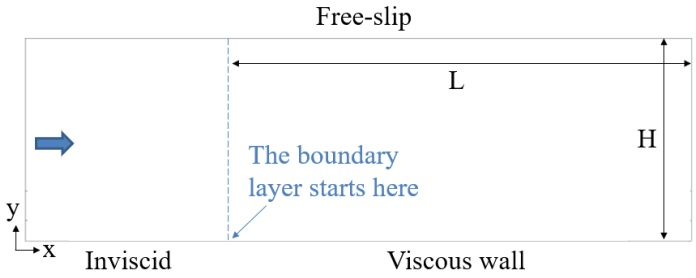


Figure 3.1: *Flat plate boundary layer domain (height and length are to the scale H/L=2.5).*

3.2 Flat plate boundary layer under different TRs

This section serves as a fundamental validation and assesses the influence of fluid property and velocity variations, due to wall heat transfer, on performance parameters for a flat-plate laminar coundary layer. A local Reynolds number parameter is introduced to describe the impact of wall cooling/heating on the flow field. The flow domain used is described in section 3.1.

3.2.1 Basic validation and mesh sensitivity

A 2D mesh is produced using ANSYS ICEM, and a mesh refinement study is carried out testing three different mesh sizes in adiabatic conditions at Re_L=130000. All grids produce consistent results in agreement with the Blasius solution, as illustrated in fig. 3.2. The mesh used for this effectively 2D case is composed of 300k elements.

3.2.2 Impact of wall temperature

Three different wall temperatures are tested keeping the same Reynolds number value Re_L=130000: TR=0.5 (cooled wall), TR=1 (adiabatic), and TR=1.5 (heated wall).

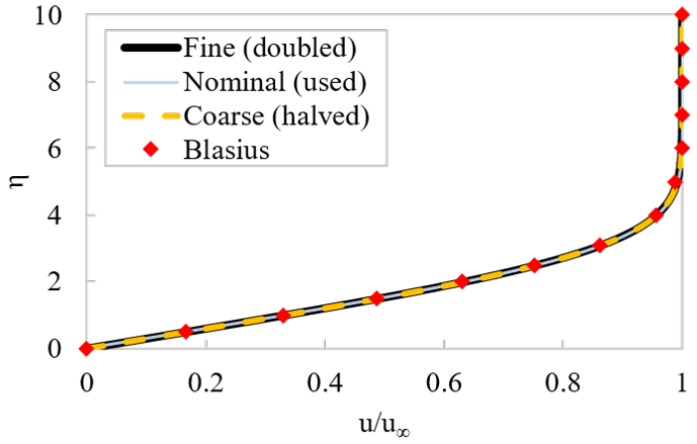


Figure 3.2: *Mesh dependency study for flat plate boundary layer*

Different TRs necessarily lead to different temperature fields, thus rather than looking at changes in the temperature field with TRs, a more relevant aspect is how the flow (velocity) field may respond to the wall heat transfer. The resulting velocity profiles are compared with the Blasius solution. Wall heating significantly thickens the boundary layer, in agreement with what Arnal [87] reported, and the opposite trend is detected for wall cooling, as illustrated in fig. 3.3. TR=1.5 and TR=0.5 show respectively a ±20% variation in boundary layer thickness and ±50% difference in displacement thickness. Similarly to the adiabatic case, the velocity profiles $u(\eta)$ at TR=0.5 and TR=1.5 are also laminar and self-similar along the flat plate.

To measure the influence of wall cooling/heating on performance parameters, TR=1.5 and TR=0.5 are compared with the adiabatic case (TR=1). The Nusselt number for TR=1 is obtained using the Reynolds-Colburn analogy as shown in eq. (3.4). The reason why the Nusselt number at TR=1 is not taken from the simulation is that Nu is effectively a nondimensional heat flux q, normalized by the driving temperature

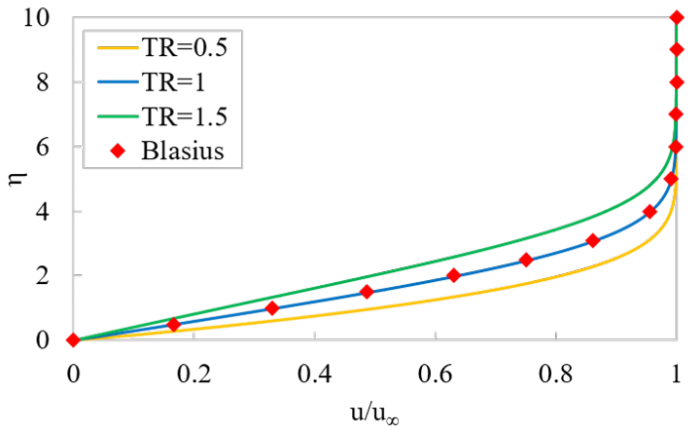


Figure 3.3: *Impact of TR on the velocity profile*

difference ($T_{01}-T_w$) and other parameters. For the adiabatic case ($TR = 1$), the normalization of q will singularly fail (i.e. $T_{01}-T_w$=0). Therefore, the Reynolds-Colburn analogy (where q is not explicitly needed) is used instead.

$$Nu_{L_{TR1}} = \frac{C_{D_{f_{TR1}}}}{2} Re_L \, Pr^{1/3} \tag{3.4}$$

In a seemingly contradicting behavior with the significant effect on the velocity profile depicted in fig. 3.3, the impact of TR on the drag coefficient and the Nusselt number appears to be quite small, as reported in table 3.1.

Table 3.1: *Impact of TR on performance parameters for a flat-plate laminar boundary layer*

TR	$Nu_L/Nu_{L_{TR1}}$	$C_{D_f}/C_{D_{f_{TR1}}}$
0.5	1.01	1.03
1.5	0.98	0.97

The explanation for this rather contradicting observation is the compensating effect

of viscosity and velocity gradient on wall shear stress ($\tau_w = \mu\frac{\partial u}{\partial y}$). Wall cooling, for instance, causes viscosity to drop significantly in the near-wall region. On the other hand, the velocity gradient substantially increases due to the velocity profile variation, as illustrated in fig. 3.4. The adiabatic values of the viscosity and velocity gradient at the wall are used as a reference in fig. 3.4.

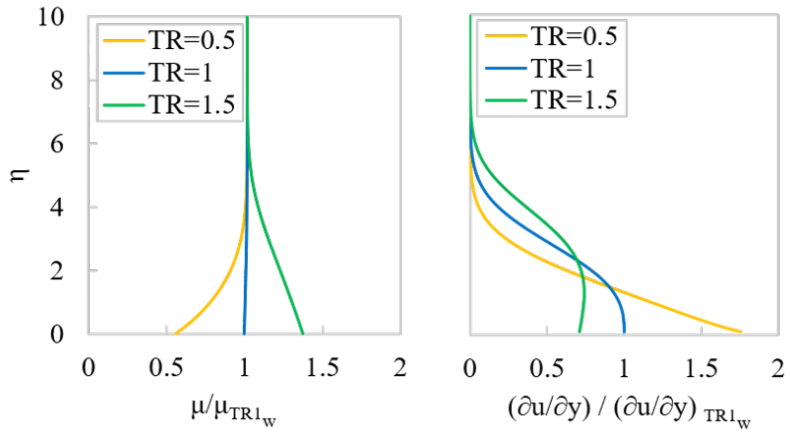


Figure 3.4: *Profiles of dynamic viscosity and velocity gradient at different wall temperature conditions non-dimensionalized using adiabatic values at the wall*

The effects of TR on viscosity and velocity gradient cancel each other out, leading to $C_{D_f}/C_{D_{f_{TR1}}} \sim 1$. Similarly, in the case of wall heating (TR=1.5), the viscosity increases and the velocity gradient decreases in the proximity of the wall, implying an exiguous variation of the frictional drag coefficient. The compensating effects of viscosity and velocity gradient result in a negligible net impact of TR on performance parameters, which effectively masks the substantial differences in the flow field caused by wall cooling/heating. A question then arises: which parameter is more suitable to describe the impact of TR on flat plate boundary layer flows? The definition of Reynolds number

based on free-stream variables overlooks the significant variation of fluid properties and velocity profile in the boundary layer caused by heat transfer. To assess the influence of wall heat transfer on the flow field across a boundary layer, Maffulli and He [5] introduced a nondimensional aerothermal parameter that represents the local Reynolds number, and is calculated using local fluid properties and velocity. Similarly, in the present study, a local Reynolds number is defined as a function of x and η in eq. (3.5), which should not be mistaken for the commonly used Reynolds number based on the local distance $Re_x{=}\rho_\infty\, u_\infty\, x/\mu_\infty$.

$$Re_{local}(x,\eta) = \frac{\rho(x,\eta)\;\; u(x,\eta)\;\; x}{\mu(x,\eta)} \tag{3.5}$$

At any given x location, the Re_{local} profile is a function of the wall normal distance η only. The impact of TR on $Re_{local}(\eta)$ is quantified in fig. 3.5, where the local Reynolds number profiles are depicted for three different wall temperatures. Wall cooling implies a higher near-wall density, lower viscosity, and a thinner boundary layer. All of these effects contribute to the increase in the local Reynolds number, as illustrated in fig. 3.5.

Now we consider the cooled wall case more closely. Unlike the performance parameters for which viscosity and velocity gradient play a compensating role, fluid properties and velocity variations caused by wall cooling have an additive effect on the local Reynolds number. Therefore, to separately assess the contributions of velocity, density, and viscosity, additional parameters are defined in eq. (3.6): $D_{tot}(\eta)$ is the total variation in the local Reynolds number; $D_u(\eta)$ measures the influence of velocity variations

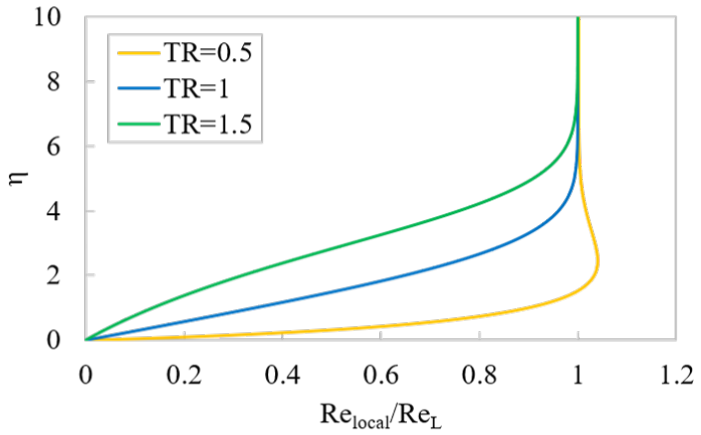


Figure 3.5: *Local Reynolds number profile*

due to wall cooling on the local Reynolds number profile; $D_\rho(\eta)$ the influence of density; and $D_\mu(\eta)$ the influence of viscosity. The value of the local Reynolds number at the adiabatic condition (TR=1) is taken as a reference.

$$
\begin{aligned}
Re_{local}(\eta)_{TR1} &= \frac{\rho(\eta)_{TR1}\, u(\eta)_{TR1}\, x}{\mu(\eta)_{TR1}} \\
D_{tot}(\eta) &= \frac{\boldsymbol{Re_{local}(\eta)_{TR05}} - Re_{local}(\eta)_{TR1}}{Re_{local}(\eta)_{TR1}} \\
D_u(\eta) &= \frac{\frac{\rho(\eta)_{TR1}\, \boldsymbol{u(\eta)_{TR05}}\, x}{\mu(\eta)_{TR1}} - Re_{local}(\eta)_{TR1}}{Re_{local}(\eta)_{TR1}} \\
D_\rho(\eta) &= \frac{\frac{\boldsymbol{\rho(\eta)_{TR05}}\, u(\eta)_{TR1}\, x}{\mu(\eta)_{TR1}} - Re_{local}(\eta)_{TR1}}{Re_{local}(\eta)_{TR1}} \\
D_\mu(\eta) &= \frac{\frac{\rho(\eta)_{TR1}\, u(\eta)_{TR1}\, x}{\boldsymbol{\mu(\eta)_{TR05}}} - Re_{local}(\eta)_{TR1}}{Re_{local}(\eta)_{TR1}}
\end{aligned}
\tag{3.6}
$$

The contributions of velocity, density and viscosity variations, due to wall cooling, on the local Reynolds number profile, are represented in fig. 3.6. Those results lead to the following observations: the three parameters $D_u(\eta)$, $D_\rho(\eta)$, and $D_\mu(\eta)$, show a significant impact near the wall (roughly about 90% each); the contribution of density

is the most significant at the wall; for η>0.5, velocity is the most impactful factor in increasing the local Reynolds number; the contribution of density is larger than that of viscosity.

In proximity of the wall (η<1), for TR=0.5, $Re_{local}(\eta)$ reaches values five times higher than the adiabatic profile (TR=1). The near-wall effect is considerable in the case of wall heating (TR=1.5) as well, $Re_{local}(\eta)$ is reduced by over 60% (see fig. 3.5). The significant impact of TR on the local Reynolds number distribution is not confined to the near-wall region, and affects almost an entire boundary layer up to η=5.

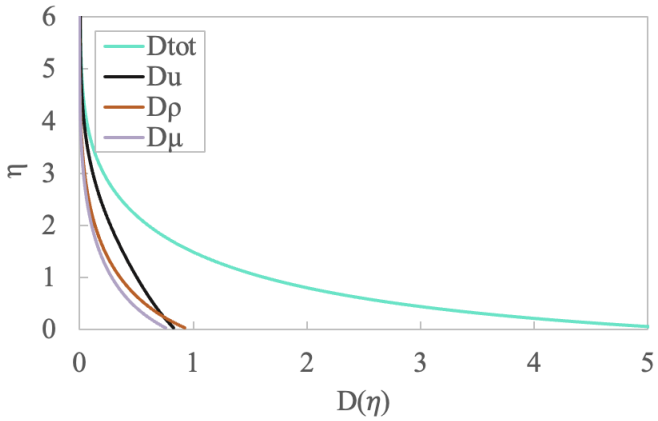


Figure 3.6: *The contribution of velocity, dynamic viscosity, and density to increasing Re_{local} in the near-wall region for TR=0.5*

It should be noted that these findings are not universally valid. Different fluids with different Prandtl numbers can exhibit distinct heat transfer behaviors. For instance, water shows relatively small density variations with temperature, and its viscosity increases with a cooled wall. This could potentially lead to lower local Reynolds number values when the temperature ratio (TR) is below 1.

These Re_{local} profiles discussed in this chapter clearly illustrate that heat transfer

has a nonnegligible impact on the flow field even if the friction drag coefficient and Nusselt number do not reflect such an effect. Thus, one can easily be misguided if judging the influence of wall heat transfer on aerodynamic flow field purely based on these two basic aerothermal performance parameters.

In the next chapter, the local Reynolds number variation due to wall cooling/heating, as well as its implication on aerodynamics, will be studied for a surface microstructure array.

3.3 Remarks

Basic validation and sensitivity studies are conducted for a flat plate laminar boundary layer. Subsequently, three wall-inflow temperature ratio (TR) values are analyzed: a cooled wall (TR=0.5), an adiabatic wall (TR=1), and a heated wall (TR=1.5).

At first, a seemingly contradicting observation is made: the common aerothermal parameters C_{D_f} and Nu appear to be largely insensitive to wall heat transfer, but the velocity profiles are substantially affected by TR. It turns out that a compensating effect is at play between the fluid viscosity and the velocity gradient in the boundary layer, leading to the heat transfer influence on the flow being largely 'masked' if judged based only on C_{D_f} and Nu. This finding led the authors to explore the local Reynolds number as a more useful indicator of the influence of heat transfer on the flow field.

It is further observed and backed up by a detailed examination of the contributions to the local Reynolds number from each fluid property or flow variable that a cooled wall

leads to a very significant increase in the local Reynolds number within the boundary layer, while a heated wall leads to a reduction. The local variation of fluid properties and their impact on the local Reynolds number distribution are also confirmed in the next chapter for an array of surface microstructures.

Chapter 4

Heat Transfer Effects for a Surface Microstructure Array

Enhanced understanding and prediction of aerodynamics and convective heat transfer characteristics for surface microstructures have been frequently pursued in the literature and are further motivated by the rapid development of additive manufacturing (AM) technologies in recent years. In the context of aerothermal design and management of high-temperature components, convective heat transfer is typically regarded as predominantly driven by fluid flow. An issue of interest is the interaction between the heat transfer and the flow field, and more specifically, if and how heat transfer may affect the flow field. Thus, the goal of this chapter is to study the interactions between aerodynamics and heat transfer for an array of manufacturable surface microstructures.

The flow field around an array of microstructures is analyzed for a fully laminar and a fully turbulent flow, respectively. The emphasis is on how changes in local flow velocity and fluid properties due to heat transfer can most relevantly alter the local

Reynolds number, as observed for the flat-plate laminar boundary layer in chapter 3. Additionally, the transition behavior under different nominal Reynolds numbers is computed at different TRs. The results are also contrasted with those predicted by an incompressible-flow model to address its applicability under the influence of heat transfer, even though in a nominally incompressible low-speed flow regime. The calculated aerothermal performance results in the transition regime are also further reformulated to account for the temperature ratio in a unified nondimensional form independent of the amount of wall heat transfer.

To summarise, this chapter aims to address the following research questions:

- What are the relationships and potential interplay between aerodynamics and heat transfer when surface microstructures are introduced?
- How would changes in local flow and fluid property influence the Reynolds number, and how should we evaluate those effects?
- To what extent is the applicability of the incompressible flow model valid in scenarios involving significant heat transfer?

4.1 Computational method and set-up

Large Eddy Simulation (LES) are performed to solve the compressible Navier-Stokes equations. Low-speed flows have been analysed (M<0.3), and the compressible flow model is used to capture the effects on the flow field of variations in fluid properties

due to heat transfer. The commercial codes ANSYS ICEM and FLUENT are used for mesh generation and flow simulation, respectively. A pressure-based finite volume method is adopted with a pressure-velocity coupled scheme, as recent enhancements in commercial solvers such as ANSYS FLUENT have broadened the capabilities of pressure-based solvers to a wide range of flow conditions, including low-speed flows that exhibit variations in fluid properties within the boundary layer due to thermal effects.

The inlet total temperature T_{01} is taken to be $280K$, and the wall temperature is set to a uniform value to match the prescribed temperature ratio (TR), defined as T_w/T_{01}. Air properties such as thermal conductivity and specific heat capacity vary with temperature according to air properties tables. The dynamic viscosity is based on Sutherland's law and the density on the ideal-gas law. The exit pressure is set to atmospheric pressure. Performance parameters are calculated as follows:

- Nusselt number: $Nu_r = \frac{hr}{k}$
- Drag coefficient: $C_D = C_{D_f} + C_{D_p}$

It must be specified that the heat transfer coefficient was calculated as $h{=}q/(T_w{-}T_{01})$. Although the two-point method would have produced more accurate estimates of h, it would have required running two simulations for each Re_r and TR value of interest. This approach was deemed too computationally expensive for transitional/turbulent cases, which require extensive computational resources to achieve time-averaged flow and thermal fields. Accepting that evaluating h based on a one-point approach could lead to inaccuracies in cases of significant fluid-solid temperature differences, as pointed

out by Maffulli et al. [5], the choice of T_{01} or T_{ad} as the reference temperature for the one-point evaluation of h does not significantly affect the results at the low speeds considered ($M < 0.3$), where these two values are relatively close. Therefore, for simplicity and to reduce computational cost, T_{01} was chosen as the reference temperature.

In this case, the bottom surface of the domain is subject to a row of eight hemispherical microstructures of radius r in the streamwise direction with periodic side boundaries in the z direction, as illustrated in fig. 4.1. No-slip and free-slip conditions are applied respectively to the wall surface and the top boundary. The inlet total pressure profile is prescribed so that the resulting inlet velocity profile is always laminar and matches the Blasius solution. The inlet boundary layer thickness is fixed at $20r$ so that according to the Blasius solution $20r=\frac{5x}{\sqrt{Re_x}}$, thus $\frac{x}{\sqrt{Re_x}}=4r$. A Blasius-like inlet velocity profile $u_{in}(\eta)$ can then be defined as $\eta=\frac{y\sqrt{Re_x}}{x}=\frac{y}{4r}$ and $u_{in}(\eta)=u_\infty u_{Blasius}(\eta)$, where u_∞ is the desired free-stream velocity for the Re_r value of interest. The total pressure inlet profile is finally calculated using $u_{in}(\eta)$. Various Reynolds number values (Re_r) are tested by adjusting the total pressure profile. It is important to specify that $Re_r=(\rho_\infty u_\infty r/\mu_\infty)$ is the globally defined Reynolds number, using the microstructure radius as the length scale.

In this chapter, the interdependence between heat transfer and aerodynamics is analysed for a surface microstructure array at different Reynolds numbers ranging from laminar to turbulent flows. The flow domain is shown in fig. 4.1, and the inlet total pressure profile is specified so that the resulting inlet velocity profile is laminar and matches the Blasius solution as illustrated in fig. 4.2.

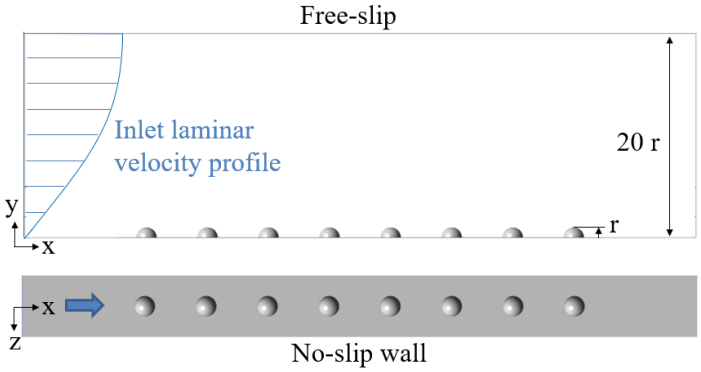


Figure 4.1: *Surface microstructure array domain: a row of eight hemispherical surface microstructures of* $500\mu m$ *radius*

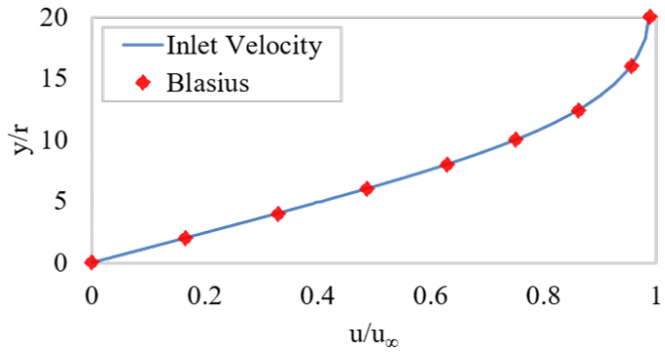


Figure 4.2: *Inlet velocity profile, obtained by specifying a total pressure profile to match the laminar Blasius solution as shown*

For low Re_r (laminar cases), the flow over the microstructures leads to a steady recirculation region (fig. 4.3a). On the other hand, for higher Reynolds numbers (turbulent cases), turbulent separation takes place (fig. 4.3b), and a scale-resolving approach is required. The LES method is adopted without an explicit subgrid model. This is effectively an implicit LES, and is preferred to capture a transition process without the subgrid model interfering with the laminar flow part, e.g He [109]. To practically determine whether a case is laminar or transitional/turbulent, simulations were conducted in both steady and transient modes using ANSYS FLUENT. If the instantaneous flow field from the transient mode is constant in time and matches that of the steady-mode

simulation, the case is deemed laminar. The critical Reynolds number was identified as the smallest value of Re_r for which ANSYS FLUENT produces different flow fields in transient and steady modes.

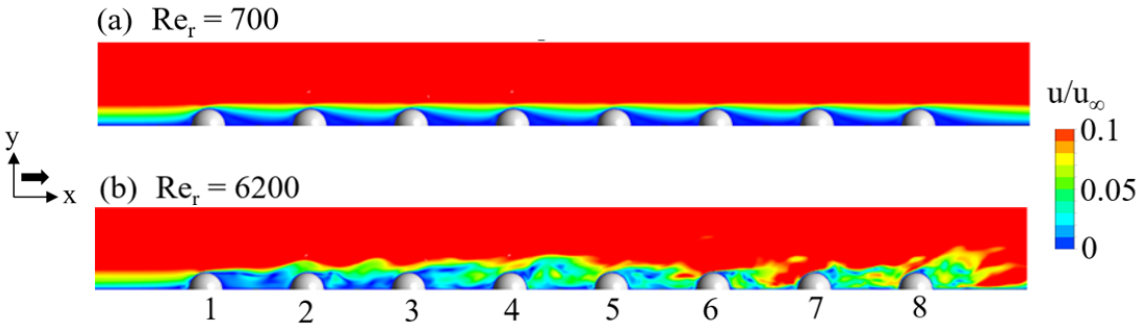


Figure 4.3: *Velocity contours, a) Laminar flow field Re_r=700, b) Turbulent flow field Re_r=6200*

Vorticity iso-surfaces for a laminar and a turbulent case are presented in fig. 4.4. To achieve consistent laminar and LES results, mesh and time step sensitivity studies are carried out as described in the next section.

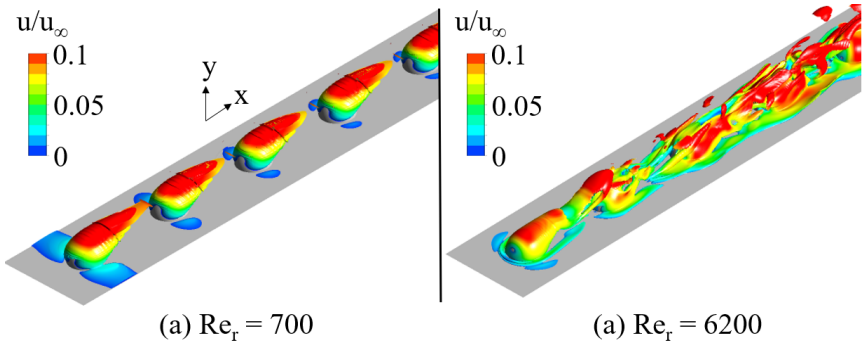


Figure 4.4: *Vorticity iso-surfaces colored with u values: a) laminar, b) turbulent*

4.2 Numerical sensitivity study

The assessment of numerical sensitivity is carried out for a surface microstructure array in the turbulent regime (Re_r=4000) with TR=0.5. A 3D mesh is generated using ANSYS ICEM. A structured multiblock approach is adopted to consistently refine the near-wall region. The flow domain around each hemispheric microstructure is meshed with an o-grid as depicted in fig. 4.5.

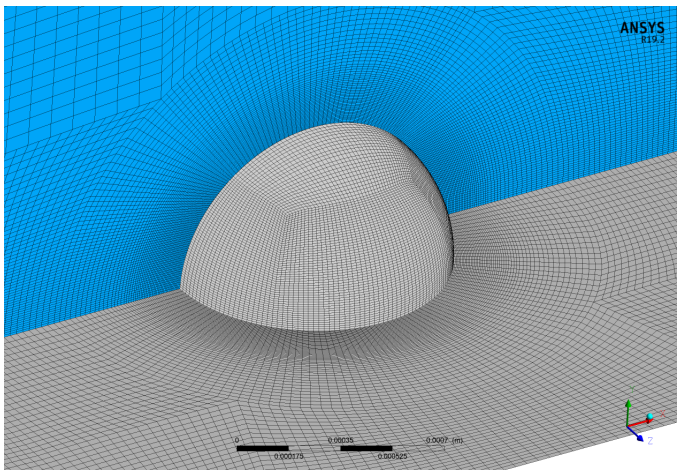


Figure 4.5: *O-grid mesh around one of the microstructures*

For the mesh dependency study, two grids are tested: 10M and 15M elements. The discrepancy caused by using the coarse mesh (10M) is less than 1% as reported in table 4.1. Similarly, in the time-step dependency study, two time-step sizes are assessed: Δt_{nd}=$time\ step/throughflow\ time$=0.002, and Δt_{nd}=0.001, see table 4.2. These time-step sizes effectively capture the unsteady flow separation caused by the surface microstructures, as the period of the main frequency of the spectrum - calculated for a point in the wake of the last microstructure in the row - is approximately 1000 times larger than the time step corresponding to Δt_{nd}=0.002. Given the small discrepancies,

a 10M element mesh, and a time-step size of Δt_{nd}=0.002 are considered sufficiently accurate to resolve turbulent cases.

Table 4.1: *Mesh size sensitivity for an array of surface microstructure*

$Mesh\ size$	$\overline{Nu_r}$
10M	5.30
15M	5.29

Table 4.2: *Time step size sensitivity for an array of surface microstructure*

Δt_{nd}	$\overline{Nu_r}$
0.002	5.30
0.001	5.32

For laminar cases, convergence is assumed when a steady state is reached. For turbulent cases, convergence is measured based on time-averaged Nusselt number. It is observed that after a sampling period of 5 through-flow times, the differences between two through-flow periods fall to less than 2%, as illustrated in fig. 4.6. Sampling starts once the flow field is is judged to be fully developed, which is reached after 5 through-flow periods.

4.3 Laminar flow results

In the present section, several wall temperatures are tested for the same Reynolds number (Re_r=720). A quasi-adiabatic case (TR=0.98) is used as reference, since the Reynolds analogy might not be suitable to calculate the reference Nusselt number

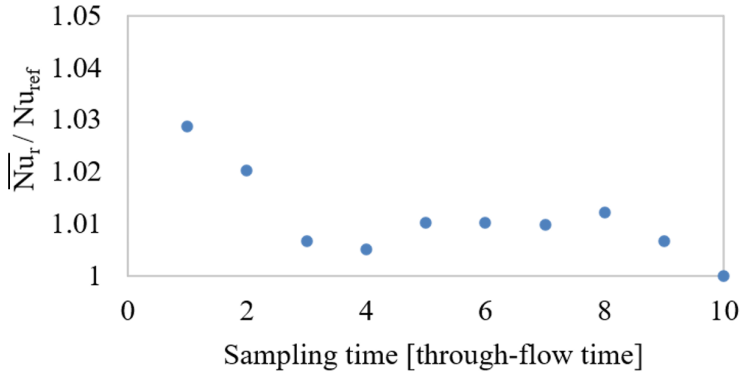


Figure 4.6: *Sampling time length study. The reference value Nu_{ref} is $\overline{Nu_r}$ after sampling for 10 through-flow times*

($Nu_{TR=1}$) for this kind of geometry where a pressure gradient is introduced by the microstructures, and the definition of $h{=}q/(T_w{-}T_{01})$ would singularly fail for $TR{=}T_w/T_{01}{=}1$.

4.3.1 Local Reynolds number effect

Similarly to the flat plate boundary layer analysis illustrated in figs. 3.5 and 3.6, the influence of the wall temperature on Re_{local} for an array of surface microstructures is first examined. In particular, the difference in $Re_{local}(x, y)$ between $TR{=}0.5$ and the reference quasiadiabatic case ($TR{=}0.98$) is depicted on an xy plane taken at $z{=}0$ (mid-plane cut). For the given z value, the definitions of the local Re differences introduced

in eq. (3.6) can be adapted as described in eq. (4.1).

$$
\begin{aligned}
D_{tot}(x,y) &= \frac{\boldsymbol{Re_{local}(x,y)_{TR05}} - Re_{local}(x,y)_{TR098}}{Re_{local}(x,y)_{TR098}} \\
D_u(x,y) &= \frac{\frac{\rho(x,y)_{TR098}\ \boldsymbol{u(x,y)_{TR05}}\ r}{\mu(x,y)_{TR098}} - Re_{local}(x,y)_{TR098}}{Re_{local}(x,y)_{TR098}} \\
D_\rho(x,y) &= \frac{\frac{\boldsymbol{\rho(x,y)_{TR05}}\ u(x,y)_{TR098}\ r}{\mu(x,y)_{TR098}} - Re_{local}(x,y)_{TR098}}{Re_{local}(x,y)_{TR098}} \\
D_\mu(x,y) &= \frac{\frac{\rho(x,y)_{TR098}\ u(x,y)_{TR098}\ r}{\boldsymbol{\mu(x,y)_{TR05}}} - Re_{local}(x,y)_{TR098}}{Re_{local}(x,y)_{TR098}}
\end{aligned}
\tag{4.1}
$$

The total changes in the local Reynolds number, D_{tot}, caused by TR variations are plotted in fig. 4.7. Wall cooling substantially increases Re_{local} near the surface microstructure array, showing an overall consistent picture with that of a flat plate boundary layer in fig. 3.5. Nevertheless, a significant difference is observed in the upper part of the recirculation regions, where negative D_{tot} values are detected locally (region indicated with 'A' in fig. 4.7).

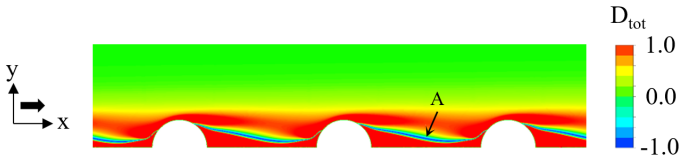


Figure 4.7: *Impact of TR=0.5 on Re_{local} for an array of surface microstructures*

Individual contributions of local velocity, density, and dynamic viscosity, to the Re_{local} variation, are depicted in fig. 4.8. In line with the flat plate boundary layer analysis, both local density, and dynamic viscosity contribute to the increase in the local Reynolds number, and the local density shows a more marked impact than the dynamic

viscosity (fig. 4.8b-c). On the other hand, the behavior of local velocity (fig. 4.8a) differs significantly from the flat plate case, resulting in negative D_u values in the separation regions (area indicated with 'A' in fig. 4.8a). The results in fig. 4.8 suggest that the local velocity is responsible for the negative D_{tot} regions illustrated in fig. 4.7.

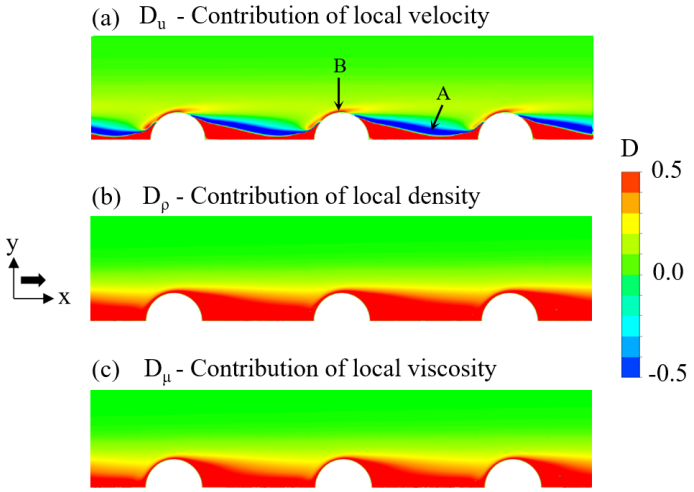


Figure 4.8: *The contribution of velocity, dynamic viscosity and density to increasing Re_{local} in the near wall region for TR=0.5*

To understand why the contribution of local velocity D_u differs significantly between a flat plate boundary layer and a surface microstructure array, the impact of TR on the velocity field in a mid-cut plane (z=0) is shown in fig. 4.9. Wall cooling (TR=0.5) increases the near wall density resulting in higher local fluid inertia, and delayed reattachment. Inversely, in the heated wall case (TR=1.5), the reduced density near the wall corresponds to an earlier flow reattachment. Therefore, wall cooling is seen to increase the size of the recirculation zone and vice versa for the wall heating.

Unlike what is observed for a flat plate boundary layer, where no flow separation takes place, in the case of hemispherical microstructures, the D_u contour (fig. 4.8a) is

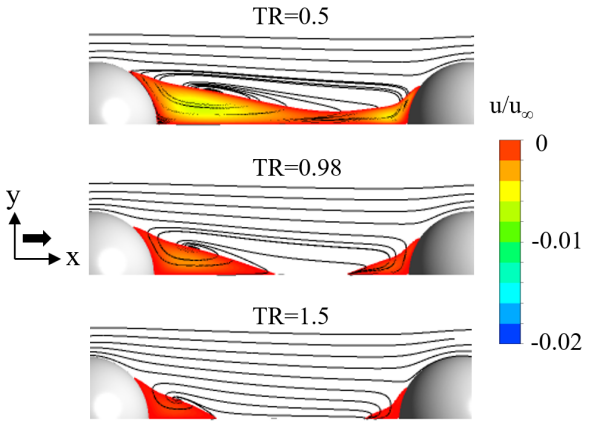


Figure 4.9: *Impact of TR on the velocity field near surface microstructures. The contour is clipped at u/u_∞=0, thus reversed flow only is depicted*

influenced by the shape and size of the recirculation region, which is dependent on TR. The enlarged separation of the cooled wall case (TR=0.5) corresponds to a local region ('A' in fig. 4.8a) where the velocity is lower compared to the adiabatic reference case. Consequently, a significant local negative contribution from the velocity changes to the local Reynolds number is illustrated in fig. 4.8a. On the other hard, similar to the flat plate boundary layer (fig. 3.3), the frontal surface attached boundary layer (marked as 'B' in fig. 4.8a) shows higher local velocity for the cooled wall case. Rather contrasting velocity contributions around the flow separation over the hemisphere surface are observed: there is a positive contribution of the frontal part where the boundary layer is attached, but the contribution becomes sharply negative right after the separation.

The same study is carried out for the heated wall case (TR=1.5). Consistent with the flat plate boundary layer findings (fig. 3.5), the near-wall Re_{local} values show an overall reduction due to wall heating, as indicated in fig. 4.10. Meanwhile, a significant difference is detected in the recirculation region, where D_{tot} reaches positive values in

'A' (flipped compared to TR=0.5).

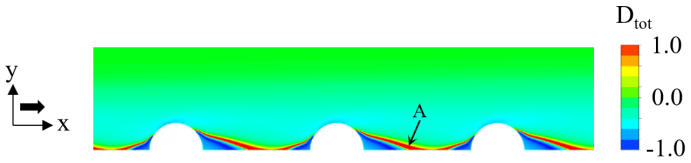


Figure 4.10: *Impact of TR=1.5 on Re_{local} for an array of surface microstructures*

The individual contributions of local velocity, density, and dynamic viscosity, to the Re_{local} variation for TR=1.5, are depicted in fig. 4.11. The reduced separation region in the heated wall case translates into higher local velocity in the upper part of the recirculation areas ('A' in fig. 4.11a), and is responsible for the D_{tot}>0 regions indicated with 'A' in fig. 4.10.

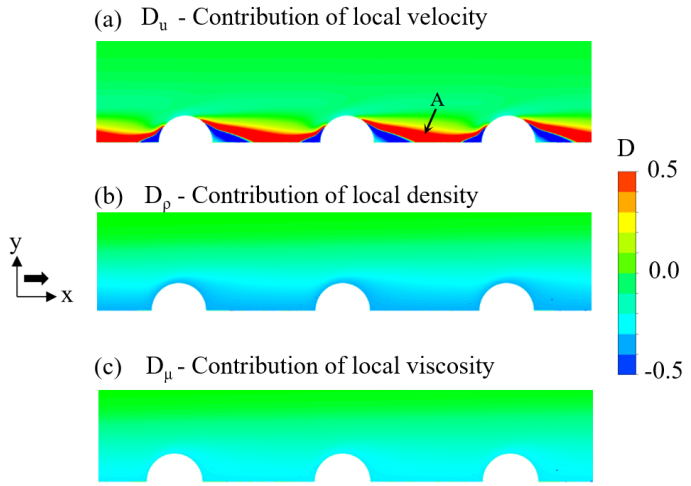


Figure 4.11: *The contribution of velocity, dynamic viscosity and density to reducing Re_{local} in the near wall region for TR=1.5*

4.3.2 Impact of TR on aerothermal parameters

In this section, the influence of TR on performance parameters is studied for an array of hemispheric surface microstructures in the laminar regime (Re_r=720). The variation of Nusselt number (Nu_r) due to heat transfer, is illustrated in fig. 4.12a, showing that Nusselt number increases as the local Reynolds number grows (high near-wall Re_{local} for TR=0.5, see fig. 4.7). Compared to the flat plate boundary layer where the impact of TR on performance parameters is negligible (see table 3.1), wall cooling (TR=0.5) increases Nu_r by ∼15%.

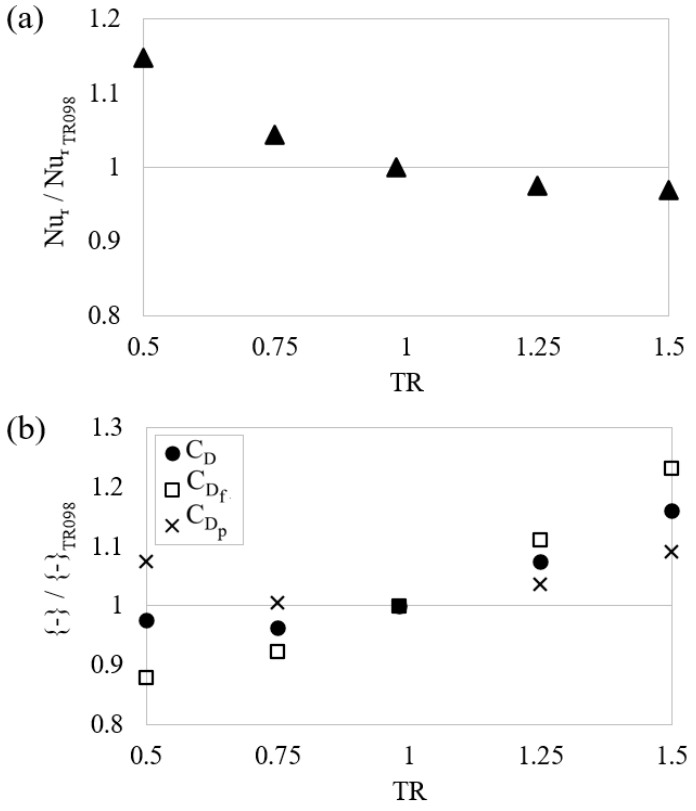


Figure 4.12: *Impact of TR on aerothermal parameters at* Re_r=720

The influence of TR on the drag coefficient is depicted in fig. 4.12b. In contrast

to the Nusselt number, the total drag coefficient C_D increases by ∼15% for the heated wall case. Unlike what is observed for a flat plate boundary layer where the frictional drag coefficient is largely unchanged for different TR values (see table 3.1), for a surface microstructure array, the temperature of the wall has a significant impact on C_{D_f}.

Our attention is drawn to the opposite variations of the friction and pressure drag components at different TRs. As shown in fig. 4.12b, for a cooled wall (TR=0.5), the frictional drag is lower than the pressure drag, but the opposite is observed for a heated wall (TR=1.5). To help interpret the relatively decreased friction drag for a cooled wall, we examine the local friction coefficient contours over the hemisphere surface at TR=0.5 and TR=1.5 as shown in fig. 4.13. The major changes occur strikingly in the local area around the flow separation. The bulk frontal surface area until separation seems to have largely negligible changes, similarly to the flat plate boundary layer, subject to the compensating effects between viscosity and velocity gradient (as discussed in section 3.2). On the other hand, the compensating mechanism stops functioning in the rear part of the microstructure in the proximity of the separation line (blue stripe indicated with 'A' in fig. 4.13a, red stripe indicated with 'B' in fig. 4.13b). For TR=0.5, the earlier separation leads to a lower local velocity gradient in the separated region, while the dynamic viscosity is also lower compared to the quasiadiabatic case, resulting in much lower local shear stress. Inversely, wall heating (TR=1.5) causes a higher local velocity gradient due to postponed separation and higher near-wall dynamic viscosity due to heating, leading to a much higher shear stress than in the reference case. The impact of TR on the friction drag coefficient is smaller for TR=0.5 than it is for TR=1.5

due to the size of the 'A' area, which is smaller than the 'B' area (fig. 4.13).

The relatively increased pressure drag at a cooled wall condition (TR=0.5) depicted in fig. 4.12b can be easily attributed to the enlarged recirculation due to wall cooling (fig. 4.9). A rather contradicting behavior is observed for the heated wall case (TR=1.5), where the pressure drag coefficient is seemingly higher compared to the quasiadiabatic solution. This is likely to be caused by the increased frontal stagnation effect due to the reduced separation of the upstream microstrcuture element (e.g. comparing the frontal streamlines and flow patterns between fig. 4.13a and fig. 4.13b).

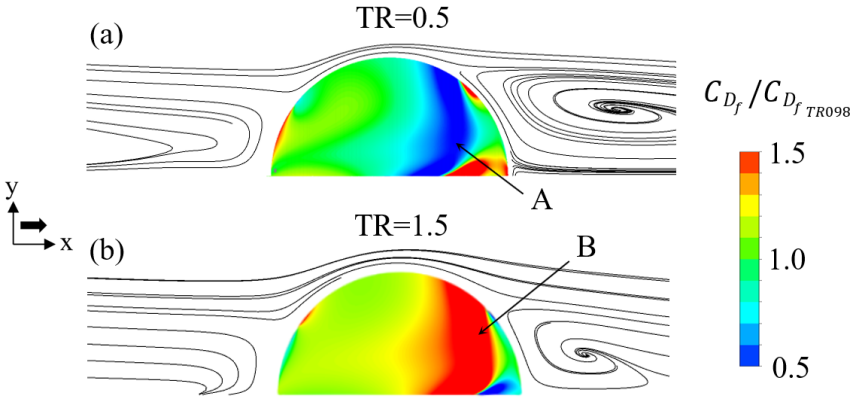


Figure 4.13: *Impact of TR on the local C_{D_f} distribution. The C_{D_f} contour is 3D, and 2D streamlines are plotted on the mid-pitch cut-plane (z=0)*

The interdependence between aerodynamics and heat transfer, for an array of surface microstructures in the laminar regime, translates into a more significant impact on performance parameters compared to a flat plate boundary layer. Next, we will discuss the consequences of the substantial local Reynolds number variation and its impact on turbulent transition for the same array of hemispheric microstructures.

4.4 Transition to turbulent flow

The significant variation of Re_{local} observed in the laminar regime (Re_r=720) as discussed in section 4.3 does beg a question: how would turbulent transition behave under the influence of wall heat transfer considering its impact on Re_{local}? In general, the impact of wall thermal Boundary Condition (BC) on transition seems to lack consistent observations and understanding, as commented on in the Introduction. Furthermore, there seem to be hardly any previous findings for microstructured surfaces in particular.

In this section, we address such a question in three subsections covering the following aspects: i) the transitional behavior under heat transfer influence at a given transitional Re_r; ii) the transition characteristics for different TRs, in terms of the overall aerothermal parameters (C_D, Nu), for a range of Re_r values, in addition to the applicability of the incompressible model in predicting such transtional behavior; and iii) a more unified nondimensional characterization of the transitional regime to account for TR effects.

4.4.1 Transitional flow behavior at a given Re_r

The flow fields at Re_r=4000 for two different TR values are illustrated in fig. 4.14. The quasiadiabatic case shows a laminar flow field as depicted in fig. 4.14a, whereas, the cooled wall case (TR=0.5) is characterized by unsteady separated flow as illustrated in fig. 4.14b. The increased local velocity in the shear layer at TR=0.5 (area indicated with 'B' in fig. 4.8a) makes the flow field more prone to shear layer instabilities. This finding

is in line with the substantially higher local Reynolds number near the microstructures shown for TR=0.5 in fig. 4.7.

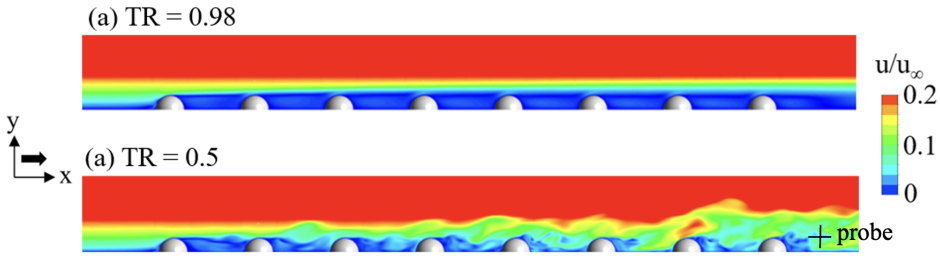


Figure 4.14: *Velocity field at Re_r=4000. a) TR=0.98, b) TR=0.5*

To further assess the cooling-induced unstable flow, we examine the power spectral density in a position where the flow is more developed. The axial velocity spectrum at a point downstream of the last microstructure for the cooled wall case (TR=0.5) at Re_r=4000 is illustrated in fig. 4.15, showing a spectrum similar to a typical turbulent one albeit not being fully developed (the location of the probe is illustrated in fig. 4.14). We therefore observe a clear promotion of turbulent transition for the cooled wall case, which is in line with the substantial increase of the local Reynolds number as established in the previous sections.

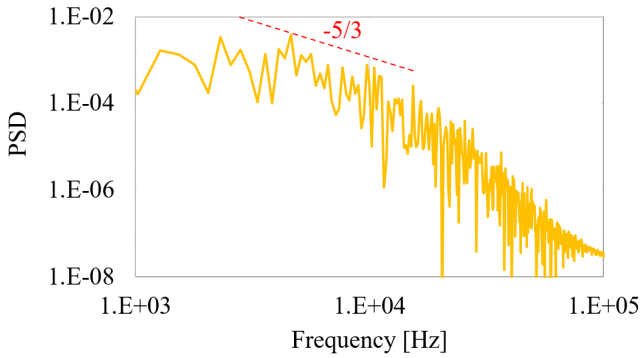


Figure 4.15: *Power spectral density of axial velocity downstream of the last mictrostructure at Re_r = 4000 for TR=0.5*

4.4.2 Transitional regime at different Re_r

We now analyse the flows for various Re_r, ranging from laminar to turbulent flows, at three wall temperatures: TR=0.5 (cooled wall), TR=0.98 (quasi-adiabatic) and TR=1.5 (heated wall). Performance parameters are area-averaged over microstructures number 5, 6, and 7 of the row to better represent a more fully developed flow field by excluding the first four microstructures of the row and the last one.

The drag coefficient is shown for several Reynolds number values (Re_r) in fig. 4.16. In the quasi-adiabatic case (TR=0.98), turbulent transition takes place at Re_r∼5000, whereas for TR=0.5 and TR=1.5, it occurs respectively at Re_r∼2500 and Re_r∼7500. These preliminary results suggest that the critical Reynolds number drops by 50% for TR=0.5, and increases by 50% for TR=1.5, indicating that TR has a substantial impact on transition given the corresponding substantial change in Re_{local}.

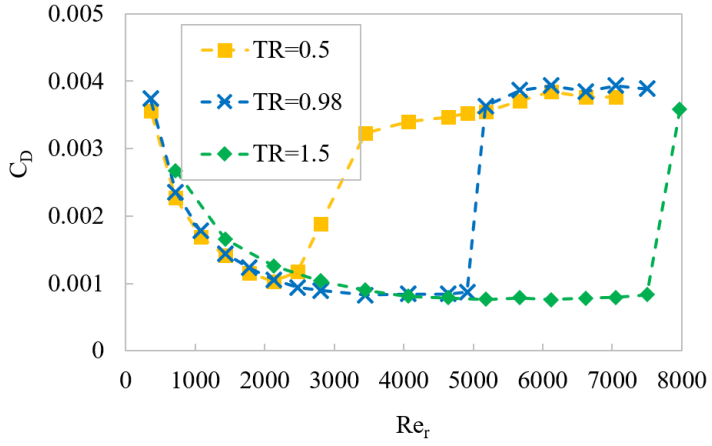


Figure 4.16: *C_D-Re_r chart for three wall temperatures: cooled wall (TR=0.5), quasi-adiabatic (TR=0.98), and TR=1.5 (heated wall)*

Similarly, the Nusselt number with its wall temperature dependency is depicted

in fig. 4.17. For Re_r<2500, the results under all TR conditions are laminar, and $Nu_{r_{TR05}} \sim 1.1 Nu_{r_{TR098}}$. On the other hand, for Re_r>7500, all the wall temperatures tested lead to turbulent flows.

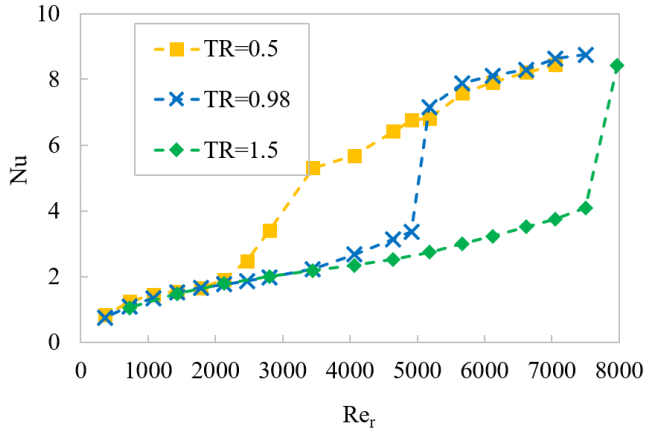


Figure 4.17: *Nu_r-Re_r chart for three wall temperatures: cooled wall (TR=0.5), quasi-adiabatic (TR=0.98), and TR=1.5 (heated wall)*

Another indication of a more fully developed turbulent flow for Re_r>5000 at TR=0.5 and TR=0.98 is provided by the axial velocity spectrum taken at a point downstream of the last microstructure. For both TR values, the standard -5/3 distribution is detected in the inertia scale range of the spectra, as illustrated in fig. 4.18.

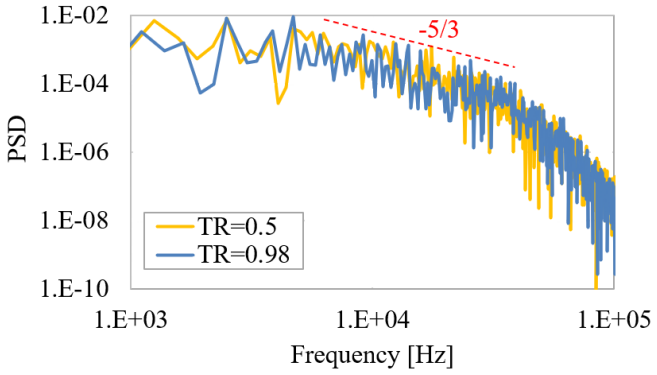


Figure 4.18: *Power spectral density of axial velocity downstream of the last mictrostructure at Re_r = 6200 for TR=0.5, and TR=0.98*

Turbulence intensity is evaluated at the same point used for the velocity spectrum, indicating that TR=0.5 results in a slightly higher turbulence intensity than the reference quasiadiabatic case, as shown in table 4.3.

Table 4.3: *Turbulence intensity value at a point downstream of the microstructures*

TR	I
0.5	0.246
0.98	0.230

To illustrate the effect of TR on the separation regions in the turbulent regime, the time-averaged velocity field at Re_r=6200 is depicted in fig. 4.19. In contrast to the laminar regime, where the cooled wall case (TR=0.5) presents a larger recirculation region (fig. 4.9), for the turbulent flow regime, TR=0.5 shows a delayed separation and a smaller recirculation region. Bearing in mind the earlier transition with the cooled wall, we would expect that the corresponding turbulent flow in this case is more fully developed than that for the quasiadiabatic TR, as indicated by the corresponding turbulence intensities (table 4.3). As such, a stronger turbulent mixing in the near wall region might lead to a delayed separation for the cooled case, as seen in fig. 4.19.

A relevant modelling issue of interest, particularly in the context of predicting the transition under the influence of heat transfer, is the applicability of the incompressible flow model. Incompressible flow assumptions, where the energy equation is linear and the flow field is uncoupled from the thermal field, are often adopted for transition studies. Therefore, a question arises: can the incompressible flow model predict the

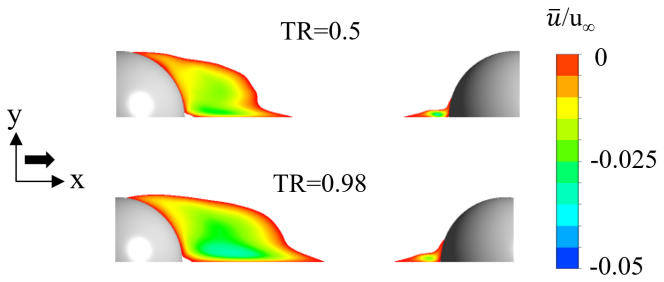


Figure 4.19: *Time-averaged velocity, Re_r=6200. The velocity contour is clipped at $\bar{u}/u_\infty$=0*

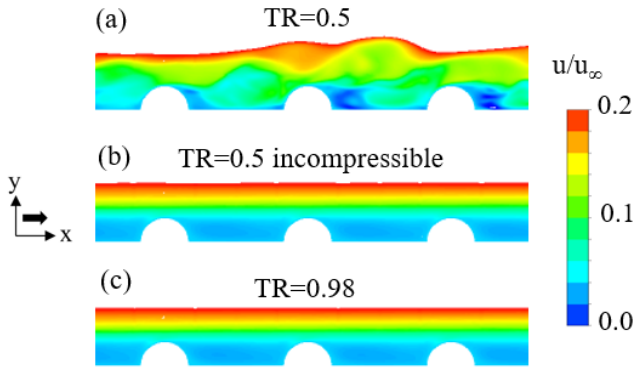


Figure 4.20: *Velocity contours at Re_r=3450. a) Compressible flow at TR=0.5; b) Incompressible flow at TR=0.5; c) Compressible flow at TR=0.98*

transition behavior under the influence of heat transfer? The flow field obtained using the incompressible flow model, which entails constant fluid properties, is compared with the compressible results in fig. 4.20 for the same Reynolds number (Re_r=3450). For incompressible simulations (fig. 4.20b), u_∞ is adjusted to match the prescribed Re_r, and fluid properties are fixed at the condition T=T_{01} so that the energy equation is linear and the flow field is independent of the thermal field. On the other hand, for compressible solutions, fluid properties vary with temperature as discussed in section 4.1 implying the non-linearity of the energy equation and the coupling of flow and thermal fields.

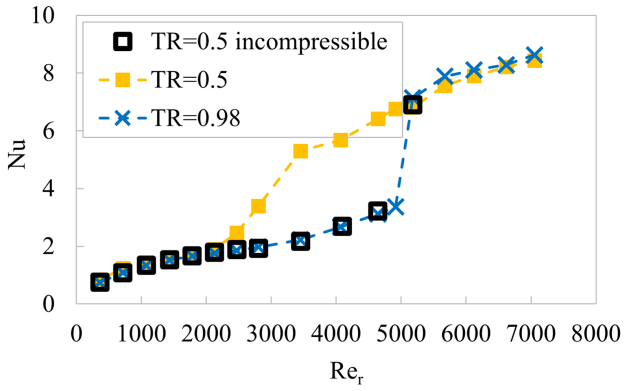


Figure 4.21: *Applicability of the incompressible flow solution to transition under the influence of heat transfer*

In the present study, the incompressible flow model results are shown to be completely unable to capture the TR influence. The Nusselt number variation with Re_r predicted by the incompressible flow at TR=0.5 is almost the same as that predicted by the compressible flow model at TR=0.98, as shown in fig. 4.21. In fact, in an incompressible flow, the velocity field can be obtained by solving only the continuity and momentum equations. The energy equation is effectively redundant as far as the velocity field is concerned, thus the temperature field is passive and has no effect on the velocity field. Those results suggest that the incompressible flow model cannot predict the interplay between aerodynamics and heat transfer, manifested in terms of the influence of TR on the laminar-turbulent transition for the microstructured surface.

4.4.3 Non-dimensional characterization

Conventionally, the key nondimensional aerothermal parameters (C_D,Nu) are considered to be only dependent on Re (for a given geometry configuration). On the other

hand, in the present study, we observe different aerothermal characteristics for different TRs, as shown in figs. 4.16 and 4.17. For more general characterization and efficient applications to different wall temperature conditions, we thus ask, is there a new independent parameter or a nondimensional group so that a unified characteristic relation can be established to automatically take into account the TR effect?

If we consider Mach number effects to be negligible for such low speed flows, the conventional nondimensional groups C_f and Nu only depend on Reynolds number and Prandtl number. For typical aerothermal analyses (viscous flow and convective heat transfer), non-dimensional performance parameters are commonly expressed in a power index form:

$$(C_f, Nu) = C\ Pr^n\ Re^m \tag{4.2}$$

where C, m, n are constants depending on geometry configurations and flow conditions. In the present work, the emphasis is placed on the wall heat transfer effect marked by different temperature ratios (TRs). Therefore, extra attention has been directed to the additional non-dimensional group (TR), which is included as follows:

$$(C_f, Nu) = C\ Pr^n\ Re^m\ TR^k \tag{4.3}$$

For a given fluid, Pr is constant, thus its influence can simply be included in constant C, i.e.:

$$(C_f, Nu) = C\ Re^m\ TR^k \tag{4.4}$$

Equation (4.4) translates into the following relations for C_f and Nu with the corresponding set of constant indices:

$$\begin{aligned} C_f \ TR^{z_{C_f}} &= C_{C_f} \, Re^{m_{C_f}} \\ Nu \ TR^{z_{Nu}} &= C_{Nu} \, Re^{m_{Nu}} \end{aligned} \tag{4.5}$$

Equation (4.5) can also be rewritten in the following general functional relations:

$$\begin{aligned} C_f \ TR^{z_{C_f}} &= f_1(Re) \\ Nu \ TR^{z_{Nu}} &= f_2(Re) \end{aligned} \tag{4.6}$$

The above eqs. (4.5) and (4.6) imply that when seeking a unified Reynolds number correlation for different TRs, we should consider using the groups $C_f \, TR^{z_{C_f}}$ and $Nu \, TR^{z_{Nu}}$. The implementation of the new grouping requires determining the constants z_{C_f} and z_{Nu}. Considering the rather different aerothermal characteristics at different Reynolds, we will have to determine the constants separately for different parts of a transition process.

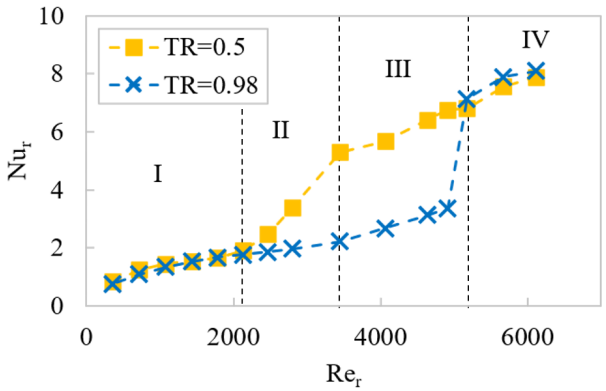


Figure 4.22: *Non-dimensional analysis method to determine* z_{Nu}

Taking the cooled wall case as an example, the characteristics for the whole Re range can be typically divided into four parts: laminar (I), transitional due to cooling (II), transitioned due to cooling (III), and turbulent (IV), as shown in fig. 4.22. The corresponding constants can be fixed by given solutions for each part respectively. Their value can be obtained from eq. (4.5) for each Re_r (e.g. $z_{Nu}=\frac{ln\frac{Nu_{0.98}}{Nu_{0.5}}}{ln\frac{0.5}{0.98}}$) and then it is averaged over the points of each part (I-IV). The results for Nu and C_D with the new nondimensional grouping are shown in fig. 4.23. We can see that the three curves for three TRs are now collapsed into one for both C_D and Nu, as intended.

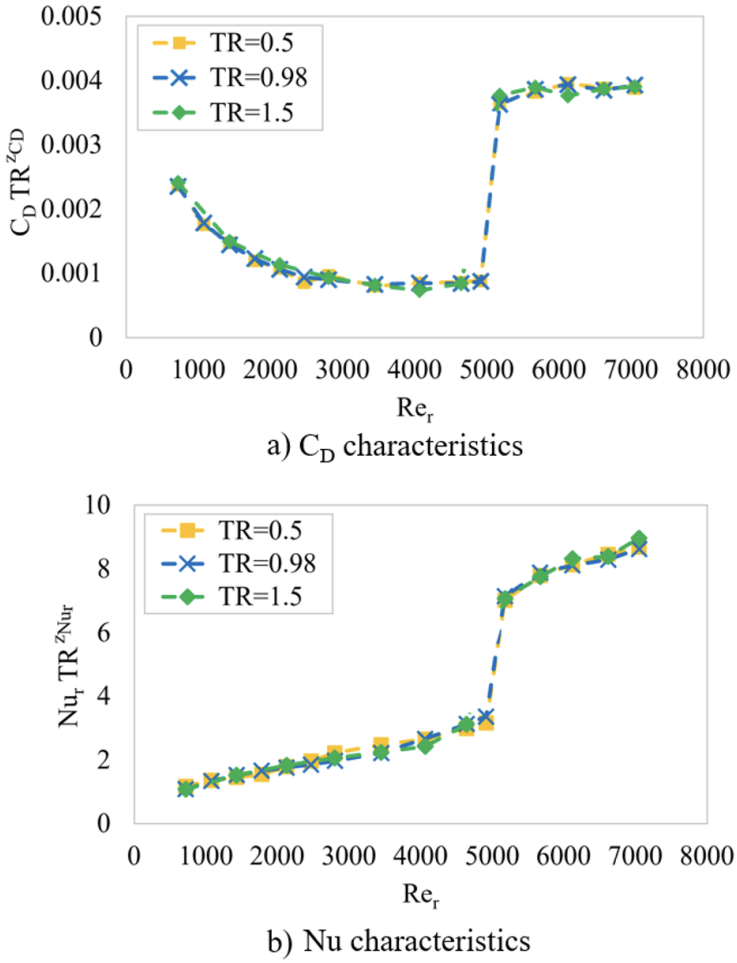


Figure 4.23: *Regrouped non-dimensional characteristics*

4.5 Remarks

Similar to observations made for a flat plate boundary layer, a cooled wall also leads to a very significant increase in the local Reynolds number within the boundary layer, even in the presence of regular roughness. In fact, for surface microstructures, the local velocity distributions around flow separations and in the recirculation zones cause distinctive variations in the local Reynolds number. These are directly attributable to changes in flow separation, with notable associated changes in drag and heat transfer.

More remarkably, in line with the substantial increase in the local Reynolds number for the microstructures under wall cooling, a much earlier transition to a turbulent flow is predicted by the scale-resolving LES simulations. The corresponding bulk-flow critical Reynolds number, for the cooled wall case, is reduced by about 50%, and increased by about 50% for the heated wall. It is also demonstrated by a comparative test that incompressible flow LES solutions under the cooling condition (TR=0.5) produce almost the same results as compressible flow solutions under the near-adiabatic condition (TR∼1). Thus, an incompressible flow model is deemed to be unsuitable for transition predictions if there are significant heat transfer effects as in the present cases.

Further considerations are given to a more unified characterization for scaling wall heat transfer effects in practical applications. A regrouping of the nondimensional parameters (C_D, Nu) with TR is proposed. With the new regrouping, the nondimensional aerothermal performance results with different TRs can now be collapsed into a single curve with regard to Reynolds number, which, once established, may be simply used to

get the aerothermal performance results at different TRs at no extra cost.

Chapter 5

Surface Microstructure Array Under Pressure Gradient

The computational configurations employed in the preceding chapters, while valuable for revealing fundamental principles governing aerodynamics and heat transfer interactions, are rather simplified for academic purposes and do not fully capture the complexity of real-world applications. This section is aimed to assess the behavior of surface microstructures under more realistic conditions.

In this chapter, Msflows, a novel multiscale block spectral approach developed by He [106] is employed to solve the flow field around an array of surface microstructures, larger than that described in chapter 4, under the suction side pressure gradient of a high-lift, low-pressure turbine airfoil. In particular, to validate the computational method and correlate it with empirical findings, the Msflows simulation results are compared with experimental data from Jeong et al. [7].

The motivation behind using Msflows instead of ANSYS FLUENT in subsequent chap-

ters is its multiscale capability, which allows for the analysis of a large number of surface microstructures that would be impractical in ANSYS FLUENT due to the prohibitive computational costs associated with a direct solution of such a two-scale problem. Nevertheless, the focus of this thesis is not to test the multiscale capabilities of the solver, as these have already been well-documented [106,107], but rather to utilize it for studying the coupling between aerodynamics and heat transfer in the context of a surface microstructure pattern. It is also important to note that the Msflows meshing process for a large number of surface microstructures, along with the generation of embedded blocks around them, is very convenient, offering a simpler meshing procedure than that of ANSYS FLUENT.

To start, an introduction to the solver and several preliminary validation cases are presented. Following that, a smooth wall boundary layer flow under the pressure gradient of interest is simulated, and these results are compared against the corresponding experiments by Jeong et al. [7] for a more comprehensive validation of the computational approach. Subsequently, an array of surface microstructures under the same pressure gradient is studied, and its behavior is then compared with that of the rough surfaces examined in the experiments, which are characterized by random roughness.

To summarise, this chapter aims to address the following research questions: do the Msflows results for the smooth wall under a pressure gradient match the experimental study by Jeong et al. [7]? Does regular roughness exposed to a pressure gradient show a similar impact on the flow field to random roughness? To what extent do the two types of roughness have comparable behavior?

5.1 Solver description and validation

Msflows is a Fortran-based code that has been developed since 1995 by He [110–112] to analyze three-dimensional, steady or unsteady flows around immersed objects, including conjugate heat transfer.

The primary governing equations for Msflows are the three-dimensional unsteady Navier-Stokes equations. These equations are applied to govern compressible flow within a stationary cylindrical coordinate system, while a moving mesh is utilized to handle rotor passages.

Regarding meshing, the code employs a multi-block approach with dual mesh capability, enabling the embedding of local fine mesh blocks within the computational domain.

The code offers multiple options for turbulence closure, allowing users to select the most appropriate model for their specific application. This includes the Denton wall distance limiter-based mixing-length model, the Spalart-Allmaras one-equation model [113], and the Menter $k-\omega$ SST two-equation model [114]. Additionally, the software provides the option to implement scale-resolving Large Eddy Simulations (LES), offering both Smagorinsky subgrid scale [115] and Implicit Large Eddy Simulations (ILES) models.

Spatial discretization of the governing equations is achieved using a second-order accurate finite-volume scheme. The variables are stored in cell centers, and central discretization is used for the viscous dissipation terms. The code utilizes the upwind

scheme (AUSM) to discretize the convective terms. The baseline spatial scheme is second-order, with the availability of a third-order alternative.

Time integration of the discretized equations is performed using a four-stage Runge-Kutta scheme, and for unsteady flows, dual time stepping with sub-iterations is adopted as described by Jameson [116]. Time integration is enhanced by implementing multigrid techniques.

Boundary treatment encompasses various aspects, including interior interfaces that involve interpolation for flow variables at dummy points, solid-surface boundary options for momentum and energy, and inlet/exit boundaries.

Unsteady disturbances in the simulation may originate from multiple sources, such as relative motions of objects (e.g., turbomachinery rotor-stator interactions), prescribed wall surface oscillations, inlet/exit distortions, and even self-excitation due to flow instability and turbulence fluctuations.

This chapter introduces Msflows, including a preliminary validation through a comparison with the commercial code ANSYS FLUENT. It aims to present the capabilities of Msflows in computational fluid dynamics and heat transfer simulations, specifically regarding the aerothermal analysis of surface microstructures.

5.1.1 Preliminary validation

This section is dedicated to evaluating the reliability and accuracy of Msflows in analyzing the interaction between heat transfer and aerodynamics. It includes a comparative analysis of Msflows against ANSYS FLUENT, aiming to determine the capacity of the

model to accurately represent the interaction between heat transfer and aerodynamic behaviors.

An initial assessment was performed on a standard flat-plate laminar boundary layer. The results obtained from Msflows reveal notable variations in the flow field, depending on different values of the temperature ratio TR. More specifically, an increase in wall temperature (TR=1.5) is found to significantly augment the thickness of the boundary layer, as visualized in fig. 5.1. Conversely, wall cooling exhibits a reverse trend. These outcomes substantiate and corroborate the previously discussed results obtained with ANSYS FLUENT, as outlined in section 3.2.2, matching those results within a 1% difference.

Although the examination of the flat plate laminar boundary layer has provided valuable insight into the influence of heat transfer on the flow field, the principal focus of this project is the systematic study of surface microstructures. In particular, as previously described in section 4.3, wall cooling (TR=0.5) is observed to lead to an increase in the density near the wall, resulting in increased local fluid inertia and delayed reattachment. In contrast, in the case of a heated wall (TR=1.5), a reduction in near-wall density corresponds to an earlier flow reattachment. This results in the augmentation of the recirculation zone for wall cooling and its reduction for wall heating, as previously depicted in fig. 4.9.

For the purpose of validating Msflows against ANSYS FLUENT, a rectangular 2D surface microstructure was introduced into a laminar flat-plate boundary layer flow at Re=10000 (see fig. 5.2). At the indicated location, the boundary layer thickness is 15

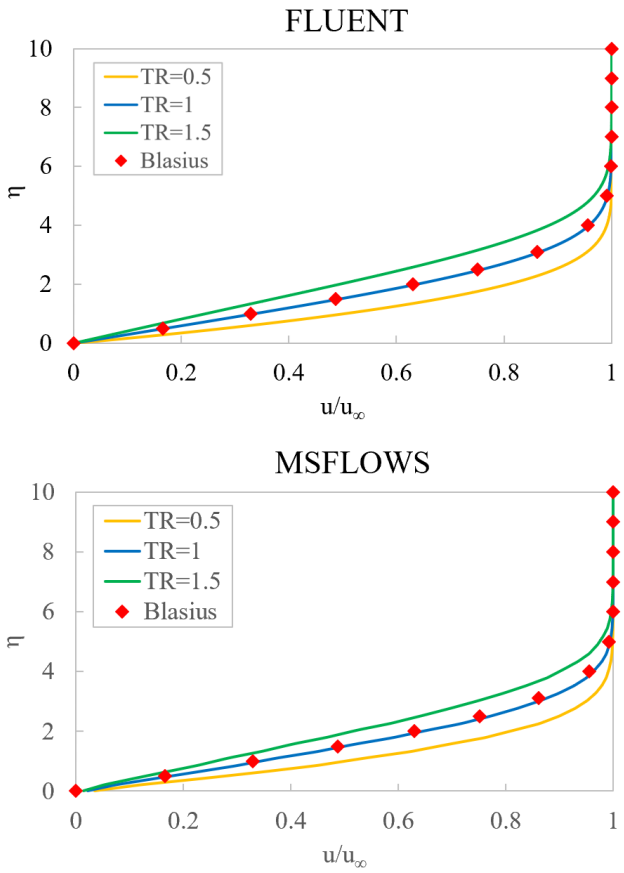


Figure 5.1: *Impact of TR on the velocity profile for flat-plate boundary layer. Comparison of Msflows present results with ANSYS* FLUENT *show matching within a 1% difference*

times greater than the height of the surface microstructure. The Msflows results indicate substantial agreement with those of the commercial code, as depicted in fig. 5.3. This verification underscores the consistent observation in laminar flows that an increased size of the separation bubble is due to an increase in local fluid inertia resulting from wall cooling, and conversely, the opposite effect occurs with wall heating.

To evaluate the accuracy of Msflows in simulating 3D flows characterized by non-negligible wall heat transfer with TR significantly deviating from 1, a simulation was conducted for a 3D laminar flow over a rectangular surface microstructure. The results

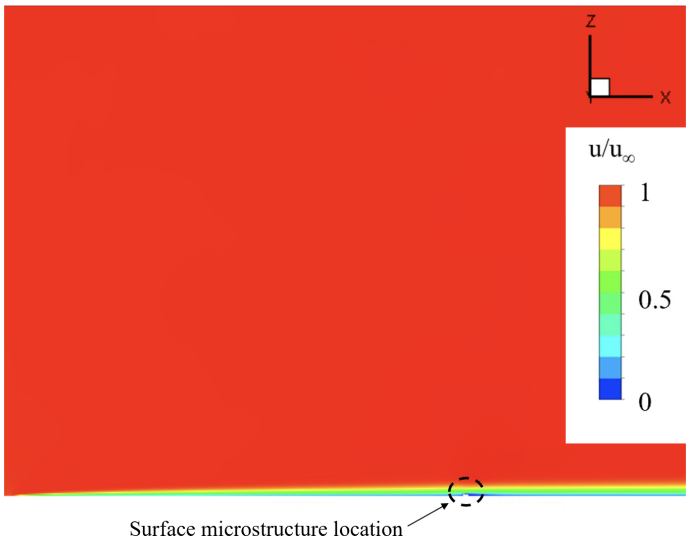


Figure 5.2: *2D surface microstructure in a flat-plate laminar boundary layer flow field*

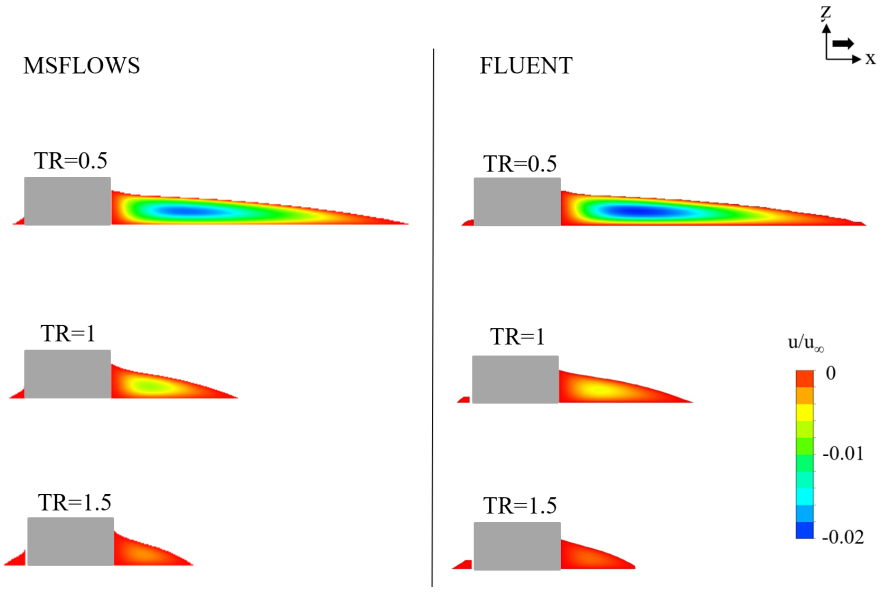


Figure 5.3: *Msflows resuslts validation against ANSYS* FLUENT *for a 2D surface microstructure located in a flat-plate laminar boundary layer*

obtained were then objectively compared with simulations performed using ANSYS FLUENT.

The computational setup used in this case is very similar to the one described in

fig. 4.1, with the main difference being for simplicity the presence of a single surface microstructure instead of a row of 6 as illustrated in fig. 5.4. An inlet boundary layer profile is used the same way as described in section 4.1 to secure a boundary layer thickness 10 times larger than the microstructure height so that the boundary layer development is not disrupted by the presence of the microstructure. Similarly, the other boundary conditions are based on what is described in section 4.1.

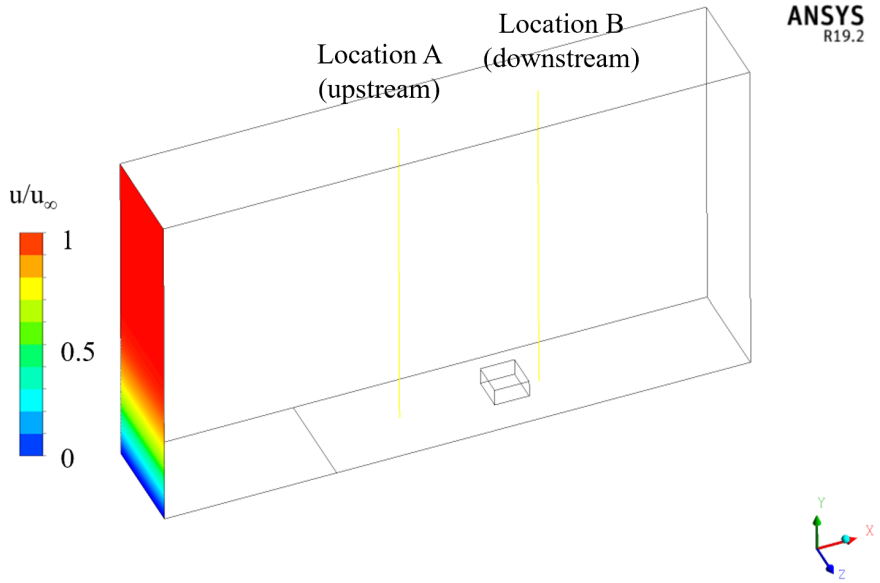


Figure 5.4: *3D surface microstructure flow domain used for the validation of Msflows*

The velocity profiles upstream and downstream of the surface microstructure were quantitatively compared with an ANSYS FLUENT case, utilizing the same computational settings. The comparison was conducted at specific locations, A and B, as indicated in fig. 5.4. The results obtained from Msflows exhibited consistent agreement with the Blasius solution upstream of the microstructure, as well as with ANSYS FLUENT in the downstream recirculation area (location B), as shown in fig. 5.5. Moreover, although not

apparent in fig. 5.5 because the image is zoomed out to encompass the entire velocity profile, the same trend regarding the impact of TR on the the size of the recirculation region illustrated in fig. 5.3, was identified in this 3D simulation.

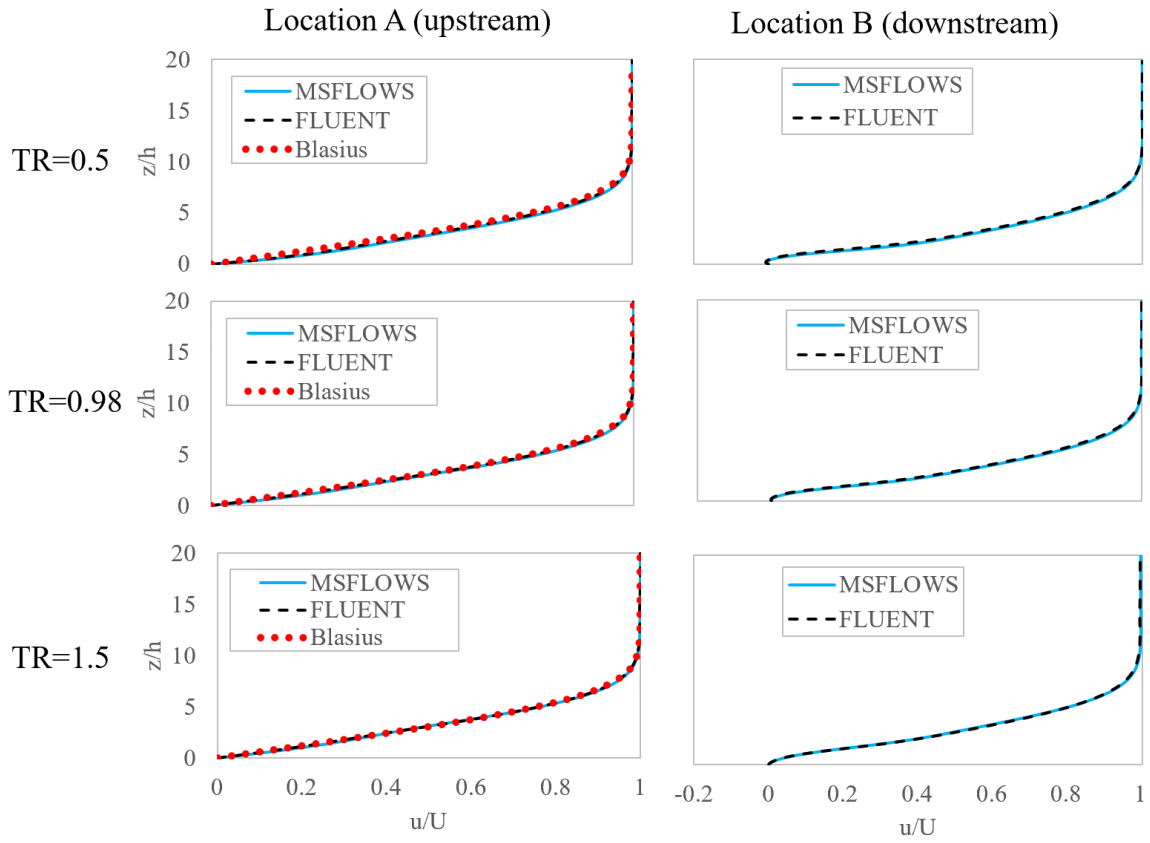


Figure 5.5: *Velocity profiles upstream and downstream of a 3D surface microstructure to validate Msflows present results against ANSYS* FLUENT

In summary, it can be deduced that for all laminar cases considered, Msflows exhibited a highly satisfactory agreement with ANSYS FLUENT in assessing the influence of temperature ratio on the flow field. This confirmation is consistent with the key findings discussed in chapters 3 and 4. Given the successful validation of Msflows outlined in this section, the following section introduces a more realistic computational setup. The objective is to leverage Msflows for the study of interactions between aerodynamics and

heat transfer in the context of surface microstructures under the suction side pressure gradient of a high-lift low-pressure turbine airfoil.

5.2 Computational method and set-up

The primary objective of this chapter is to use Msflows for a comprehensive examination of the behavior of surface microstructures in scenarios more representative of real-world conditions than those outlined in chapter 4. This includes introducing a pressure gradient and studying a larger array of microstructures. The results obtained from Msflows will be compared with the experimental data presented by Jeong et al. [7], who specifically examined the influence of surface roughness under the suction side pressure gradient of a high-lift, low-pressure turbine airfoil. Therefore, the computational setup used for this comparison will be detailed in this section.

The validation process will begin with a comparison against the smooth wall case described in the experimental data by Jeong et al. [7]. Subsequently, the behavior of an array of regular roughness simulated with Msflows will be qualitatively compared with the experimental results obtained by Jeong et al. [7] for random roughness.

Jeong et al. [7] conducted smooth wall boundary layer measurements in a low-speed, open-type wind tunnel at Seoul National University. The flow was generated by a 45 kW blower and the flow domain is depicted in fig. 5.6a. The flow speed was adjusted to test the two Reynolds numbers of interest: the so-called cruise condition (Re_c=120000), and the take-off (Re_c=520000). The test section featured a 1300mm long aluminum

flat plate with elliptic leading and trailing edges ($50mm$ major axis, $10mm$ minor axis) within a $2400mm$ (chordwise) $\times$ $400mm$ (spanwise) $\times$ $430mm$ (pitchwise) space. Contoured walls were installed to replicate the suction side pressure gradient of a T106A high-lift low-pressure turbine airfoil, maintaining zero incidence. The chord length, equivalent to the turbine suction surface length, was $546mm$. A wire mesh turbulence grid, located 1.1 chord lengths upstream of the leading edge, introduced static free-stream turbulence. The measured turbulence intensity and the integral length scale at the leading edge were 3.2% and $6.5mm$, respectively. Three surface roughness levels (R_a=$0.356\mu m$, $24.16\mu m$, and $40.63\mu m$) were tested, using a smooth machined aluminum plate for R_a=$0.356\mu m$, and sandpaper attached to the aluminum plate for the other cases, respectively, excluding the leading and trailing edges. An additional sandpaper patch of non-specified roughness level was affixed to the upper wall near the suction peak. This was solely to prevent or reduce flow separation at the lower Reynolds number (Re_c=120000), which could otherwise lead to a significant coupling between the behavior of the top and bottom walls.

In an effort to optimize computational efficiency in Msflow simulations, the computational domain has been strategically restricted to encompass only the region employed in the experiments that is essential for examining the impact of surface roughness on the flow field. This targeted computational domain is depicted in fig. 5.6b for visual reference. The computational domain, as depicted, includes the same contoured wall as in the experiments. However, it focuses only on the section of the flow domain above the flat plate. Additionally, the areas preceding the flat plate's leading edge and beyond

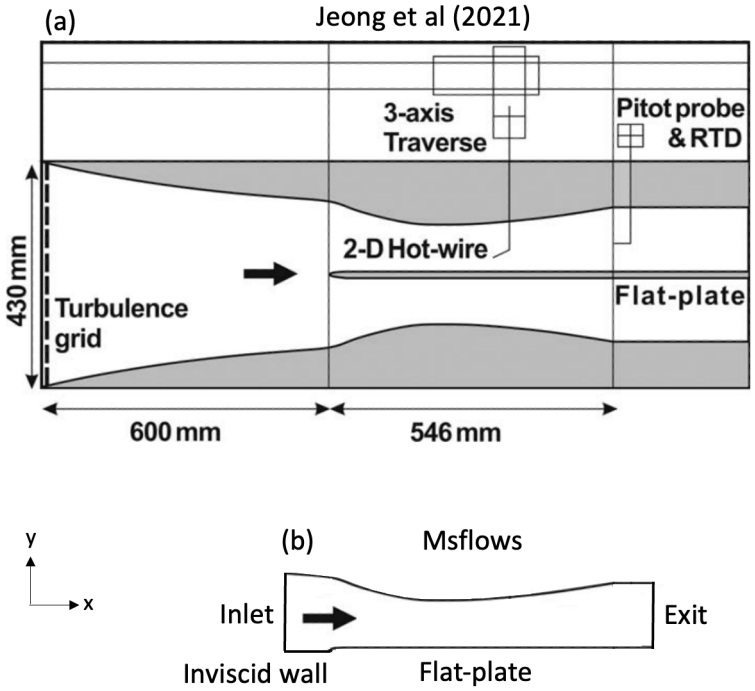


Figure 5.6: *a) Experimental domain by Jeong et al. [7]; b) Msflows present simulation domain*

the Pitot probe's location are truncated.

For direct comparison and validation of the adiabatic smooth wall simulation results with the experiments by Jeong et al. [7], the relevant nondimensional groups Re_c and Pr, calculated in the experiments at exit with a Pitot probe as shown in fig. 5.6b, have been matched, and all boundary conditions are set to replicate a flow field as closely as possible to the experimental conditions. Specifically, the total pressure at the inlet and static pressure at the exit, along with the inlet Reynolds number and the Prandtl number, are adjusted to ensure that the Reynolds number of interest (Re_c) in the simulations corresponds to the Re_c in Jeong et al.'s experiments [7]. Additionally, an inviscid wall is adopted upstream of the flat-plate leading edge, while all other walls,

except the spanwise sidewalls which are also inviscid, are set to no-slip conditions.

As mentioned above, this study aims to analyze an array of surface microstructures under a pressure gradient. Thus, to directly compare the simulation results with the experimental data, the R_a/C value of the regular roughness used in the simulations matches that in the R_a=40.63μm case by Jeong et al. [7]. In particular, the surface microstructure array used for Msflows simulations consists of 3 rows of 20 surface microstructures each: 3 microstructures spanwise x 20 microstructures streamwise, as described in fig. 5.7. Additionally, following the approach used in the experiments by Jeong et al. [7], a surface roughness pattern was applied to the top wall. This was done to reduce or suppress flow separation on the contoured wall, which could otherwise lead to significant coupling between the behavior of the top and bottom walls.

It should be noted that there are still some differences between the computational and experimental setups. For example, the surface roughness employed by Jeong et al. [7] is randomly distributed, while the simulated roughness is regular. Furthermore, there are differences in the starting points of the surface roughness elements: Jeong et al. [7] applied sandpaper sheets to the flat plate beginning right after the leading edge, whereas the regular roughness elements in the simulation commence at the streamwise location x/C=0.55.

The decision to have surface microstructures away from the leading edge in the computational domain is grounded in the need to prevent disruption of boundary layer development. The selected location where the microstructure pattern begins (x/C=0.55) ensures that the boundary layer thickness is 10 times larger than the microstructure

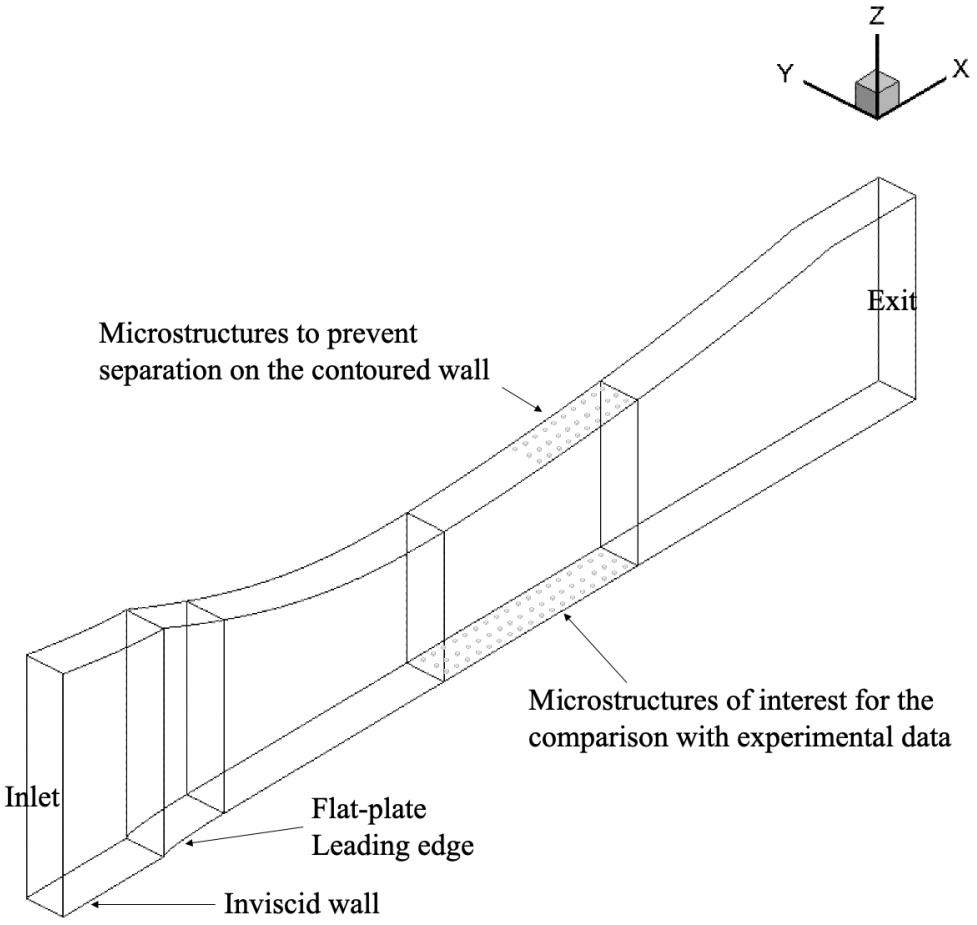


Figure 5.7: *Rough wall Msflows simulation domain*

height. It is important to note that the size of the surface microstructures defines the mesh size, and finding an optimal compromise between having small microstructures to not disrupt the boundary layer and having large microstructures to reduce the mesh size is crucial for achieving a computationally manageable resolution. In this context, rectangular elements used in the Msflows simulations match R_a/C of the experiments and are relatively large in size (h=500μm in height, h/C=0.0003) to ensure a manageable mesh (see fig. 5.8). Hence, given their size, the surface microstructure array used in the simulations has to begin at the streamwise location x/C=0.55 to prevent the

disruption of the boundary layer.

The choice of a rectangular shape, which cannot be directly compared with the hemispherical microstructures used in ANSYS FLUENT simulations in chapter 4, arises from limitations in the Msflows meshing process, which currently does not support the generation of hemispherical elements. The separation mechanism of rectangular and hemispherical microstructures is certainly different. Unlike spherical elements, the separation point in rectangular microstructures is largely predetermined. Nevertheless, the fundamental findings related to the variation in viscosity and density, due to heat transfer, influencing the local Reynolds number values in the boundary layer, are independent of the shape of the microstructure (see fig. 4.8 b-c). Similarly, the argument that variations in local fluid inertia due to heat transfer can affect the size of the separation region, as discussed in fig. 4.9, holds for rectangular microstructures as will be discussed in the following chapter.

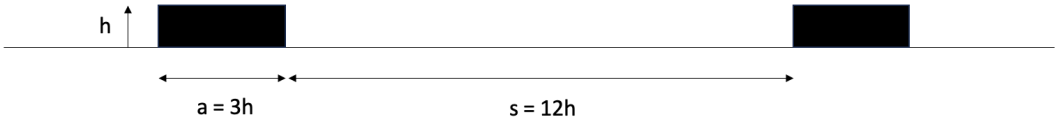


Figure 5.8: *Surface microstructure pattern parametrization*

The primary aim of this chapter is to compare our findings with the experimental study conducted by Jeong et al. [7]. Therefore, the following paragraphs will focus on the differences between the experimental setup used by Jeong et al. [7] and the current analysis conducted using Msflows.

Aside from the variation in the nature of the surface roughness pattern (random

for the experiment vs. regular for the Msflows simulations) and its starting location, in the simulations, no fixed inlet turbulence is imposed, whereas in the experiments the measured turbulent intensity at the flat-plate leading edge is 3.2%, and the span length is set to 10% of the chord to reduce computational costs. Furthermore, in the experiments, a sandpaper patch is affixed to the contoured wall to reduce/prevent flow separation at low Reynolds number (Re=120000) even if no evidence of a completely suppressed contoured-wall separation is provided, whereas in the simulations, surface microstructures are employed for the same purpose on the contoured wall. Surface microstructures are not used on the contoured wall for high Reynolds number (Re=520000) simulations, as the flow does not separate in those cases. Nevertheless, despite such differences, which arise from the use of different types of roughness (regular vs. random) and computational cost constraints, the two setups are still highly comparable and can enable the validation of Msflows against experimental data.

The analysis described in the following sections is based on LES (Large Eddy Simulation) results. The LES method is adopted without an explicit subgrid model, effectively making it an implicit LES. This approach is preferred to capture a transition process without the subgrid model interfering with the laminar flow part, as discussed in [109].

The base mesh used in Msflows simulations has been generated with ANSYS ICEM, a commercial mesh generator. Msflows works with multiblock structured meshes and has the capability of embedding it with local fine mesh blocks. Such capability has been used in the rough-wall simulations to increase the mesh resolution around the surface microstructure and enable to resolve the element-to-element interactions.

The base mesh employed in rough wall cases consists of 2.5 million mesh elements and maintains a $y_+<2$ within the area of interest for experimental comparisons. To improve resolution near the surface microstructures, each mesh cell in the base mesh has been subdivided into three, as detailed in fig. 5.9. However, this refinement has been selectively applied only to the central row of surface microstructures in order to reduce the overall computational resources required for the study. Moreover, for smooth wall cases where no surface microstructures are present on the flat plate, the base mesh without embedded blocks is used.

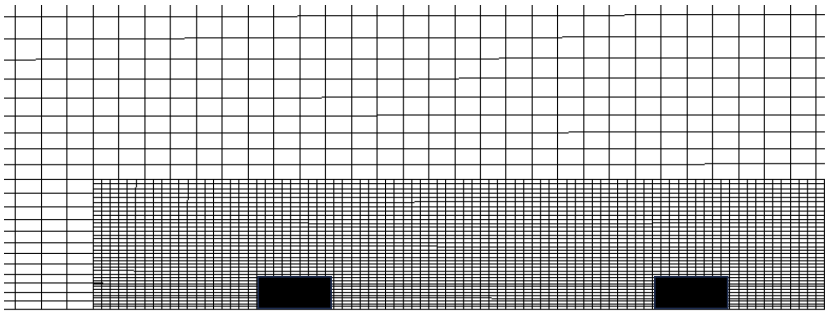


Figure 5.9: *Embedded mesh around the surface microstructures*

5.3 Smooth Wall Validation

In this section, the objective is to conduct a comparison between the smooth wall results generated by Msflows simulations (referred to as "Present" hereafter) and the experimental data presented in the study by Jeong et al. [7]. In particular, the validation will focus on two Reynolds number values of interest: Re_c=120000 and Re_c=520000.

As illustrated by Jeong et al. [7], at Re_c=120000, the flow field separates due to the adverse pressure gradient imposed by the contoured wall on the bottom surface

boundary layer. The present results confirm this behavior, showing good agreement with the experimental data as illustraded in fig. 5.10, which depicts on a mid-span cut plane the time-averaged flow field from the suction peak to the exit of the computational domain. Nevertheless, it should be noted that in the simulations, the reattachment point of the separation region is shifted downstream by approximately 7% of the chord length, and the onset of separation also occurs slightly further downstream compared to the experiments. This minor discrepancy could potentially be caused by the differences between the computational setup and the experimental rig discussed in section 5.2.

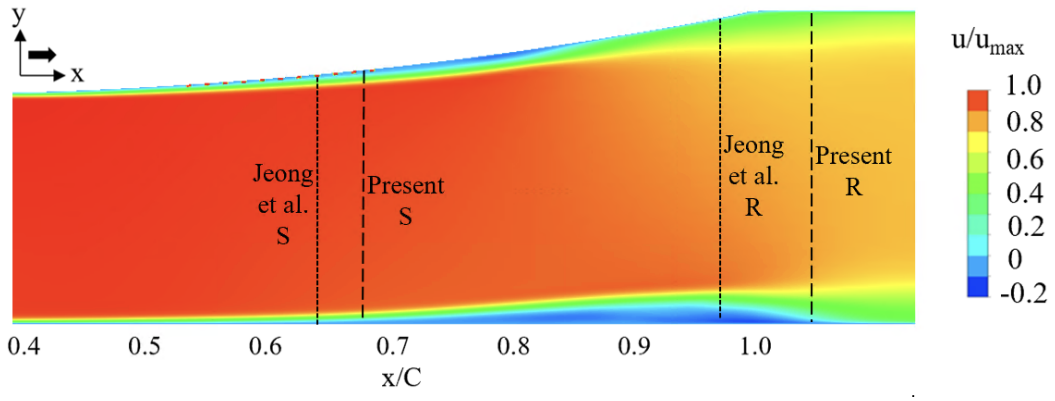


Figure 5.10: *Time-averaged flow field on a mid-span cut plane at* Re_C=120000 *in the smooth bottom surface case from the present Msflows simulations. Locations of separation onset 'S' and reattachment 'R' are also indicated on the contour plot for comparison with Jeong et al. [7]*

Figure 5.11 displays the static pressure coefficient (Cp) measured for the smooth surface at Re_c=120000, plotted against the normalized chord length. This chart shows that Msflows (Present) and ANSYS FLUENT produce consistent results that align with the experimental data by Jeong et al. [7].

The time-averaged flow field, acquired through Msflows simulations, is subjected

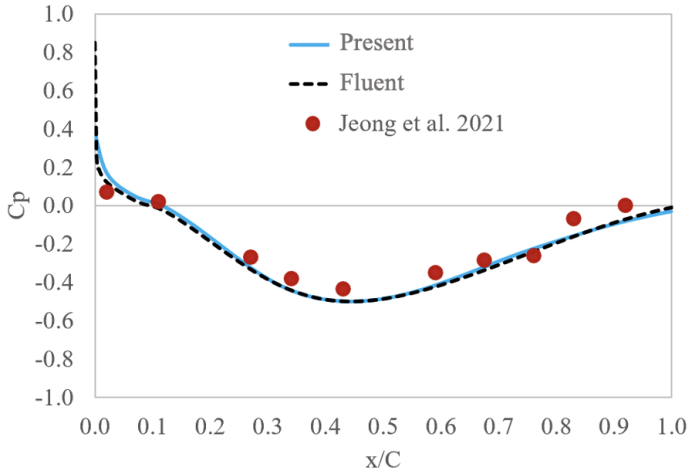


Figure 5.11: *Comparison with experimental data by Jeong et al. [7]: static pressure coefficient plotted versus normalized streamwise location for the smooth surface at* Re_c=120000

to a quantitative comparison with the experimental data presented by Jeong et al. [7]. As depicted in Figure 5.12, the results obtained from Msflows (Present) exhibit a substantial degree of agreement with the experimental findings, although the location of the separation bubble is shifted downstream, as are the velocity profiles. In Figure 5.12, the results of Jeong et al. [7] are compared with the present velocity profiles, which are placed approximately 7% further downstream to account for the downstream shift of the separation bubble, as illustrated in Figure 5.10, and obtain a more meaningful comparison. Although some minor disparities are observed, it is important to note that the experiments themselves are inherently susceptible to a certain level of uncertainty. Specifically, accurately assessing the flow velocity in close proximity to the wall with a probe is a challenging task, which accounts for the deviation from a zero velocity value at the wall in the experimental velocity profiles.

The validation of the Msflows approach is further enhanced by comparing Reynolds

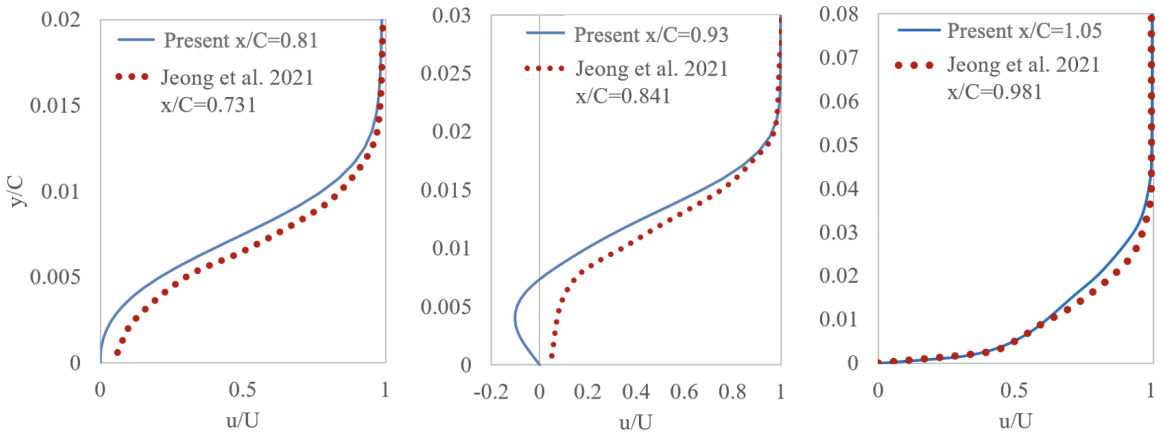


Figure 5.12: *Comparison with experimental data by Jeong et al. [7]: time-averaged velocity profiles at* Re_c=120000 *for the smooth surface case*

shear stresses as shown in fig. 5.13, although aligning the simulations with experimental data in this aspect is notably more difficult than matching the time-averaged velocity field. The primary challenge lies in the complexity of accurately simulating the specific transition mechanism observed in the experiments. For example, at x/C=0.731, the simulations depict a completely laminar flow with zero Reynolds shear stress profiles, while in the experiments, as shown in fig. 5.13, nonzero Reynolds shear stress profiles are detected at x/C=0.731. This relatively minor disparity between experiments and simulations may be attributed to differences in boundary conditions, as discussed in section 5.2. In fact, unlike in the experiments, the inlet turbulence is set to zero in the simulations, a factor that could influence the transition mechanism.

Furthermore, as elaborated on in this section, the reattachment point of the separation bubble on the bottom wall exhibits a downstream shift in the simulations. This shift accounts for the observed similarity between the experimental Reynolds shear stress profile at x/C=0.841 and the simulation profile at x/C=0.9 (approximately 6%

of the chord length further downstream) as illustrated in fig. 5.13.

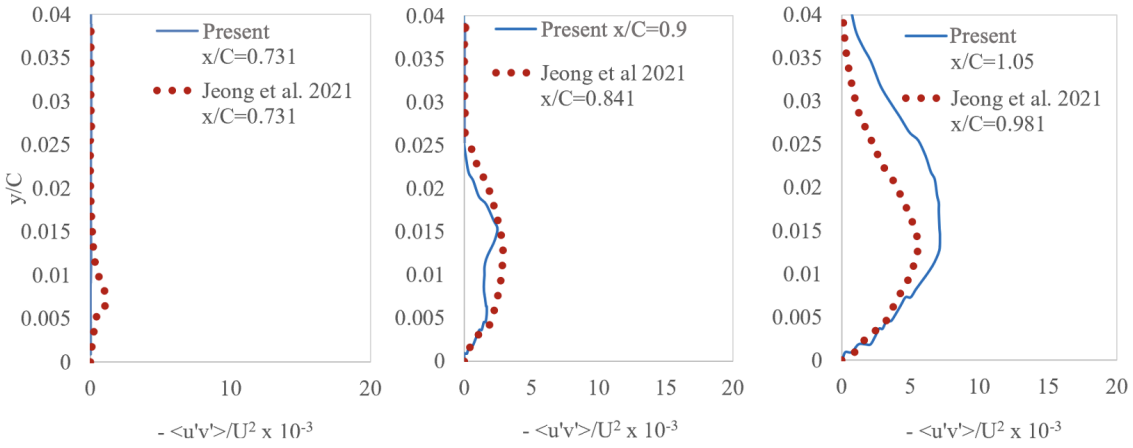


Figure 5.13: *Comparison with experimental data by Jeong et al. [7]: Reynolds shear stress profiles at* Re_c=120000 *for the smooth surface case*

Unlike what was discussed for the low Reynolds number case (Re=120000), where a separation bubble occurs on the bottom wall due to the adverse pressure gradient generated by the contoured wall, at Re=520000, the boundary layer transitions from laminar to turbulent without separation. In agreement with the experimental findings of Jeong et al. [7], the higher turbulent diffusion resulting from the increased Reynolds number leads to a thinner boundary layer, as illustrated in fig. 5.14. This thinner boundary layer is less prone to separation.

The time-averaged flow field obtained from Msflows simulations is quantitatively compared with the experimental data presented by Jeong et al. [7]. As illustrated in fig. 5.15, the present results from Msflows simulations demonstrate a substantial degree of agreement with the experimental findings, indicating a strong correspondence between the two datasets and confirming the downstream flow field shift of roughly 7-8% discussed for the Re=120000 case.

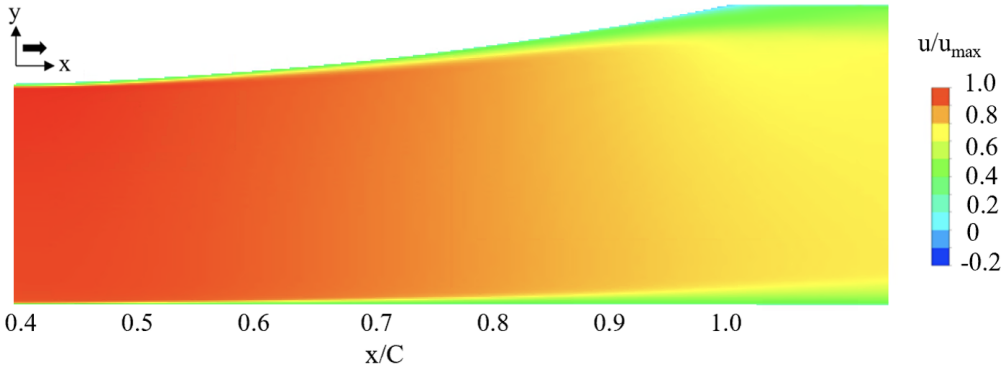


Figure 5.14: *Time-averaged flow field on a mid-span cut plane at Re*=520000 *for the smooth surface case from the present Msflows simulations*

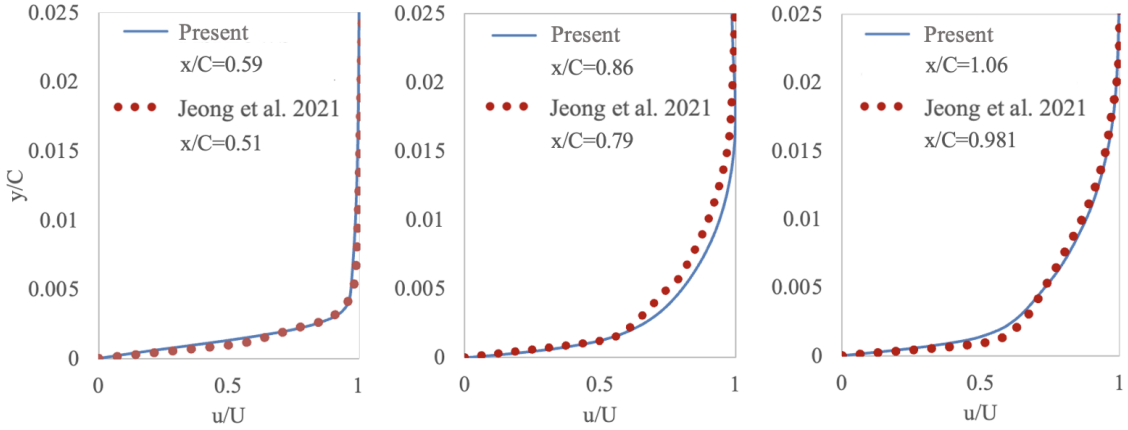


Figure 5.15: *Comparison with experimental data by Jeong et al. [7]: time-averaged velocity profiles at* Re_c=520000 *for the smooth surface case*

Similarly to the study conducted at low Reynolds number ($Re = 120000$), the shear Reynolds stresses derived from high Reynolds number simulations are compared with the experimental data provided by Jeong et al. [7] in fig. 5.16. It is important to note that achieving a precise quantitative comparison between experiments and simulations is hindered by differences in the setups.

In contrast to Jeong et al.'s work [7], the simulations do not introduce a fixed inlet turbulence, and the span length in the simulations is set at 10% of the chord to

optimize computational efficiency, compared to 70% in the experiments. Furthermore, the experimental setup involves the use of a sandpaper patch on the contoured wall for both Reynolds numbers of interest, aimed at preventing flow separation. In contrast, our simulations employ surface microstructures on the contoured wall exclusively at Re=120000, and no surface microstructures are used on the contoured wall in the simulations at Re=520000, because flow separation does not occur at high Reynolds numbers and the presence of microstructures could disrupt the very thin boundary layer.

Nevertheless, despite these differences between the experimental and computational setups, the qualitative agreement between simulations and experiments, as shown in fig. 5.16, suggests a comparable development of the boundary layer.

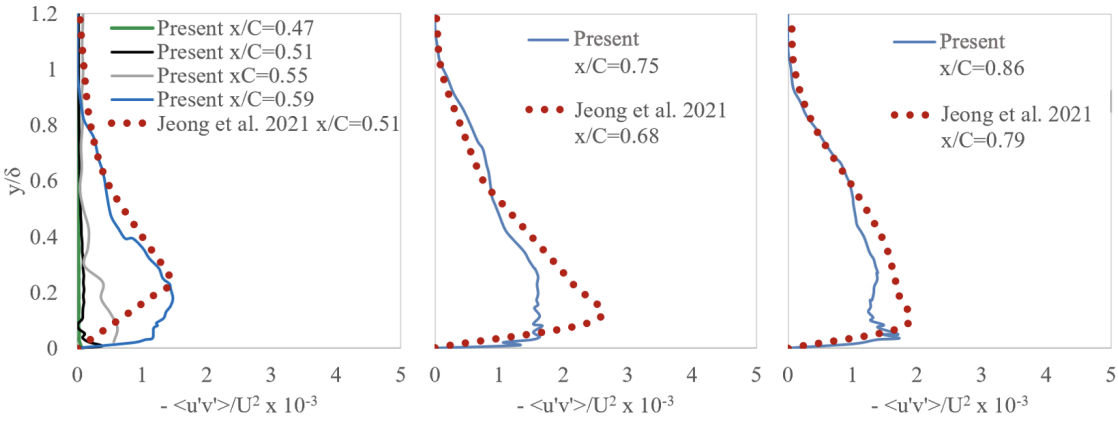


Figure 5.16: *Comparison with experimental data by Jeong et al. [7]: Reynolds shear stress profiles at Re_c=520000 for the smooth wall case*

The transition onset point detected in the experiments for this Reynolds number is around x/C=0.5, and similarly, the simulation results in fig. 5.16 suggest that the transition approximately starts in the range $0.51<x/C<0.55$ based on the position of

the first Reynolds shear stress profile diverging from zero. The mid-span contour plot in fig. 5.17 illustrates the estimated transition onset in simulations and experiments, indicating that the transition is sensibly predicted.

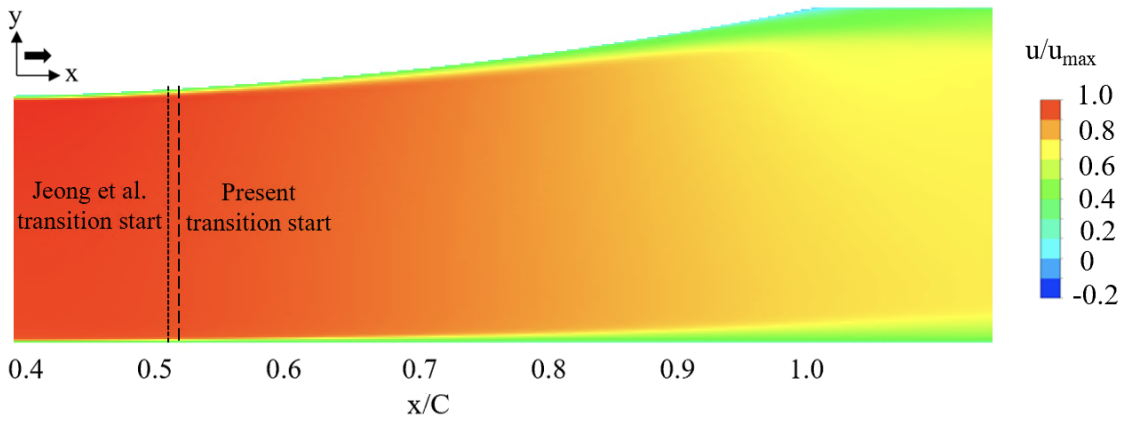


Figure 5.17: *Comparison with experimental data by Jeong et al. [7]: transition onset at* Re_c=520000

The results displayed under both high and low Reynolds number conditions demonstrate the consistency of the employed computational setup. Such a set-up is utilized in the next section to examine the behavior of an array of surface microstructures subjected to the suction side pressure gradient of a high-lift low-pressure turbine airfoil and its impact on the flow field.

5.4 Adiabatic Surface Microstructure Array

This section is dedicated to the analysis of how surface microstructures affect the flow field, employing a methodological approach similar to that of Jeong et al. [7] in their exploration of random roughness. The study will extend to include a comparison of the impacts of random roughness versus regular roughness. This comparative analysis aims

to provide a clearer understanding of the behaviors and effects each type of roughness has on the flow field.

As described in section 5.2, both the smooth and rough wall scenarios incorporate a contoured top wall with an array of surface microstructures. This design aims to minimize separation on the contoured top wall, which is not the focus of this study, and to reduce its interactions with the bottom wall boundary layer, the primary subject of interest. This approach is similar to that of Jeong et al. [7], who used a sandpaper patch around the suction peak of the contoured wall for the same objective. It is important to remark that references to 'smooth wall cases' imply the absence of roughness on the bottom wall, while 'rough wall' denotes the application of surface roughness to the bottom wall. Regardless of these distinctions, all cases incorporate surface microstructures on the contoured wall to avoid separation at the top.

The findings for the smooth and rough wall cases are presented in fig. 5.18. Specifically, fig. 5.18a displays the adiabatic smooth wall flow field, which is the same as shown in fig. 5.10, highlighting the separation onset (S) and reattachment location (R) for both present results (coarse dash line) and Jeong et al. [7] (fine dash line). The key distinction between the experimental results of Jeong et al. [7] and the present computational results obtained from Msflows, as already discussed in the previous section, lies in the downstream shift of the separation region by 5-10% of the chord length, attributable to the differences between the computational and experimental setups outlined in section 5.2.

In contrast, fig. 5.18b presents the time-averaged velocity contour for the case with

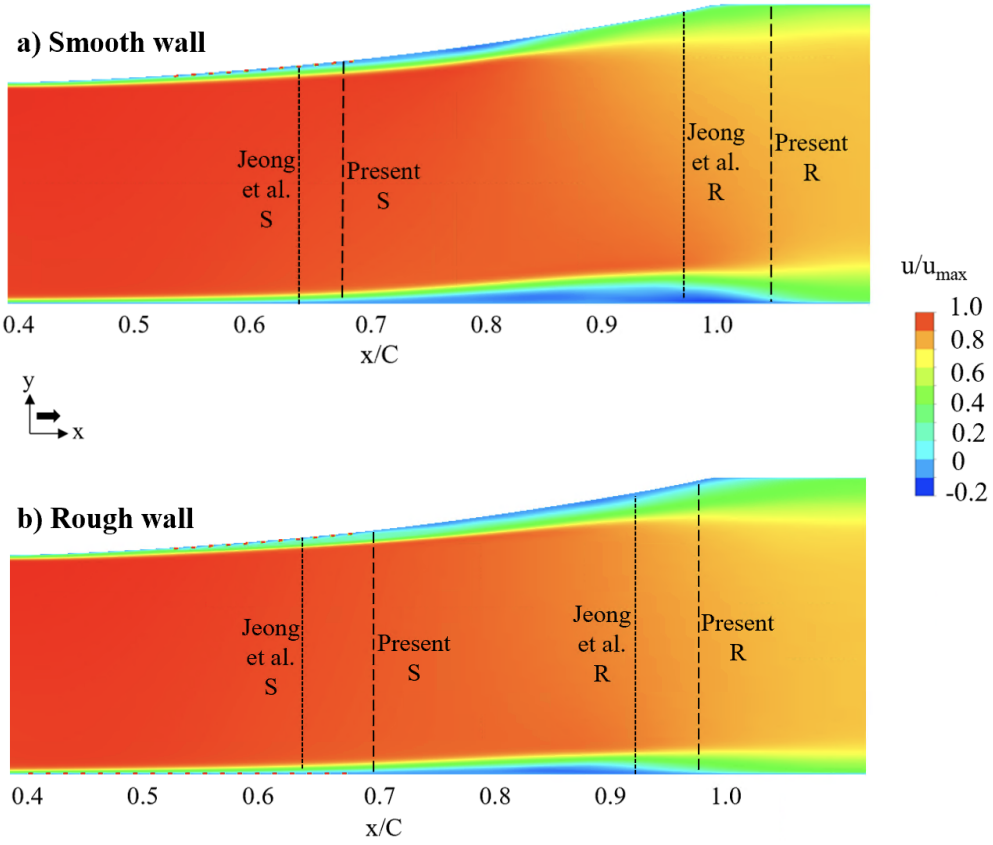


Figure 5.18: *Comparison with experimental data by Jeong et al. [7]: time-averaged flow field on a mid-span cut plane at* Re=120000 *for both a) smooth wall and b) rough wall. Separation onset and reattachment location are indicated respectively with S and R*

surface microstructures on the bottom wall (rough wall). This aligns with Jeong et al.'s findings [7] about random roughness; in fact, surface microstructures are similarly observed to substantially reduce the separation region's size. However, differences exist: first, while the random roughness in the study of Jeong et al. [7] and the regular roughness pattern in the simulation share the same R_a/C, the effect of size reduction is more pronounced with regular roughness, resulting in a 26% reduction in the separation bubble length compared to a 16% reduction for random roughness. Second, regular roughness, unlike random roughness, appears to affect the location of separation onset

(S). Jeong et al. [7] reported that increased roughness height leads to an upstream shift in transition onset but the separation onset location stays largely the same, whereas the present Msflows results show that the separation onset moves slightly downstream for the rough wall case.

Such minor observed discrepancy may be linked to the different roughness characteristics in the experiments and simulations. Although the roughness average height to chord length ratio (R_a/C) is the same, the simulations feature regular roughness with a higher skewness (Ra_{skew}=4.69) compared to the random roughness in the experiments of Jeong et al. (Ra_{skew}=1.12). Therefore, despite having the same R_a/C, the microstructures in the simulations are taller in terms of maximum height compared to the random roughness used in the experiments. The choice of a higher Ra_{skew} in simulations is influenced by computational considerations, where larger microstructures reduce mesh refinement requirements, and practical aspects related to a potential additive manufacturing process to produce microstructures of interest, such as easing the removal of excess powder during the laser sintering process and achieving a better surface finish.

The time-averaged velocity profiles for both smooth and rough wall cases are illustrated in fig. 6.1, confirming that surface microstructures contribute to a thinner boundary layer that appears less prone to separation. The flow field near the surface microstructures, as shown in fig. 5.20, remains fully laminar. This observation aligns with the experimental findings of Jeong et al. [7] who also detected a laminar flow in the area of the domain where we placed the microstructures ($0.4<x/C<0.7$).

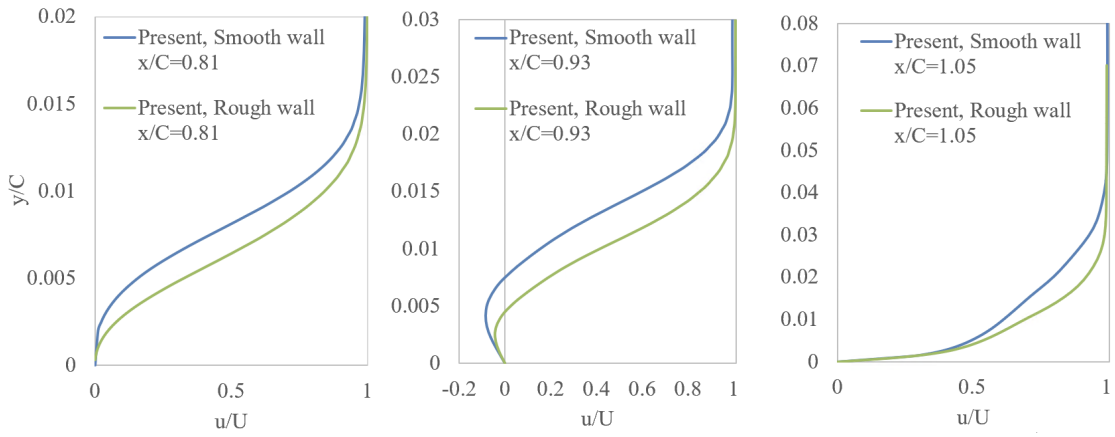


Figure 5.19: *Time-averaged velocity profiles at* $Re_c = 120000$ *for smooth and rough surface cases*

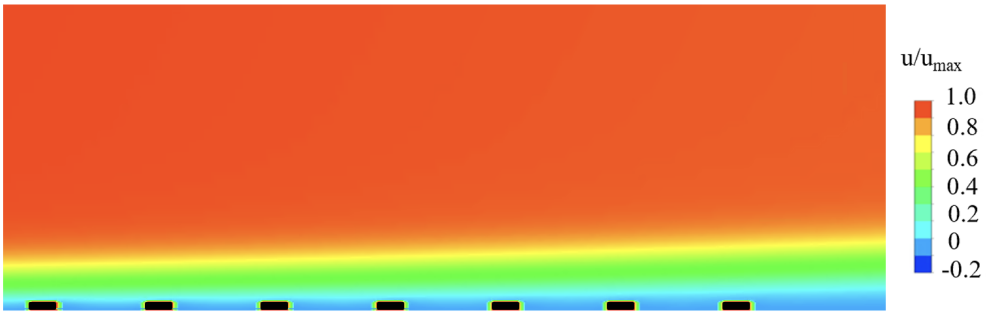


Figure 5.20: *Flow field near surface microstructures under an adverse pressure gradient at* $Re_c = 120000$

In general, significant efforts were made to align the simulations with the experimental data from Jeong et al. [7]. However, matching their maximum roughness height was impractical as it would have necessitated a much finer mesh, resulting in prohibitively high computational costs.

The difference in roughness peak height might amplify the influence of surface roughness on the separation onset location, an effect that was negligible in the experiments of Jeong et al. [7], but becomes more significant in the simulations. In this context, the regular roughness in the simulations shifts the onset of separation (S) downstream, as

illustrated in fig. 5.18.

It is also important to remark that the behavior of the contoured top wall is influenced by the boundary layer's development on the bottom wall. As depicted in fig. 5.18b, the rough bottom wall case shows a smaller separation area compared to the smooth bottom wall. This results in reduced upward flow deflection, enhancing the diffusion on the top wall and subsequently moving downstream the reattachment point of its separated region. However, this situation is not ideal since our objective is to have a passive top wall, which would enable us to observe the bottom wall's behavior without such interactions. In the experimental work by Jeong et al. [7] a sandpaper patch was applied to the contoured wall to reduce/suppress the top wall separation region, but the authors did not specify the type of sandpaper used and no published data are available to adequately model the behavior of the top wall in our simulations. The uncertainty arising from the interaction between the top and bottom walls may have been less pronounced in the experiments, although Jeong et al. [7] do not provide specific information regarding this coupling. This could be due to the random roughness used in their study having a less significant effect on the size of the bottom wall separation, potentially making the coupling effect between the top and bottom walls less relevant. Despite our efforts to closely replicate the experimental conditions in our simulations, avoiding the undesirable interaction between the top and bottom walls proved to be challenging. A potential solution could be to apply non-viscous conditions to the top wall. This insight emerged after conducting a series of computationally demanding simulations and will inform future research.

5.5 Remarks

In summary, the computational setup used demonstrates satisfactory agreement with the time-averaged flow field for the smooth wall cases, showing only minor discrepancies compared to the experimental study by Jeong et al. [7] for both Reynolds numbers of interest Re=120000 and Re=520000. These differences are likely attributable to variations between the experimental setup and the simulation, such as the presence of free-stream turbulence in the experiments or the use of a different roughness type (random roughness in the experiments and regular roughness in the simulation). Furthermore, the simulations reasonably capture the transition behavior at Re=520000 and the development of the separation region at Re=120000 for smooth wall cases, remarking that the flow behavior observed in the simulations is comparable to that illustrated in the experimental work by Jeong et al. [7].

The influence of regular roughness on the flow field is evaluated and contrasted with the rough wall results from Jeong et al. [7], who used random roughness characterized by the same R_a/C. Although both types of roughness decrease the size of the separation region, the effect of regular roughness appears more significant (26% reduction compared to 16% with random roughness). This difference is likely due to the different maximum roughness heights, with regular roughness having a higher maximum height to reduce mesh requirements and consequently the computational costs.

The results of this study suggest that merely matching the average roughness height is insufficient to fully characterize different types of roughness. Significant efforts were

made to align with the experimental data by Jeong et al. [7], however, matching their maximum roughness height proved impossible due to the requirement for a much finer mesh, which would have entailed an impractically high computational cost. Consequently, while both experimental and computational results indicate the same trend of surface roughness, which reduces the size of the separation region, the use of different roughness types prevents the results from matching exactly in quantitative terms.

Chapter 6

Heat Transfer Effects for Surfaces Under Pressure Gradient

The main objective of this chapter is to discuss the interplay between aerodynamics and heat transfer in scenarios more representative of real-world conditions than those illustrated in chapter 4. To this end, the effects of heat transfer are examined in the presence of a pressure gradient, using the same setup described in section 5.2, for a smooth wall and an array of surface microstructures.

In the subsequent sections, we test three fluid-solid temperature ratios for the two Reynolds numbers employed in the experiments by Jeong et al. [7], specifically Re_c=120000 and Re_c=520000. The adiabatic scenario (TR=1) serves as the baseline for comparison with the cooled wall (TR=0.5) and heated wall (TR=1.5) cases.

6.1 Smooth Wall

The computational domain for this case is described in fig. 5.6. To assess the impact of varying temperature ratios, all input parameters were kept constant across the simulations, with the exception of the bottom wall's thermal boundary condition. This condition was designated as adiabatic for TR=1 and isothermal for both the heated and cooled wall cases. In all scenarios, the total temperature at the inlet, T_{01}, was set at $300K$.

The input Reynolds number in Msflows was adjusted to ensure that the exit Reynolds numbers at the x/C=1 location from Jeong et al.'s experiments [7] matched those of the present Msflows simulations for the adiabatic case (TR=1). However, as will be detailed in the following paragraphs, maintaining a constant inlet Reynolds number and other input parameters while varying the fluid-solid temperature ratio results in slight deviations in the exit Reynolds numbers for different temperature ratios compared to the adiabatic case.

In the case of the lower Reynolds number (Re_c=120000), a separation region is detected under adiabatic conditions. The effect of the temperature ratio (TR) on the size of this separation region is clearly depicted in fig. 6.1. For the heated wall scenario (TR=1.5), the onset of separation occurs approximately 3% of the chord length further upstream compared to the adiabatic case (TR=1), and the reattachment is delayed roughly by 10%. In contrast, the cooled wall case (TR=0.5) shows a notable reduction in the separation bubble. Specifically, the separation onset shifts downstream by around

5% of the chord length relative to the adiabatic case, and the reattachment point moves upstream by nearly 10%.

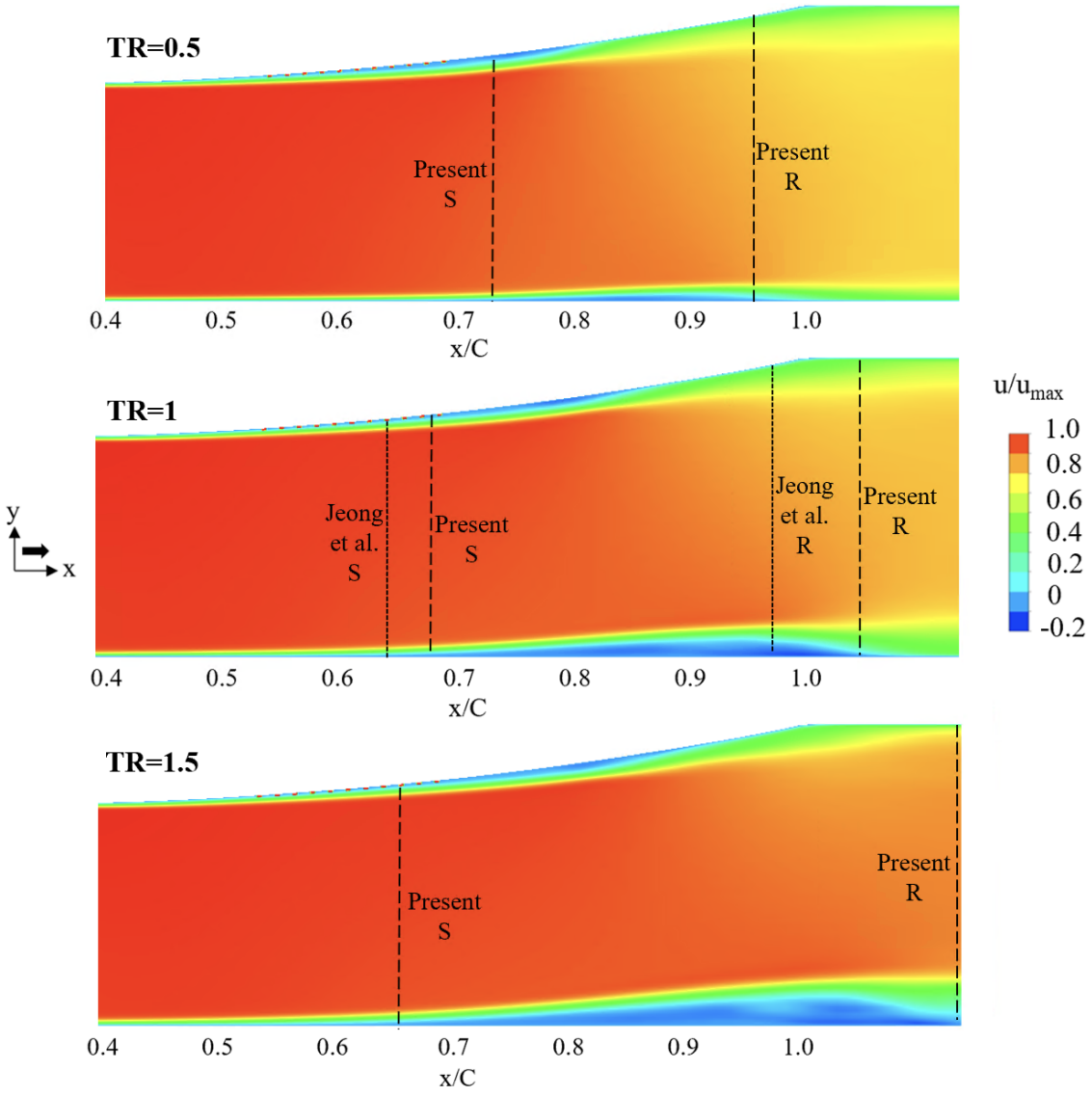


Figure 6.1: *Time-averaged flow field on a mid-span cut plane at* Re=120000 *for the smooth wall case with three different TRs: cooled wall* (TR=0.5)*, heated wall* (TR=1.5)*, and adiabatic* (TR=1)*. Separation onset and reattachment location are indicated respectively with S and R*

The exit Reynolds number Re_c is affected by wall heat transfer, exhibiting a change of approximately ±5% for TR=1.5 and TR=0.5 respectively. In fact, in the case of

the heated wall (TR=1.5), the presence of a larger separation bubble diminishes flow diffusion and deceleration, leading to a higher exit velocity. Despite the general trend described by Jeong et al. [7] of a higher Reynolds number correlating with a smaller separation region, in this instance, the opposite effect is observed. Such behavior can be attributed to the fact that the globally defined exit Reynolds number does not account for the local effects of wall heat transfer on fluid properties near the wall, nor its impact on the flow field.

As observed in figs. 3.5 and 3.6 for a flat plate laminar boundary layer under zero pressure gradient, heat transfer significantly alters local fluid properties and, consequently, the flow field. Therefore, similarly to the previous chapters, to evaluate the impact of wall heat transfer on the flow field within a boundary layer, the local Reynolds number calculated using local fluid properties and velocity as defined in eq. (6.1) is introduced. This should not be confused with the commonly used Reynolds number based on the local distance Re_x=$\rho_\infty u_\infty x/\mu_\infty$.

$$Re_{local}(x,y) = \frac{\rho(x,y)\ u(x,y)\ x}{\mu(x,y)} \tag{6.1}$$

To gain a clearer understanding of this phenomenon, the influence of the temperature ratio (TR) on both the flow field and the local Reynolds number profiles is illustrated in fig. 6.2a and fig. 6.2b, respectively, at x/C=0.4, a point upstream of the separation bubble. Similarly to the observations in figs. 3.3 and 3.5 for a flat-plate laminar boundary layer under a zero pressure gradient, in the presence of a pressure

gradient, a cooled wall (TR=0.5) results in a thinner boundary layer and a significantly increased local Reynolds number. In contrast, a heated wall (TR=1.5) leads to a thicker boundary layer and a decreased local Reynolds number. This reduction in the local Reynolds number near the wall observed at TR=1.5 explains why, regardless of the increase in the exit Reynolds number Re_c, an enlargement of the separation region is detected for the heated wall scenario.

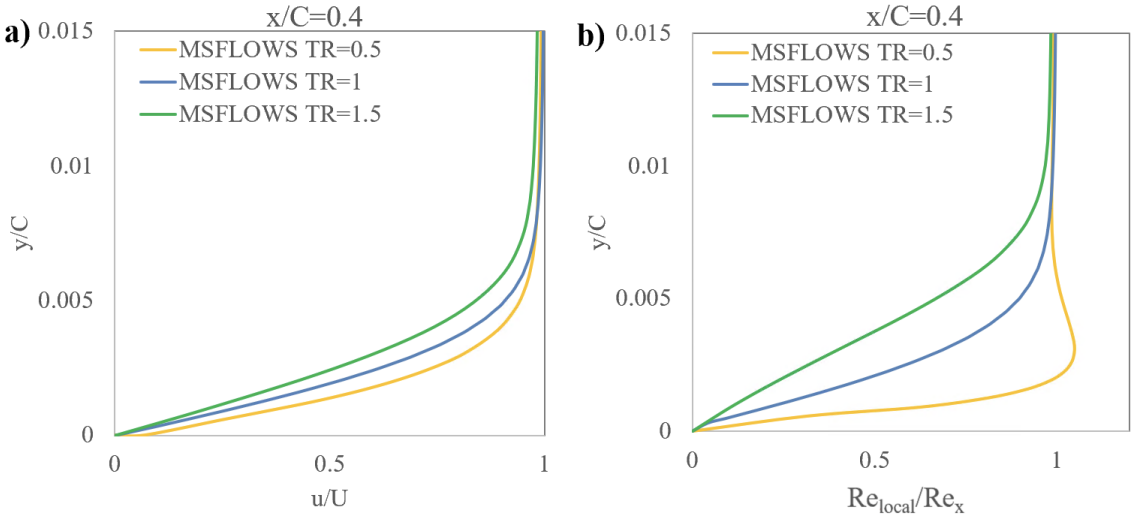


Figure 6.2: *Impact of TR on the a) time-averaged velocity profile, and b) local Reynolds number profile at Re_c=120000, upstream of the separation bubble for the smooth wall case*

One might ask why, in the case of surface microstructures under a zero pressure gradient, as detailed in fig. 4.9, the separation region behind each microstructure tends to expand in the cooled wall scenario (TR=0.5) for laminar flows, yet a seemingly different effect is observed for the separation region due to contoured wall diffusion. It is crucial to recognize that the flow dynamics in these cases is markedly different. For laminar flows over hemispheres, the separation point is primarily determined by

the shape of the microstructure itself. Then a higher local fluid inertia, a result of the cooled wall, causes the flow to reattach further downstream. Moreover, in turbulent flows over surface microstructures, as seen in fig. 4.19, the separation region is reduced in the cooled wall case (TR=0.5), a consequence of increased turbulent diffusion due to a higher local Reynolds number. In contrast, flow separation prompted by contoured wall diffusion exhibits a different behavior, initially beginning as a laminar separation caused by the pressure gradient of the contoured wall and then transitioning to turbulent in the vicinity of the maximum bubble height streamwise location, as shown by Jeong et al. [7]. This accounts for the earlier reattachment observed in the adiabatic case, where the local Reynolds number is higher compared to the heated wall case (TR=1.5).

Besides the difference mentioned, the zero pressure gradient surface microstructure case from chapter 4 and the contoured wall scenario detailed in the present section exhibit a similar transition mechanism. In both cases, the shear layer separation — caused, respectively, by the presence of microstructures and by the pressure gradient of the contoured wall — becomes unstable, leading to a bypass transition. This is consistent with the findings of Jeong et al. [7], who observed the onset of the transition near the maximum height of the separation bubble in the contoured wall case. The impact of the temperature ratio on the separation bubble maximum height/transition onset location (MH) is illustrated in fig. 6.3. This shows that the location is shifted stream-wise by roughly $\pm$7% of the chord length for TR=1.5 and TR=0.5, respectively, compared to the adiabatic case.

The fact that the separation bubble maximum height location for the adiabatic

case by Jeong et al. [7] is roughly 10% of the chord length upstream of that from the present simulation aligns with the differences in the experimental set-up discussed in section 5.2 causing an overall shift of the separation region position as illustrated in fig. 5.10. Thus, although there are minor differences between the experimental and simulation setups, the overall trend of the temperature ratio affecting the position of the separation bubble maximum height location is consistent with the other computational findings highlighted in this thesis.

Interestingly, a similar impact of ±5% on the position of the transition onset point was detected by Jeong et al. [7] in their adiabatic experiments of rough surfaces in which three different roughness heights were tested. This analogy indicates that the separation bubble on a smooth wall, subject to three distinct temperature ratios, is affected in a similar way by varying thermal boundary conditions as an adiabatic wall with three different surface finishes. Similarly to the cooled wall case (TR=0.5), the highest roughness finish resulted in a reduced separation bubble, with its maximum height location shifted upstream.

The other Reynolds number of interest is Re=520000 and its time-averaged flow field is illustrated in fig. 6.4 for three different temperature ratios (TRs): cooled wall (TR=0.5), heated wall (TR=1.5), and adiabatic (TR=1). Although all TR values exhibit similar behavior with no formation of a separation bubble, the thickness of the boundary layer is noticeably influenced by the varying wall thermal boundary conditions. Additionally, the transition onset location is identified in fig. 6.4, based on the streamwise position where the first nonzero Reynolds shear stress profile is detected,

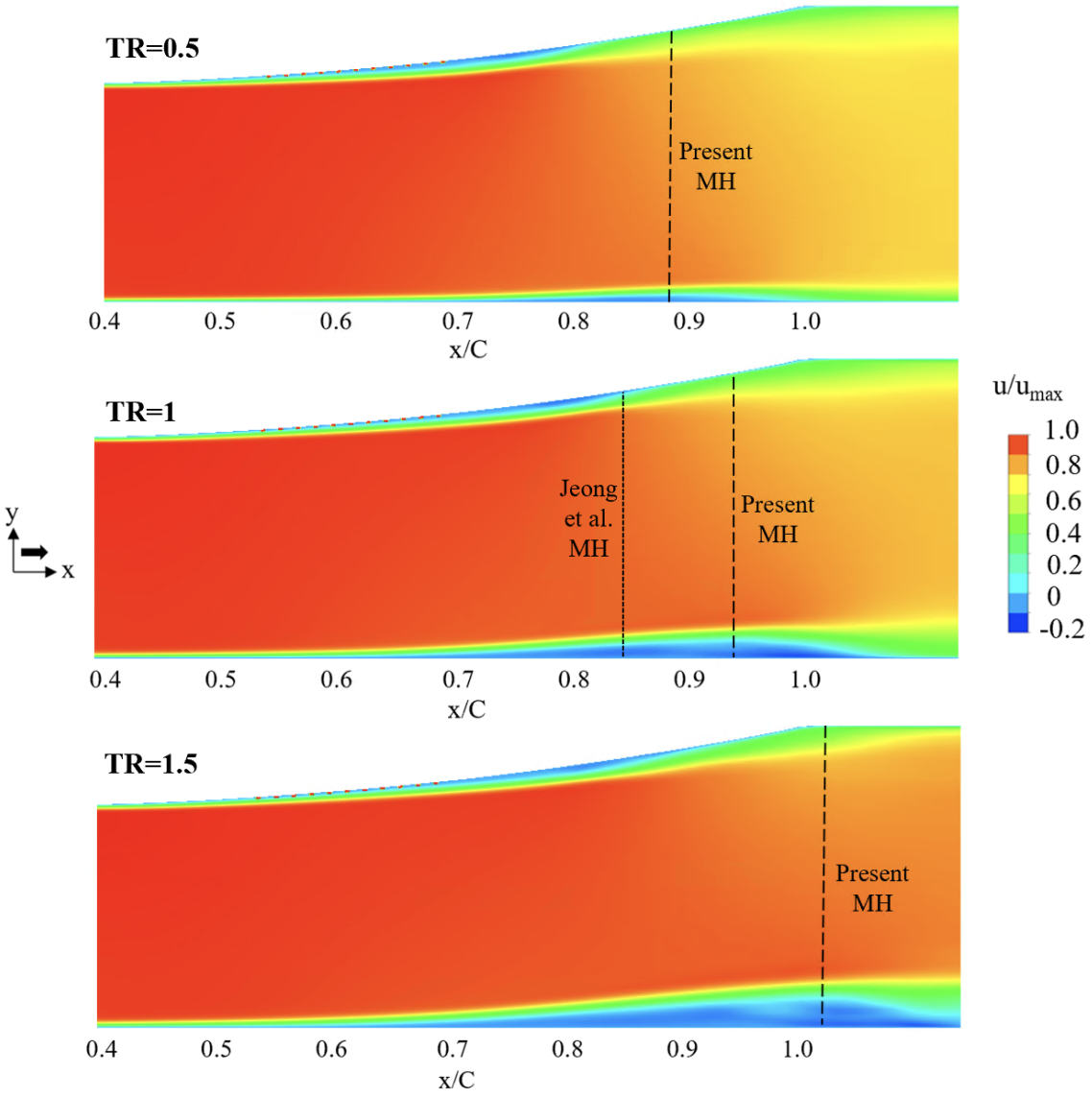


Figure 6.3: *Impact of TR on the separation bubble maximum height location (MH) at* Re_c=120000*for the smooth wall case*

following a similar approach used for the adiabatic case in fig. 5.16.

To quantitatively assess the impact of the temperature ratio (TR) on the boundary layer profile, the mid-span time-averaged velocity profiles at the exit are presented in fig. 6.5a. As discussed in fig. 3.3, for a flat plate laminar boundary layer under zero pressure gradient, wall heating notably thickens the boundary layer, while wall

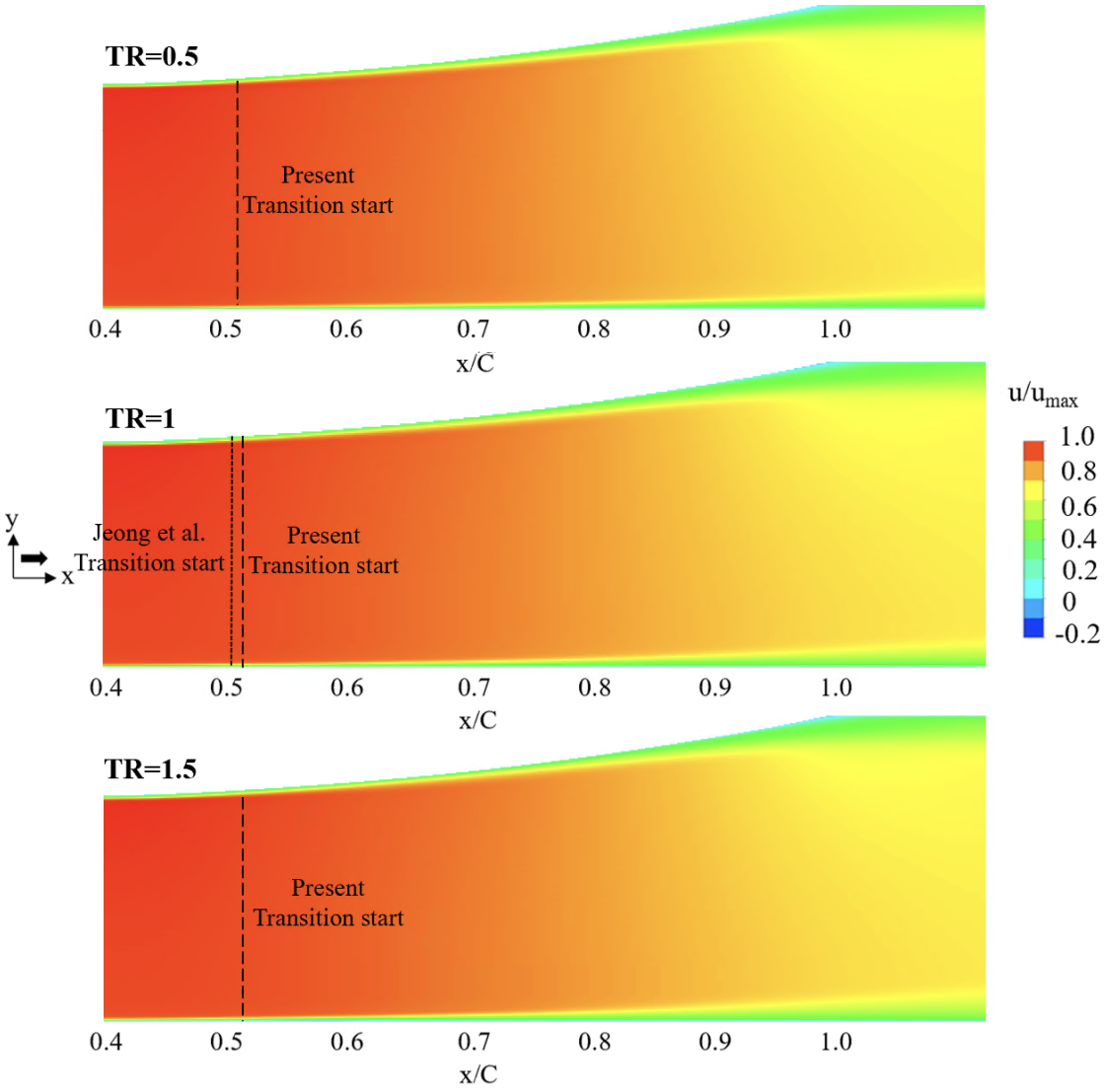


Figure 6.4: *Time-averaged flow field on a mid-span cut plane at* Re=520000 *for the smooth wall case with three different TRs: cooled wall* (TR=0.5)*, heated wall* (TR=1.5)*, and adiabatic* (TR=1)*. Transition onset locations are indicated with dash lines*

cooling demonstrates the opposite effect. The same trend was also observed for a smooth surface boundary layer under the suction side pressure gradient of a high-lift low-pressure turbine airfoil.

It is important to note that, unlike the flat-plate laminar boundary layer under

zero pressure gradient shown in fig. 3.3, in this case the flow field at x/C=1.06 is fully turbulent. Despite this difference, the impact on the boundary layer thickness for a smooth surface under a pressure gradient is approximately ±20% for TR=1.5 and TR=0.5, respectively. This variation is quantitatively very similar to what is observed for a laminar flat-plate boundary layer under zero pressure gradient.

In agreement with section 3.1, fig. 6.5b illustrates that such effect leads to a notable difference in terms of the local Reynolds number, resulting in a substantial increase in Re_{local} within the boundary layer for the cooled wall case (TR=0.5) and a decrease for the heated wall case (TR=1.5).

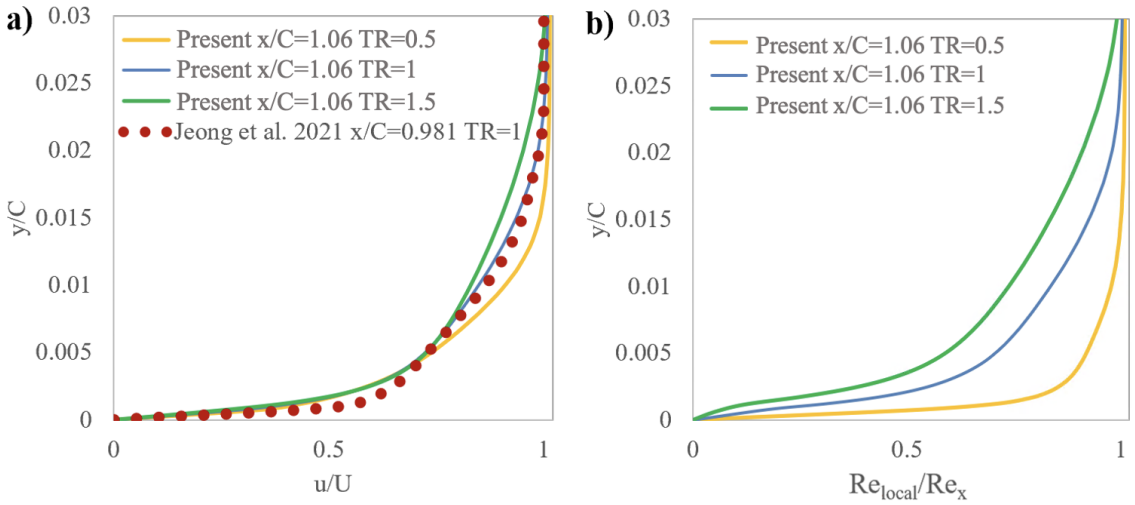


Figure 6.5: *Impact of TR on the a) time-averaged velocity profile, and b) local Reynolds number profile at Re_c=520000for the smooth wall case*

In the studies conducted by Jeong et al. [7] at Re_c=520000, various roughness levels had minimal impact on the transition onset position, with even the roughest surface showing only a slight deviation compared to a smooth wall. In parallel, the temperature ratio (TR) study reveals that, although TR significantly affects the local Reynolds

number profile, the transition onset location is largely unchanged by different thermal boundary conditions, as detailed in fig. 6.4. This finding appears to contrast with chapter 4, where TR markedly influenced the critical Reynolds number in flows over surface microstructures under zero pressure gradient. However, this discrepancy can be attributed to differences in the cases studied: the smooth wall under pressure gradient at Re_c=520000 case is characterised by a natural transition, not influenced by the separated shear layer, unlike the surface microstructures under the zero pressure scenario and the smooth wall under pressure gradient at Re_c=120000 case where transition was caused by the separated shear layer becoming unstable. Additionally, it is important to note that the absence of free-stream turbulence in the simulations further reinforces the case for natural transition. In this context, accurately detecting the precise natural transition behavior becomes computationally even more challenging, necessitating an exceptionally fine mesh.

It is rather difficult to assess the impact that thermal boundary conditions will have on different transition types as two contrasting mechanisms take place; for example, in the case of the cooled wall (TR=0.5), an increased local Reynolds number in the boundary layer tends to induce turbulence, while a thinner boundary layer stabilizes the flow against the pressure gradient from the contoured wall. The distinct responses to thermal boundary conditions in bypass and natural transition scenarios are further supported by the literature review in section 2.3.1, which includes multiple studies documenting the stabilizing effect of cooling in natural transition cases.

6.2 Surface Microstructure Array

The primary objective of this section is to describe the interaction between aerodynamics and heat transfer when surface microstructures are present. We utilize the computational setup detailed in fig. 5.7 to study the behavior of an array of surface microstructures under a pressure gradient with varying wall thermal conditions. In assessing different temperature ratios, all input parameters were kept constant throughout all simulations, with the exception of the bottom wall thermal boundary condition. This condition was configured as adiabatic for TR=1, and as isothermal for both the heated and cooled wall cases. T_{01} was consistently set at $300K$ for all scenarios. Given the computational cost and the fine mesh required to directly resolve the flow field around surface microstructures, only results for the Re_C=120000 case are presented in this section.

Consistent with the observations of an adiabatic wall as presented in section 5.4, it appears that a rough wall consistently diminishes or even suppresses the size of the separation bubble across all temperature ratios of interest. This trend is clearly demonstrated in fig. 6.6, especially when compared to the smooth bottom wall case depicted in fig. 6.1. This effect suggests that surface roughness introduces a significant alteration in flow dynamics within the boundary layer, influencing the separation behavior by reducing the size of the separation bubble under all the thermal conditions tested.

Compared with the adiabatic scenario, the surface microstructure case at TR=1.5 exhibits an upstream shift in the separation onset point by approximately 4% of the

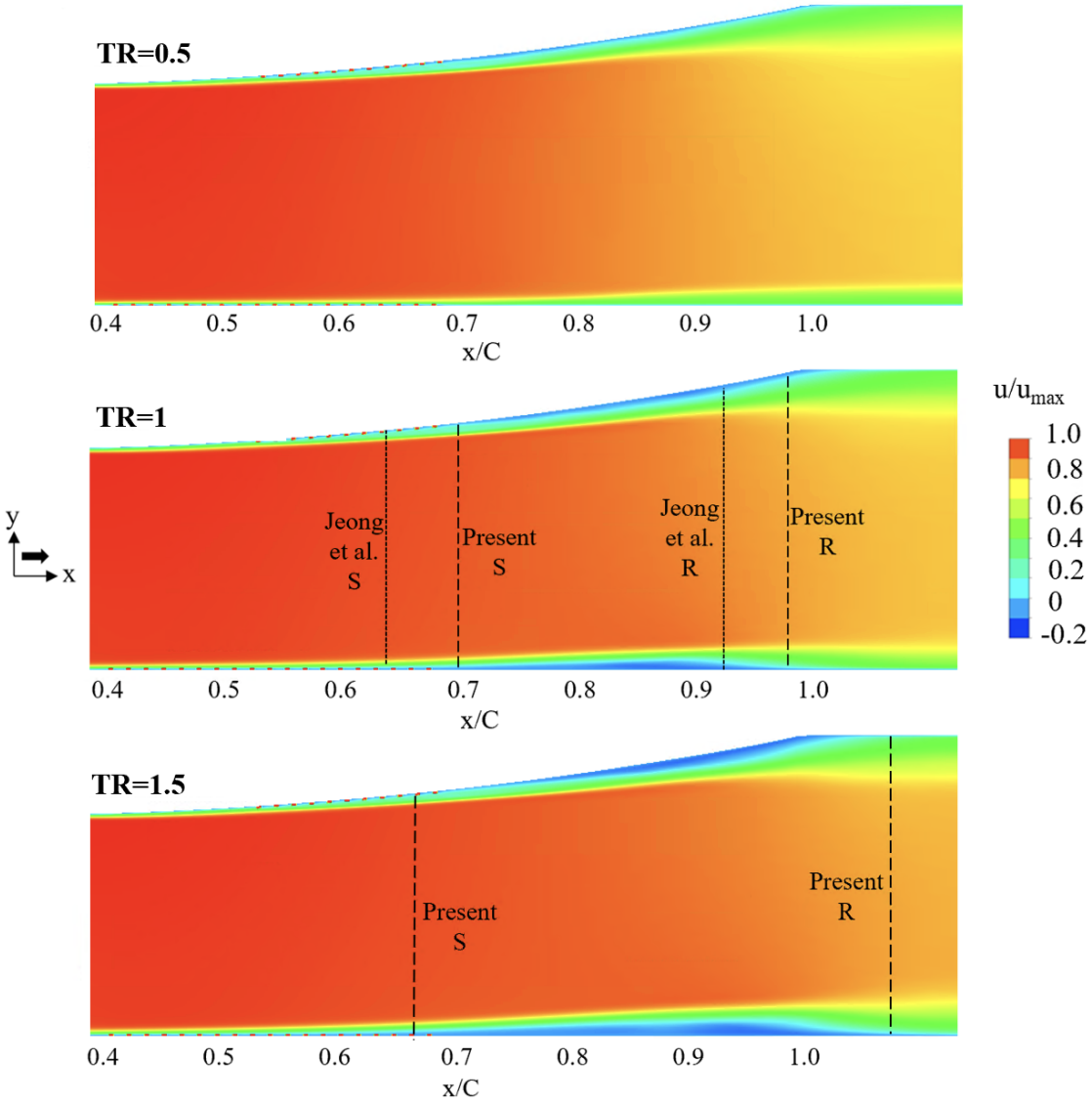


Figure 6.6: *Time-averaged flow field on a mid-span cut plane at* Re=120000 *for the rough wall case with three different TRs: cooled wall* (TR=0.5)*, heated wall* (TR=1.5)*, and adiabatic* (TR=1)*. Separation onset and reattachment location are indicated respectively with S and R*

chord length and a downstream shift in the reattachment point by 10% of the chord length. In contrast, at TR=0.5, there is a complete suppression of the separation bubble.

Interestingly, it appears that both wall cooling and surface microstructures exert

a similar influence on the separation region, as both factors contribute to reducing or even suppressing the separation region.

Regarding the flow behavior around surface microstructures under different wall thermal conditions and a low-pressure turbine pressure gradient, results consistent with those observed in chapter 4 have been found. Specifically, the surface microstructures on the bottom surface are located in a region that is entirely laminar ($0.4<x/C<0.7$), and similar to the findings for an array of hemispherical surface microstructures under a zero pressure gradient (as referenced in fig. 4.9), the recirculation region between the microstructures is enlarged for cooled walls due to increased local fluid inertia caused by higher local density, and reduced for heated walls, as depicted in fig. 6.7.

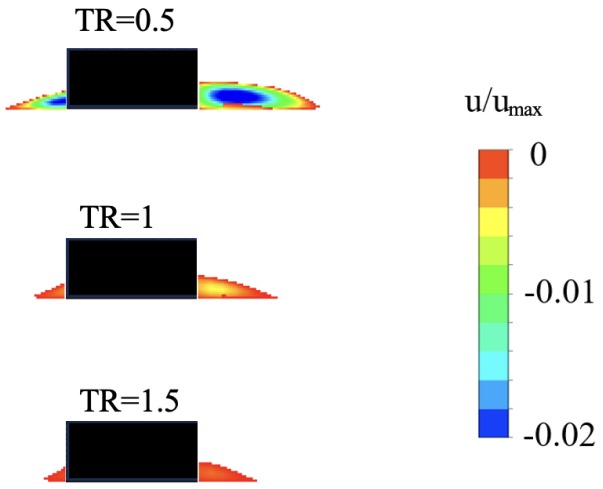


Figure 6.7: *Impact of TR on the velocity field near surface microstructures under a pressure gradient at Re=120000. The contour is clipped at $u/u_\infty=0$, thus reversed flow only is depicted*

6.3 Remarks

As discussed in the literature review in section 2.3, significant temperature differences between the freestream and the wall lead to a notable coupling of aerodynamic and thermal fields. This coupling manifests itself through the influence of wall heat transfer on the local fluid properties, which affect the flow field. Simultaneously, alterations in the flow field have a reciprocal effect on heat transfer, thus establishing a bidirectional interaction.

The findings in this chapter corroborate observations from chapters 3 and 4 for a flat plate and a small array of surface microstructures under a zero pressure gradient. They show that heat transfer has a significant impact on the flow field, even in more complex settings such as a larger array of microstructures under the suction side pressure gradient of a high-lift low-pressure turbine airfoil.

In particular, wall cooling in the presence of a pressure gradient has been found to reduce the boundary layer thickness, while heating tends to enhance it. This behavior aligns with previous findings for a flat-plate boundary layer under zero pressure gradient. Additionally, the size of the separation bubble at Re=120000 is also significantly affected by heat transfer. Specifically, the separation bubble is considerably reduced by the cooled wall (TR=0.5) and enlarged by the heated wall (TR=1.5)

Similarly to the methods outlined in chapters 3 and 4, the local Reynolds number is utilized as the key parameter to underscore the significance of the interaction between aerodynamics and heat transfer. This approach also reveals the inadequacy of the

globally defined Reynolds number in capturing the flow behavior near the wall. For instance, in the case of the heated wall, contrary to conventional wisdom and the general trend of separation regions diminishing at higher Reynolds numbers as illustrated by Jeong et al. [7], the separation region appeared to increase in size even though the exit Reynolds number was effectively higher. This behavior can be attributed to a significant reduction in the near-wall local Reynolds number caused by wall heating. Similarly, wall cooling was observed to increase the local Reynolds number in the boundary layer, resulting in a reduced separation region.

This chapter also examines heat transfer effects for regular roughness under a pressure gradient. The anticipated trend, where surface roughness reduces the size of the separation region at Re=120000, was confirmed across different temperature ratios. Additionally, it was observed that combining wall cooling (TR=0.5) with the surface roughness array leads to the complete suppression of the separation bubble.

Chapter 7

Conclusions and Future Work

7.1 Conclusions

The primary objective of this thesis is to investigate the interactions between aerodynamics and heat transfer, a complex problem in both academic research and industrial practice where the flow field and thermal field are often considered uncoupled.

The studies conducted range from a simple flat-plate boundary layer to more complex configurations involving arrays of surface microstructures. These investigations, presented across various chapters, provide insights into the interplay between aerodynamics and heat transfer, emphasizing that wall heat transfer significantly alters the fluid properties near the wall and, consequently, the flow field.

The comprehensive literature review establishes a foundational understanding of the significant effects of surface finish and heat transfer on flow mechanisms. It highlights the complexities in characterizing the impact surface roughness, particularly focusing on

the distinction between regular and random roughness. Additionally, the review identifies limitations in the application of Newton's law of cooling, especially in the context of interactions between aerodynamics and heat transfer in scenarios with pronounced fluid-solid temperature differences. It also presents various cases where heat transfer was observed to have a significant impact on aerothermal properties and discusses its influence on laminar-turbulent transition. Finally, the literature review explores the potential of conjugate heat transfer analysis in addressing these cases and the use of multiscale models to study arrays of surface microstructures.

The study of the laminar flat plate boundary layers under various thermal boundary conditions calls into question the usefulness of conventional parameters such as the friction coefficient (C_f) and Nusselt number (Nu) for highlighting the interaction between aerodynamics and heat transfer. The research demonstrates that these parameters might mask the actual impact of heat transfer on the flow, revealing the local Reynolds number as a more representative parameter to describe the coupling between flow and thermal fields.

The investigation then focuses on regular roughness under a zero pressure gradient, revealing that substantial variations in the local Reynolds number distribution occur around surface microstructures. Additionally, a clear influence of heat transfer on the flow field is observed, particularly in terms of significant changes in the separation region development behind each microstructure for the different fluid-solid temperature ratios analyzed. This includes a substantially delayed reattachment point for cooled walls due to increased local fluid inertia. A notable shift in the critical Reynolds num-

ber is also observed for the tested temperature ratios, indicating an earlier transition to turbulent flow for cooled walls and a delayed transition for heated walls. Furthermore, this study introduces a new method for scaling wall heat transfer effects, with potential applications in aerothermal engineering for practically estimating flow performance parameters at different temperature ratios.

In order to analyze the behavior of surface microstructures under different wall thermal conditions in more realistic scenarios, this thesis examines a larger array of surface microstructures under the pressure gradient of a high-lift, low-pressure turbine airfoil. Initially, the computational setup is validated against the experimental work by Jeong et al. [7], demonstrating good agreement for a smooth wall boundary layer under a pressure gradient in terms of time-averaged flow field, transition onset position, and flow separation. Subsequently, the behavior of an adiabatic array of surface microstructures is compared to the random roughness pattern used in Jeong et al.'s experiments. Although both computational and experimental results show a general trend of roughness reducing the size of the separation region, the differences in roughness types — regular roughness in the simulations and random roughness in the experiments with the same average height — quantitatively result in a slightly different effect. Specifically, there is a 26% separation length reduction for regular roughness compared to a 16% reduction for random roughness, and such discrepancy underscores that R_a may be an insufficient parameter to fully characterize surface roughness.

The final results chapter investigates the interactions between aerodynamics and heat transfer in the context of an array of surface microstructures under a pressure

gradient in scenarios with significant temperature differences. The findings confirm a significant coupling between aerodynamics and heat transfer, extending the observations made for a smaller array of microstructures under zero pressure gradient. Once again, wall cooling is shown to reduce the boundary layer thickness and significantly increase the local Reynolds number in the near wall region, while wall heating thickens the boundary layer and reduces the local Reynolds number. Consequently, the size of the separation bubble is also affected by different temperature ratios, demonstrating a substantial reduction in the case of wall cooling and an enlargment for the heated wall case.

In addition, this study covers the behavior of surface microstructures under a pressure gradient with heat transfer, confirming the anticipated trend where surface roughness reduces the size of the separation region at Re=120000 across various temperature ratios. Furthermore, it was observed that the combination of wall cooling (TR=0.5) with the surface roughness array employed in this study results in complete suppression of the separation bubble.

In conclusion, this thesis contributes to the fields of aerodynamics and thermodynamics by examining the aerothermal behavior of surfaces under different thermal conditions. The research presented addresses specific gaps in existing literature and suggests directions for future studies, particularly in the areas of multiscale solver applications and conjugate heat transfer analysis. The findings provide insights that are relevant to the design and engineering of surfaces in aerodynamic applications, highlighting the importance of understanding the interplay between flow dynamics, heat

transfer, and surface characteristics. They can be summarized as follows:

- The flat-plate laminar BL study reveals that conventional parameters such as the friction coefficient and Nusselt number can mask the true impact of heat transfer on flow dynamics, with the local Reynolds number being a more revealing descriptor of the interaction between flow and thermal fields

- Similar to the flat-plate case, significant variations in the local Reynolds number distribution are observed around surface microstructures due to heat transfer, with increased values for cooled walls and lower values for heated walls. Heat transfer also influences the size of the separation regions between the microstructures

- For surface microstructures under heat transfer, a notable shift in the critical Reynolds number is observed for the tested fluid-solid temperature ratios, indicating an earlier transition to turbulent flow for cooled walls and a delayed transition for heated walls

- The incompressible flow model that entails constant fluid properties and decoupled flow and thermal fields is completely unable to capture the temperature ratio influence on laminar-turbulent transition

- A novel method for scaling wall heat transfer effects is introduced, offering practical applications in aerothermal engineering for estimating flow performance parameters at different temperature ratios

- Both regular roughness (from present simulations) and random roughness (from experimental data in the literature) under the pressure gradient of a high-lift, low-pressure turbine airfoil reduce the size of the separation region caused by such pressure gradient. However, regular roughness shows a larger reduction (26%) compared to random roughness (16%).

- The study confirms a notable coupling between aerodynamics and heat transfer in the presence of a pressure gradient. Wall cooling reduces boundary layer thickness and increases the local Reynolds number, which translates into a reduction in the size of the separation bubble, while wall heating has the opposite effect

- Combining wall cooling (TR=0.5) with the presence of an array of surface microstructures results in complete suppression of the separation bubble caused by the LP turbine pressure gradient

7.2 Future work

The findings discussed in the present thesis highlight the significance of interactions between aerodynamics and heat transfer, suggesting that a conjugate approach is essential for a comprehensive understanding of the aerothermal behavior of surface microstructures in challenging environments. Additionally, the use of multiscale solvers like the one described in this thesis has the potential to enable the design of surface microstructure arrays that improve the aerothermal performance of hot components. Therefore, further development and parallelization of Msflows represent a clear direction for fu-

ture research. This approach, combined with the experimental validation of the heat transfer effects discussed in this thesis, could significantly enhance awareness within the heat transfer scientific community about the crucial interplay between heat transfer and aerodynamics, which is often not taken into account due to the complexity of the problem.

Another possible direction for future work is the implementation and development of the SHTC concept introduced by He [70]. This approach aims to achieve more accurate evaluations of HTC in cases of non-uniform wall temperature and linear energy equations. Additionally, SHTC could also be used when the temperature field actively interacts with the velocity field (non-linear aerothermal regime) by applying local linearization and decomposing a full thermal variable into a nonlinear base and a locally linear perturbation.

References

[1] Nanoscribe website: https://www.nanoscribe.com.

[2] X. Miao, Q. Zhang, C. Atkin, Z. Sun, and Y. Li. Improving Purge Air Cooling Effectiveness by Engineered End-Wall Surface Structures—Part I: Duct Flow. *Journal of Turbomachinery*, 140(9), 2018.

[3] K. K. Ferster, K. L. Kirsch, and K. A. Thole. Effects of Geometry, Spacing, and Number of Pin Fins in Additively Manufactured Microchannel Pin Fin Arrays. *Journal of Turbomachinery*, 140(1), 2017.

[4] R. J. Moffat. What's new in convective heat transfer? *International Journal of Heat and Fluid Flow*, 19(2):90–101, 1998.

[5] R. Maffulli and L. He. Wall temperature effects on heat transfer coefficient for high-pressure turbines. *Journal of Propulsion and Power*, 30(4):1080–1090, 2014.

[6] R. Maffulli and L. He. Impact of Wall Temperature on Heat Transfer Coefficient and Aerodynamics for Three-Dimensional Turbine Blade Passage. *Journal of Thermal Science and Engineering Applications*, 9(4), 04.

[7] H. Jeong and S. J. Song. Surface Roughness Impact on Boundary Layer Transition and Loss Mechanisms Over a Flat-Plate Under a Low-Pressure Turbine Pressure Gradient. *Journal of Turbomachinery*, 144(1), 2021.

[8] N. Shahrubudin, T.C. Lee, and R. Ramlan. An overview on 3d printing technology: Technological, materials, and applications. *Procedia Manufacturing*, 35:1286–1296, 2019.

[9] W. Gao, Y. Zhang, D. Ramanujan, K. Ramani, Y. Chen, C.B. Williams, C.L. Wang, Y.C. Shin, S. Zhang, and P.D. Zavattieri. The status, challenges, and future of additive manufacturing in engineering. *Computer-Aided Design*, 69:65–89, 2015.

[10] B. Blakey-Milner, P. Gradl, G. Snedden, M. Brooks, J. Pitot, E. Lopez, M. Leary, F. Berto, and A. du Plessis. Metal additive manufacturing in aerospace: A review. *Materials Design*, 209, 2021.

[11] T. Blachowicz and A. Ehrmann. 3d printed mems technology—recent developments and applications. *Micromachines*, 11(4), 2020.

[12] E. Sachs, M. Cima, P. Williams, D. Brancazio, and J. Cornie. Three Dimensional Printing: Rapid Tooling and Prototypes Directly from a CAD Model. *Journal of Engineering for Industry*, 114(4):481–488, 11 1992.

[13] F. Walachowicz, I. Bernsdorf, Ulrike Papenfuss, C. Zeller, A. Graichen, V. Navrotsky, N. Rajvanshi, and C. Kiener. Comparative energy, resource and recycling

lifecycle analysis of the industrial repair process of gas turbine burners using conventional machining and additive manufacturing. *Journal of Industrial Ecology*, 21(S1):S203–S215, 2017.

[14] V. Navrotsky. Industrialization and field experience of 3d printed gas turbine components. *siemens.com/gas-power*, 2019.

[15] S. Tanigawa, M. Kataoka, M. Taneike, R. Ito, T. Komaki, and N. Motoyama. Development of metal am technology for gas turbine components. *Journal of the Global Power and Propulsion Society*, (July):49–65, 2023.

[16] T. Kellner. The blade runners: This factory is 3d printing turbine parts for the world's largest jet engine. *GE News*, 2018.

[17] B. Sevenson. Ge considers 3d printing turbine blades for next generation boeing 777x's ge9x engines. *3DPrint.com/The Voice of 3D Printing/Additive Manufacturing*, 2014.

[18] T. Kellner. Mind meld: How ge and a 3d-printing visionary joined forces. *GE News*, 2017.

[19] Siemens website: https://press.siemens.com/global/en/pressrelease/siemens-achieves-breakthrough-3d-printed-gas-turbine-blades, 2017.

[20] J. C. Snyder and K. A. Thole. Performance of Public Film Cooling Geometries Produced Through Additive Manufacturing. *Journal of Turbomachinery*, 142(5), 04 2020.

[21] R. Xu, Z. Cheng, and P. Jiang. Fundamentals and recent progress of additive manufacturing-assisted porous materials on transpiration cooling. *Journal of the Global Power and Propulsion Society*, (July):19–48, 2023.

[22] K. Chu, R. Enright, and E. N. Wang. Structured surfaces for enhanced pool boiling heat transfer. *Applied Physics Letters*, 100(24):241603, 2012.

[23] L. He. Editorial: Some advances in additive manufacturing for aerothermal technologies. *Journal of the Global Power and Propulsion Society*, (July):1–2, 2023.

[24] A. W. Gebisa and H. G. Lemu. Additive manufacturing for the manufacture of gas turbine engine components: Literature review and future perspectives. *Ceramics; Controls, Diagnostics, and Instrumentation; Education; Manufacturing Materials and Metallurgy*, 6, 2018.

[25] A. Riemer, S. Leuders, M. Thöne, H.A. Richard, T. Tröster, and T. Niendorf. On the fatigue crack growth behavior in 316l stainless steel manufactured by selective laser melting. *Engineering Fracture Mechanics*, 120:15 – 25, 2014.

[26] N. Rao. Materials for gas turbines – an overview. *Advances in Gas Turbine Technology*, 2011.

[27] C. K. Stimpson, J. C. Snyder, K. A. Thole, and D. Mongillo. Roughness Effects on Flow and Heat Transfer for Additively Manufactured Channels. *Journal of Turbomachinery*, 138(5):051008, 2016.

[28] A. J. Wildgoose and K. A. Thole. Variability in additively manufactured turbine cooling features. *Journal of the Global Power and Propulsion Society*, (July):3–18, 2023.

[29] M. Stripf, A. Schulz, and S. Wittig. Surface Roughness Effects on External Heat Transfer of a HP Turbine Vane . *Journal of Turbomachinery*, 127(1):200–208, 2005.

[30] M. N. Goodhand and R. J. Miller. The Impact of Real Geometries on Three-Dimensional Separations in Compressors. *Journal of Turbomachinery*, 134(2), 2011.

[31] A. Vyatskikh, S. Delalande, A. Kudo, X. Zhang, C. M. Portela, and J. R. Greer. Additive manufacturing of 3d nano-architected metals. *Nature Communications*, 9(1), 2018.

[32] Thomas M. Corbett, Karen A. Thole, Daniel Ryan, and Sudhakar Bollapragada. Impacts of Superalloys on the Surface Quality of Additively Manufactured Channels. *Journal of Turbomachinery*, 146(8):081003, 03 2024.

[33] G. Ranjith Kumar, M. Sathishkumar, M. Vignesh, M. Manikandan, G. Rajyalakshmi, R. Ramanujam, and N. Arivazhagan. Metal additive manufacturing of commercial aerospace components – a comprehensive review. *Proceedings of the Institution of Mechanical Engineers, Part E: Journal of Process Mechanical Engineering*, 237(2):441–454, 2023.

[34] M. Kapsis and L. He. Analysis of Aerothermal Characteristics of Surface Microstructures. *Journal of Fluids Engineering*, 140(5), 2018.

[35] Kathryn L. Kirsch and Karen A. Thole. Pressure loss and heat transfer performance for additively and conventionally manufactured pin fin arrays. *International Journal of Heat and Mass Transfer*, 108:2502 – 2513, 2017.

[36] S. C. Siw, M. K. Chyu, and M. A. Alvin. Heat transfer enhancement of internal cooling passage with triangular and semi-circular shaped pin-fin arrays. *Heat Transfer*, 4, 2012.

[37] M. Kapsis, L. He, Y. S. Li, O. Valero, R. Wells, S. Krishnababu, G. Gupta, J. Kapat, and M. Schaenzer. Multiscale Parallelized Computational Fluid Dynamics Modeling Toward Resolving Manufacturable Roughness. *Journal of Engineering for Gas Turbines and Power*, 142(2), 2020.

[38] A.D. Fitt, C.J.P. Forth, B.A. Robertson, and T.V. Jones. Temperature ratio effects in compressible turbulent boundary layers. *International Journal of Heat and Mass Transfer*, 29(1):159–164, 1986.

[39] T.L. Perelman. On conjugated problems of heat transfer. *International Journal of Heat and Mass Transfer*, 3(4):293 – 303, 1961.

[40] L. Nikuradse. Laws of flow in rough pipes, vdi forsch. 361. *English translation. NACA TM-1292*, 1933.

[41] H. Schlichting. Boundary-layer theory. *7th ednMcGraw-Hill InC*, 1979.

[42] F. Hummel, M. Lötzerich, P. Cardamone, and L. Fottner. Surface Roughness Effects on Turbine Blade Aerodynamics. *Journal of Turbomachinery*, 127(3):453–461, 2004.

[43] M. F. Tachie, D. J. Bergstrom, and R. Balachandar. Roughness Effects on the Mixing Properties in Open Channel Turbulent Boundary Layers. *Journal of Fluids Engineering*, 126(6):1025–1032, 2005.

[44] Samuel Altland, Haosen H. A. Xu, Xiang I. A. Yang, and Robert Kunz. Modeling of Cube Array Roughness: RANS, Large Eddy Simulation, and Direct Numerical Simulation. *Journal of Fluids Engineering*, 144(6):061106, 02 2022.

[45] D. Chatzikyriakou, J. Buongiorno, D. Caviezel, and D. Lakehal. Dns and les of turbulent flow in a closed channel featuring a pattern of hemispherical roughness elements. *International Journal of Heat and Fluid Flow*, 53:29 – 43, 2015.

[46] Donald P. Rizzetta and Miguel R. Visbal. Direct numerical simulations of flow past an array of distributed roughness elements. *AIAA Journal*, 45(8):1967–1976, 2007.

[47] P. Orlandi and S. Leonardi. Dns of turbulent channel flows with two- and three-dimensional roughness. *Journal of Turbulence*, 7:N73, 2006.

[48] M Bernardini, S Pirozzoli, P Orlandi, and SK Lele. Compressible boundary layer transition induced by isolated roughness elements. In *Proceedings of the Summer Program*, page 15, 2012.

[49] V. Citro, P. Luchini, F. Giannetti, and F. Auteri. Boundary-layer flows past an hemispherical roughness element: Dns, global stability and sensitivity analysis. *Procedia IUTAM*, 14:173–181, 2015. IUTAM$_A BCM Symposium on Laminar Turbulent Transition$.

[50] N. Abuaf, R. S. Bunker, and C. P. Lee. Effects of Surface Roughness on Heat Transfer and Aerodynamic Performance of Turbine Airfoils. *Journal of Turbomachinery*, 120(3):522–529, 1998.

[51] F. Montomoli, H. Hodson, and F. Haselbach. Effect of Roughness and Unsteadiness on the Performance of a New Low Pressure Turbine Blade at Low Reynolds Numbers. *Journal of Turbomachinery*, 132(3), 2010.

[52] J. H. Shin and S. Jin Song. Pressure Gradient Effects on Smooth and Rough Surface Turbulent Boundary Layers—Part I: Favorable Pressure Gradient. *Journal of Fluids Engineering*, 137(1), 2014.

[53] J. H. Shin and S. Jin Song. Pressure Gradient Effects on Smooth- and Rough-Surface Turbulent Boundary Layers—Part II: Adverse Pressure Gradient. *Journal of Fluids Engineering*, 137(1), 2014.

[54] N. Rostamy, D. J. Bergstrom, D. Sumner, and J. D. Bugg. An Experimental Study of a Turbulent Wall Jet on Smooth and Transitionally Rough Surfaces. *Journal of Fluids Engineering*, 133(11), 2011.

[55] H. Yan, W. Zhang, Z. Peng, and G. Meng. Effect of Three-Dimensional Surface Topography on Gas Flow in Rough Micronozzles. *Journal of Fluids Engineering*, 137(5), 2015.

[56] N. D. Cardwell, N. Sundaram, and K. A. Thole. Effect of Midpassage Gap, Endwall Misalignment, and Roughness on Endwall Film-Cooling. *Journal of Turbomachinery*, 128(1):62–70, 2005.

[57] E. L. Erickson, F. E. Ames, and J. P. Bons. Effects of a Realistically Rough Surface on Vane Heat Transfer Including the Influence of Turbulence Condition and Reynolds Number. *Journal of Turbomachinery*, 134(2), 2011.

[58] M. Lorenz, A. Schulz, and H.-J. Bauer. Experimental Study of Surface Roughness Effects on a Turbine Airfoil in a Linear Cascade— Part I: External Heat Transfer. *Journal of Turbomachinery*, 134(4), 2011.

[59] D. J. Whitehouse, J. F. Archard, and D. Tabor. The properties of random surfaces of significance in their contact. *Proceedings of the Royal Society of London. A. Mathematical and Physical Sciences*, 316(1524):97–121, 1970.

[60] T.R. Thomas. Characterization of surface roughness. *Precision Engineering*, 3(2):97–104, 1981.

[61] E.S. Gadelmawla, M.M. Koura, T.M.A. Maksoud, I.M. Elewa, and H.H. Soliman. Roughness parameters. *Journal of Materials Processing Technology*, 123(1):133–145, 2002.

[62] D. G. Bogard, D. L. Schmidt, and M. Tabbita. Characterization and Laboratory Simulation of Turbine Airfoil Surface Roughness and Associated Heat Transfer. *Journal of Turbomachinery*, 120(2):337–342, 1998.

[63] A. Sigal and J. E. Danberg. New correlation of roughness density effect on the turbulent boundary layer. *Journal of Turbomachinery*, 28(3):554–556, 1990.

[64] D.R. Waigh and R. J. Kind. Improved aerodynamic characterization of regular three-dimensional roughness. *AIAA Journal*, 36(6):1117–1119, 1998.

[65] J. P. Bons. A Review of Surface Roughness Effects in Gas Turbines. *Journal of Turbomachinery*, 132(2), 2010.

[66] S. K. Roberts and M. I. Yaras. Effects of Surface-Roughness Geometry on Separation-Bubble Transition. *Journal of Turbomachinery*, 128(2):349–356, 2005.

[67] M. N. Goodhand, K. Walton, L. Blunt, H. W. Lung, R. J. Miller, and R. Marsden. The Limitations of Using "Ra" to Describe Surface Roughness. *Journal of Turbomachinery*, 138(10), 2016.

[68] C. Gramespacher, M. Stripf, and H. Bauer. The Influence of Deterministic Surface Roughness and Freestream Turbulence on Transitional Boundary Layers: Heat Transfer Distributions and a New Transition Onset Correlation. *Journal of Turbomachinery*, 144(4), 2021.

[69] Li He. Chapter two - conjugate heat transfer: Some fundamentals and recent progress. 55:41–87, 2023.

[70] L. He. Spectral heat transfer coefficient for convection. *International Journal of Heat and Mass Transfer*, 216, 2023.

[71] J.M. Hacker and J.K. Eaton. Measurements of heat transfer in a separated and reattaching flow with spatially varying thermal boundary conditions. *International Journal of Heat and Fluid Flow*, 18(1):131–141, 1997.

[72] J. K. Eaton. The Discrete Green's Function for Convective Heat Transfer—Part 1: Definition and Physical Understanding. *Journal of Heat Transfer*, 142(10), 2020.

[73] J. K. Eaton and P. M. Milani. The Discrete Green's Function for Convective Heat Transfer—Part 2: Semi-Analytical Estimates of Boundary Layer Discrete Green's Function. *Journal of Heat Transfer*, 142(10), 2020.

[74] D. W. Hoffman and J. K. Eaton. Conjugate Heat Transfer Analysis Using the Discrete Green's Function. *Journal of Heat Transfer*, 143(3), 2021.

[75] E.R.G. Eckert and R. M. Drake. Analysis of heat and mass transfer. *Hemisphere Publishing New York*, 1987.

[76] W. M. Kays, M. Crawford, and B. Weigand. *Convective heat and mass transfer*, volume 4. 1980.

[77] Q. Zhang and L. He. Impact of Wall Temperature on Turbine Blade Tip Aerothermal Performance. *Journal of Engineering for Gas Turbines and Power*, 136(5), 2014.

[78] M. S. Shadloo and A. Hadjadj. Laminar-turbulent transition in supersonic boundary layers with surface heat transfer: A numerical study. *Numerical Heat Transfer, Part A: Applications*, 72(1):40–53, 2017.

[79] A. L. Braslow. A review of factors affecting boundary-layer transition. *NASA Technical Note D-3384*, 1966.

[80] D. A. Buntin, A. A. Maslov, and Yu. V. Gromyko. The effect of temperature of a cone nose-tip on the spectra of disturbances in the hypersound boundary layer. *Technical Physics Letters*, 100(241603), 2012.

[81] A. Fedorov, V. Soudakov, I. Egorov, A. Sidorenko, Y. Gromyko, D. Bountin, P. Polivanov, and A. Maslov. High-speed boundary-layer stability on a cone with localized wall heating or cooling. *AIAA Journal*, 53(9):2512–2524, 2015.

[82] Y. Zhu, W. Zhu, D. Gu, C. Lee, and C.R. Smith. Hypersonic transition over a heated wall. *Physics of Fluids*, 33(10), 2021.

[83] P. Schäfer, J. Severin, and H. Herwig. The effect of heat transfer on the stability of laminar boundary layers. *International Journal of Heat and Mass Transfer*, 38(10):1855–1863, 1995.

[84] S. Özgen. Effect of heat transfer on stability and transition characteristics of boundary-layers. *International Journal of Heat and Mass Transfer*, 47(22):4697–4712, 2004.

[85] H. W. Liepmann and G. H. Fila. Investigations of effects of surface temperature and single roughness elements on boundary-layer transition. *NACA Technical Note No. 1196*, 1947.

[86] E. Reshotko and A. Tumin. Role of transient growth in roughness-induced transition. *AIAA Journal*, 42(4):766–770, 2004.

[87] D. Arnal and O. Vermeersch. Compressibility effects on laminar-turbulent boundary layer transition. *International Journal of Engineering Systems Modelling and Simulation*, 3(1-2):26–35, 2011.

[88] R. Rubini, R. Maffulli, and T. Arts. Effect of the gas to wall temperature ratio on the bypass transition. *ASME Paper No. GT2018-76214*, 2018.

[89] L. H. Back, R. F. Cuffel, and P. F. Massier. Laminar, Transition, and Turbulent Boundary-Layer Heat-Transfer Measurements With Wall Cooling in Turbulent Airflow Through a Tube. *Journal of Heat Transfer*, 91(4):477–487, 1969.

[90] A. Dorfman and Z. Renner. Conjugate problems in convective heat transfer: Review. *Mathematical Problems in Engineering*, 2009.

[91] T. Verstraete and R.V.D. Braembussche. A novel method for the computation of conjugate heat transfer with coupled solvers. *Proceedings of International Symposium on Heat Transfer in Gas Turbine Systems*, 2009.

[92] L. He and M.L.G. Oldfield. Unsteady Conjugate Heat Transfer Modeling. *Journal of Turbomachinery*, 133(3), 2010.

[93] L. He and M. Fadl. Multi-scale time integration for transient conjugate heat transfer. *International Journal for Numerical Methods in Fluids*, 83(12):887–904, 2017.

[94] M. Shahi, J.B.W. Kok, J.C.R. Casado, and A. K. Pozarlik. Study of unsteady heat transfer as a key parameter to characterize limit cycle of high amplitude pressure oscillations. *Heat Transfer*, 5C, 2014.

[95] L. He. Closely coupled fluid-solid interface method with moving-average for les based conjugate heat transfer solution. *International Journal of Heat and Fluid Flow*, 79:108440, 2019.

[96] Tom Hickling and Li He. A multiscale framework for unsteady conjugate heat transfer with turbulence resolving methods — with application to rotating cavities. *International Journal of Heat and Fluid Flow*, 103:109174, 2023.

[97] T. Hughes, L. Mazzei, and K. E. Jansen. Large eddy simulation and the variational multiscale method. *Computing and Visualization in Science*, 3(1-2):47–59, 2000.

[98] J. E. Aarnes. On the use of a mixed multiscale finite element method for greaterflexibility and increased speed or improved accuracy in reservoir simulation. *Multiscale Modeling Simulation*, 2(3):421–439, 2004.

[99] P. Jenny, S.H. Lee, and H.A. Tchelepi. Multi-scale finite-volume method for elliptic problems in subsurface flow simulation. *Journal of Computational Physics*, 187(1):47–67, 2003.

[100] H. Hajibeygi, D. Karvounis, and P. Jenny. A hierarchical fracture model for the iterative multiscale finite volume method. *Journal of Computational Physics*, 230(24):8729–8743, 2011.

[101] T.Y. Hou, X. Hu, and F. Hussain. Multiscale modeling of incompressible turbulent flows. *Journal of Computational Physics*, 232(1):383–396, 2013.

[102] M. P. Errera and G. Turpin. Temporal multiscale strategies for conjugate heat transfer problems. *Journal of Coupled Systems and Multiscale Dynamics*, 1(1):89–98, 2013.

[103] L. He. Block-Spectral Approach to Film-Cooling Modeling. *Journal of Turbomachinery*, 134(2), 2011.

[104] L. He. Block-spectral mapping for multi-scale solution. *Journal of Computational Physics*, 250:13–26, 2013.

[105] L. He. Fourier spectral modelling for multi-scale aero-thermal analysis. *International Journal of Computational Fluid Dynamics*, 27(2):118–129, 2013.

[106] L. He. Multiscale block spectral solution for unsteady flows. *International Journal for Numerical Methods in Fluids*, 86(10):655–678, 2018.

[107] M. Kapsis, L. He, Y. S. Li, O. Valero, R. Wells, S. Krishnababu, G. Gupta, J. Kapat, and M. Schaenzer. Multiscale Parallelized Computational Fluid Dynamics Modeling Toward Resolving Manufacturable Roughness. *Journal of Engineering for Gas Turbines and Power*, 142(2), 2019.

[108] L. He. Two-scale conjugate heat transfer solution for micro-structured surface. *International Journal for Numerical Methods in Fluids*, 95(8):1260–1285, 2023.

[109] L. He. Averaging for High Fidelity Modeling - toward Large Eddy Simulations in Multi-Passage Multi-Row Configurations. *Journal of Turbomachinery*, 143(2), 2021.

[110] L. He. New two-grid acceleration method for unsteady navier-s tokes calculations. *Journal of Propulsion and Power*, 9(2):272–280, 1993.

[111] L He. Three-dimensional unsteady navier—stokes analysis of stator—rotor interaction in axial-flow turbines. *Proceedings of the Institution of mechanical Engineers, Part A: Journal of Power and Energy*, 214(1):13–22, 2000.

[112] L He. Harmonic solution of unsteady flow around blades with separation. *AIAA journal*, 46(6):1299–1307, 2008.

[113] P. Spalart and S. Allmaras. A one-equation turbulence model for aerodynamic flows. *30th aerospace sciences meeting and exhibit*, 1992.

[114] F. Menter. Review of the shear-stress transport turbulence model experience from an industrial perspective. *International Journal of Computational Fluid Dynamics*, 23(4):305–316, 2009.

[115] J. Smagorinsky. General circulation experiments with the primitive equations: I. the basic experiment. *Monthly Weather Review*, 91(3):99 – 164, 1963.

[116] A. Jameson. Time dependent calculations using multigrid, with applications to unsteady flows past airfoils and wings. *10th Computational Fluid Dynamics Conference*, 1991.